The application of particle image velocimetry for the analysis of high-speed craft hydrodynamics

Jacobi, G.

DOI
10.4233/uuid:12a7e93e-34f1-41b5-864f-156ac0f60d30

Publication date
2020

Document Version
Final published version

Citation (APA)
Jacobi, G. (2020). *The application of particle image velocimetry for the analysis of high-speed craft hydrodynamics*. [Dissertation (TU Delft), Delft University of Technology]. https://doi.org/10.4233/uuid:12a7e93e-34f1-41b5-864f-156ac0f60d30

Important note
To cite this publication, please use the final published version (if applicable).
Please check the document version above.

The Application Of Particle Image Velocimetry For The Analysis Of High-Speed Craft Hydrodynamics

THE APPLICATION OF PARTICLE IMAGE VELOCIMETRY FOR THE ANALYSIS OF HIGH-SPEED CRAFT HYDRODYNAMICS

Proefschrift

ter verkrijging van de graad van doctor
aan de Technische Universiteit Delft,
op gezag van de Rector Magnificus prof. dr. ir. T.H.J.J. van der Hagen,
voorzitter van het College voor Promoties,
in het openbaar te verdedigen op 24 augustus 2020 om 12:30 uur

door

Gunnar JACOBI

Diplom Ingenieur Schiffbau und Meerestechnik,
Universität Rostock, Duitsland,
geboren te Göttingen, Duitsland.

Dit proefschrift is goedgekeurd door de

promotor: Prof. dr. ir. R.H.M. Huijsmans
copromotor: Dr. ir. I. Akkerman

Samenstelling promotiecommissie:

Rector Magnificus,	voorzitter
Prof. dr. ir. R.H.M. Huijsmans	Technische Universiteit Delft
Dr. ir. I. Akkerman	Technische Universiteit Delft
Onafhankelijke leden:	
Dr. L. De Santana	Universiteit Twente
Dr. D. Ragni	Technische Universiteit Delft
Dr.-Ing. F. di Felice	CNR-INM
Prof. dr. ir. J. Westerweel	Technische Universiteit Delft
Prof. dr. A.E.P. Veldman	Rijksuniversiteit Groningen
Prof. ir. J.J. Hopman	Technische Universiteit Delft , reservelid

This research has been conducted within the Fast FEM project under the guidance of the Dutch Research Council (NWO). The project has been made possible with contributions from following partners:

Delft University of Technology
DAMEN Shipyards
Maritime Research Institute Netherlands
The Royal Netherlands Navy
Bureau Veritas
Lloyds Register
The Royal Netherlands Rescue Organization KNRM
University of Twente

Keywords: particle image velocimetry (PIV), underwater PIV, underwater PIV uncertainty, pressure from PIV, fast ships, interceptor

Printed by: Gildeprint - The Netherlands

Front & Back: Judith Jacobi

ISBN 978-94-6402-176-9

An electronic version of this dissertation is available at
repository.tudelft.nl.

CONTENTS

Summary **ix**

1 Introduction **1**
- 1.1 Hydrodynamics of high-speed craft . . . 2
- 1.2 Prediction and analysis of high-speed craft hydrodynamics . . . 4
- 1.3 Determination of hydrodynamic pressure distributions from measured velocity fields . . . 8
- 1.4 Research objectives . . . 10
- 1.5 Chapter outline . . . 11

2 PIV in towing tank applications **13**
- 2.1 PIV principle . . . 13
  - 2.1.1 Stereo-PIV . . . 15
- 2.2 PIV in towing tank applications . . . 19
  - 2.2.1 Overview . . . 19
  - 2.2.2 The TU Delft underwater PIV-system . . . 20
- 2.3 Critical operational aspects . . . 22
- 2.4 High-speed related error sources . . . 25
  - 2.4.1 Structural vibrations . . . 26
  - 2.4.2 Large out-of-plane velocities . . . 27

3 Pressure reconstruction from velocity fields **29**
- 3.1 General approach . . . 30
- 3.2 Time and phase-averaged pressure fields . . . 31

4 The application of PIV for the analysis of interceptor hydrodynamics **35**
- 4.1 Test case: Hydrodynamics of interceptors . . . 36
- 4.2 Experimental setup . . . 37
  - 4.2.1 PIV setup . . . 39
- 4.3 PIV processing . . . 41
  - 4.3.1 Vibration analysis and correction . . . 41
  - 4.3.2 Vector field calculation . . . 46

4.4 Pressure reconstruction and force determination . . . 47
4.5 Measurement uncertainty assessment and propagation . . . 49
4.5.1 Measurement uncertainty . . . 49
4.5.2 Uncertainty propagation . . . 51
4.6 Numerical simulations . . . 54
4.7 Discussion and comparison of experimental and numerical results. . . . 57
4.7.1 2d results. . . . 57
4.7.2 3d results. . . . 61
4.8 Discussion . . . 67

5 Velocity and pressure measurements in the bow region of a fast ship 69
5.1 Test case . . . 70
5.1.1 Calm water. . . . 72
5.1.2 Forced heave oscillations . . . 72
5.2 Numerical simulations . . . 74
5.2.1 Calm water simulations . . . 75
5.2.2 Forced oscillation simulations . . . 77
5.3 Experimental setup . . . 81
5.3.1 PIV setup. . . . 81
5.4 Feature detection and masking of PIV images . . . 84
5.4.1 Ship hull identification. . . . 85
5.4.2 Free-surface identification . . . 88
5.5 Vector field calculation and data reduction . . . 91
5.5.1 Multi-plane measurements . . . 91
5.5.2 Oscillation tests . . . 94
5.6 Pressure reconstruction . . . 97
5.7 Measurement uncertainty assessment and propagation . . . 100
5.7.1 Uncertainty propagation. . . . 102
5.8 Discussion and comparison of experimental and numerical results. . . . 103
5.8.1 Multi-plane PIV measurements . . . 103
5.8.2 Oscillation tests . . . 109
5.9 Discussion . . . 117

6 Conclusion 119
6.1 PIV at high carriage speeds . . . 119
6.1.1 Structural vibrations . . . 119
6.1.2 Out-of-plane flow . . . 120
6.2 Pressure measurement with PIV in towing tanks . . . 121
6.2.1 Pressure PIV for high-speed craft hydrodynamics . . . 121
6.3 Outlook and future recommendations . . . 122

References **125**

Acknowledgements **133**

Curriculum Vitæ **135**

List of Publications **137**

SUMMARY

As soon a ship operates at high forward speeds its weight is pre-dominantly supported by hydrodynamic, rather than hydrostatic forces. Small changes in the dynamic pressure distribution on the ship hull can have a significant influence on the ship's running attitude in calm water, but also on its seakeeping performance. In order to further improve these vessels it is important to experimentally and numerically investigate the flow in the vicinity of the ship hull and to accurately determine global as well as local pressure distributions.

In contrast to traditional experimental techniques, which often lack spatial resolution, this thesis presents an alternative experimental method for the analysis of the flow field and the reconstruction of hydrodynamic pressures from particle image velocimetry (PIV). This is a non-intrusive, laser-optical measurement technique where the velocity field of an entire region within the flow is measured simultaneously. The thesis discusses to what extend the PIV technique can be used to analyse the hydrodynamics of high-speed ships during model tests in towing tanks. The research particularly focusses on the influence of high towing tank carriage velocities, that can result in structural vibrations and high out-of-plane velocities, on the quality of the measured velocity fields. Furthermore it is focussed on the reconstruction of hydrodynamic pressures from these, and the propagation of measurement uncertainties towards the final hydrodynamic pressure fields. Hereby, the spatial variation of uncertainties within the measurement region is taken into account.

The analysis is done by means of two practical applications with a towed underwater stereo-PIV system. A first test-case analyses the flow in the transom region of a generic planning hull and the influence of an interceptor on the local pressure distribution. A second test-case focusses on the analysis of the flow field in the bow region of a semi displacement hull. Results from both cases show, that measurements can be obtained in regions, where high-spatial resolution is necessary, but cannot be provided by traditional techniques. Being interested in time- or phase-averaged results, multi-plane PIV measurements are used to extend the observed region to capture the three-dimensional velocity and pressure fields. The obtained experimental results are in good agreement with results from numerical simulations.

1

INTRODUCTION

The marine industry is continuously striving to develop faster ships. In the area of passenger and cargo transport, the motivation for this is of economic nature, to compete with other means of transportation. However, for some applications, high speed at sea is even indispensable, e.g., as search and rescue (SAR) vessels (Figure 1.1) or patrol boats and combat crafts, where the success of the mission is highly dependent on the quick response time. To guarantee reliable operation, these vessels do not only have to go fast in calm water conditions, but also have to operate in severe conditions, while maintaining the highest possible speed. Next to the broad range of requirements with respect to their operational profile, the complexity of the hydrodynamics and their effect on calm water as well on the seakeeping behavior of these vessels makes the design of a high-speed craft a demanding task. To outline the complexity and the necessity of a good understanding of the hydrodynamics of high-speed ships, the reader will be given a short introduction to these.

Figure 1.1: Photograph of a KNRM rescue vessel operating in waves

1

1.1. HYDRODYNAMICS OF HIGH-SPEED CRAFT

While numerous definitions of high-speed crafts exist, in this work, a high-speed craft is considered as a hull borne vessel traveling at speeds exceeding a Froude number of $Fr_L = U/\sqrt{Lg} = 0.4$. The Froude number describes the ratio of inertial forces to the external gravitational forces, with U being the speed of the ship, L being the waterline length, and g the gravitational acceleration. Ships with their operational speeds below this number are mainly supported by hydrostatic forces, which according to the principle of Archimedes, are proportional to the displaced water of the submerged hull. With the hydrodynamic pressure being proportional to the square of the ship speed, their contribution to the forces supporting the ship in this speed range is comparable small, resulting only in minor changes of trim and sinkage of these displacement vessels. However, as soon as a ship operates at higher forward speeds, hydrodynamic pressures start playing a significant role, which may considerably change the trim and sinkage of the vessel. A conventional displacement hull with its convex buttock lines in the aft section will start to significantly squat, and trim and resistance will increase dramatically. High-speed vessels, however, have hull forms adopted to the hydrodynamic phenomena associated with higher Froude numbers. They have straight buttock lines that end at a transom stern, and the flow starts to separate at $Fr_L > 0.4$, leaving the transom clear. The generated hydrodynamic lift will support a substantial part of the ship's weight. Depending on their maximum operating speed, the class of high-speed mono-hulls can be subdivided into semi-displacement vessels and fully planning vessels. At $Fr_L > 1.0 - 1.2$, most of the weight of the hull will be carried by the generated hydrodynamic pressure. The vessel is considered to be fully planing. In the intermediate speed range of $0.4 < Fr_L < 1 - 1.2$, the major part of the vessel is still supported by hydrostatic forces. The performance of the vessels, however, is always highly affected by the hydrodynamic pressure distribution on the hull. For this reason, they are considered as semi-displacement vessels. For high-speed crafts, where the waterline can vary significantly between different speeds, the reference length L for the calculation of the Froude number is often defined as the cubic root of the ships displacement $\nabla^{1/3}$, resulting in the displacement Froude number $Fr_\nabla = U/\sqrt{\nabla^{1/3} g}$.

A typical high-speed monohull and the dependency of its trim and sinkage on forward speed are depicted in Figure 1.2. It is clearly shown that due to the increased hydrodynamic lift, the trim as well as sinkage change considerably with respect to the ship's floating position at zero speed. With the ship being lifted out of the water at higher speeds, this is beneficial for the total resistance of the vessel. Due to the reduced wetted surface and submerged volume, the increase of frictional as well as wave-making resistance at higher speeds will be reduced. A systematic study of Clement and Blount (1963) shows that variations in trim and sinkage are not only a pure function of forward speed but are also strongly affected by changing the pressure distribution on the hull with varying its

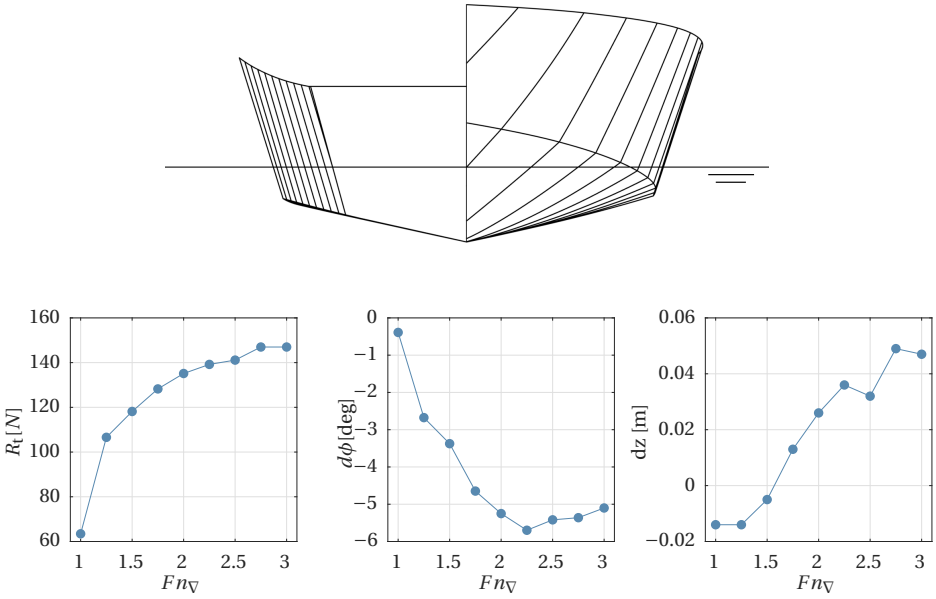

Figure 1.2: Linesplan of the parent hull form of the systematic series of planing hull forms by Clement and Blount (1963) and the speed dependency of resistance, trim and sinkage

geometrical parameters. For a long time, the generation of a large hydrodynamic lift was the main goal in the design process of a fast ship to maximize its speed.

Being optimized for the highest possible speeds in calm water conditions, the seakeeping behavior of these first-generation high-speed vessels was often less than satisfactory. As soon as these ships had to operate in more severe conditions with large waves, they experienced large relative heave and pitch motions. Wave impacts were associated with large accelerations, which significantly impaired the comfort and safety of crew and passengers. As a result, fast ship applications were, to a large extent restricted to sheltered areas. Driven by the increasing demand for high-speed crafts in offshore applications at the end of the 1960s, researchers started to further investigate the hydrodynamic phenomena involved with the operation of high-speed ships in waves.

Savitsky (1968) was the first to give a detailed description of factors that influence the behavior of fast ships in waves. Fridsma (1969), Fridsma (1971), Van den Bosch (1970) and later Keuning and Gerritsma (1982) focused on the experimental quantification of these, by performing systematic model tests in regular and irregular waves. Amongst other things, the influence of changes in trim and sinkage and the influence of the deadrise angle on motion response and accelerations were quantified. Both concluded that at high forward speeds, the relation of the ship's motion and the wave elevation is strongly

non-linear. The increase of non-linearity of the motion response with increasing forward speed and with decreasing deadrise angles led to the conclusion that the non-linearity of motions is highly dependent on the amount of hydrodynamic lift generated on the hull. These findings were in conflict with the previous design philosophy for fast ships where a maximum hydrodynamic lift was aimed at for reduced resistance and maximum forward speed. As a consequence, the focus in the design process changed to finding the optimal balance between maximum speed and seaworthiness. With the length of fast ships being relatively small compared to the length of the encountered waves, they experience relatively large motions when sailing in waves. Keuning (1994) noted that the characteristic V-shape of the hull leads to significant variations in the submerged geometry. Next to the non-linear hydrodynamic lift, he identified non-linear wave exciting forces, especially in the bow region, to have a significant influence on the seakeeping behavior.

While this better understanding led to the development of new ship designs with improved seakeeping behavior such as the enlarged-ship and axe-bow design (Keuning and Pinkster (1995, 2002)), also additional motion control devices are used to optimize the calm water, as well as the seakeeping performance of a fast ship. T-foils and interceptors make use of the high forward speeds where they create a hydrodynamic lift force, which is proportional to the squared velocity. At higher speeds, these devices can generate an additional trim moment to control the running attitude of the ship. Used in static configurations, they are mainly used for resistance reduction by influencing the trim and sinkage of the ship. However, by dynamically changing the foil angle or trim tab intrusion height, these devices can also be used for active ride-control of fast ships in waves.

The herein presented description of the hydrodynamic characteristics is by far not complete and the reader is referred to Faltinsen (2005), Keuning (1994) and De Jong (2011) for a more elaborate description of the previously described phenomena. In summary, it has been shown that the behavior of high-speed ships depends on numerous non-linear hydrodynamic effects, which all need to be considered in the early design stage of a ship.

1.2. PREDICTION AND ANALYSIS OF HIGH-SPEED CRAFT HYDRODYNAMICS

While initially researchers had to rely solely on experimental towing tank tests and derived semi-empirical formulas, to investigate the hydrodynamics of high-speed crafts in calm water and waves (Clement and Blount (1963), Fridsma (1969)), in the 1970s numerical methods started to become more and more of importance.

Initial seakeeping methods considered the ship, which was moving in waves, as a linear system. Here the response of the ship was in linear relation to the incoming wave. By definition, only applicable for low-speed ships, Blok and Beukelman (1984)

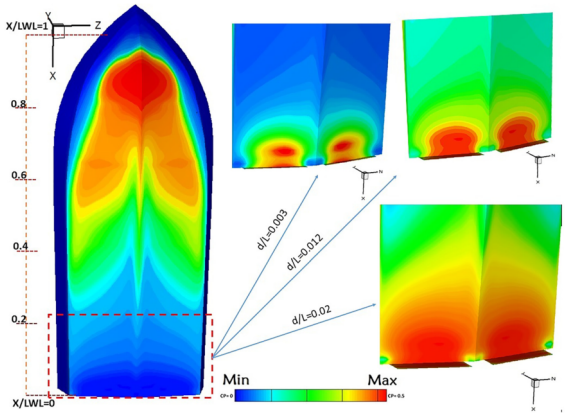

Figure 1.3: Pressure distribution of the hull of a planing ship for different appendage configurations determined from CFD simulations (from Mansoori and Fernandes (2016))

evaluated the applicability of a linear strip theory for the motion prediction of a fast semi-displacement ship. Predicted motions were in good agreement with measurements. However, Keuning (1994), who extended the strip theory of Zarnick (1978) by including the influence of non-linear effects, later found large differences between predicted and experimentally determined added mass and damping distributions. He emphasized the importance of considering non-linearities in the numerical seakeeping codes. Van Walree (1999) later presented a non-linear time domain panel method, which was based on a three-dimensional time-domain Green function. De Jong et al. (2007) later extended the method. Comparisons with motions, obtained from experiments in regular and irregular waves, showed the improved prediction of the calm water running trim and sinkage, as well as the behavior of fast ships in waves. He concluded that the method obtained a more fundamental three-dimensional pressure distribution taking into account forward speed effects and the three-dimensionality of the flow.

With the steady improvement of computers, fully viscous approaches were becoming more and more attractive. The numerical solution of the Reynolds-averaged Navier-Stokes (RANS) equations gives the most accurate description of the flow around high-speed crafts and thus allows for even more detailed insights into the hydrodynamics of these. Figure 1.3 shows results from CFD simulations with a planing ship, which were conducted to study the effect of different appendage configurations on the pressure distribution in the transom region of the vessel. Because of the computational costs, RANS simulations for fast ships are mostly restricted to the prediction of resistance and running trim and sinkage in calm water. Publications about RANS simulations of ships advancing in waves are rare and mostly restricted to displacement vessels (Larsson et al. (2013)). Results from the Gothenburg CFD workshop 2010 (Larsson et al. (2013)), also showed that for normal

displacement vessels, the average error in computed resistance has been reduced to 2.1 %, making RANS simulations a reliable design tool for these types of ships. However, Haase et al. (2012) reported that for high-speed ships, average deviations to towing tank tests are still in the order of 10 %.

From the presented overview of existing numerical methods for the assessment of high-speed hydrodynamics, it is seen that the steady improvement of numerical tools delivers more and more detailed insights into the hydrodynamics of ships. To support this development, towing tank tests are necessary to provide experimental data for validation purposes. They can be also seen as an alternative means to numerical techniques, where these are not yet reliable enough or computationally too expensive. However, to validate the more and more complex numerical codes, experimental methods also have to provide the same level of detailedness.

Concerning the validation of seakeeping codes, Keuning (1994) and De Jong (2011) concluded that it is not anymore sufficient to measure the result of the pressure distribution on the hull, i.e., motions and integral forces, but also the local pressure distribution itself. To get a more detailed representation of the local effect of the hydrodynamic pressure distribution, Keuning (1994) and also later De Jong and Keuning (2006) used a segmented model to obtain section-wise forces to derive the longitudinal added mass and damping coefficient distributions. During both tests, the ship was divided into seven segments, which were connected to a rigid backbone via several force balances. Figure 1.4 (top) shows a schematic drawing of the model segments and the backbone. Figure 1.4 (bottom) shows the measured discrete longitudinal added mass and damping distribution obtained from forced oscillation tests.

However, segmented model tests are rarely seen. The reason for this is extensive model preparation and uncertainties due to the interaction of segments. De Jong (2011) proposed the additional usage of pressure transducers to measure the local pressure distributions, but at the same time, he mentioned the problems of applying pressure transducers to measurements at high forward speeds. The fact that the dynamic pressure variations due to the rigid body motions were comparatively small compared to large static pressures made a reliable determination of these problematic. Additionally, a perfectly flush installation into the faired hull is needed to avoid a disturbance of the local flow. Van Walree et al. (2016) and Choi (2018) presented results from seakeeping tests with a fast-displacement vessel, where the pressure distribution in the bow region has been obtained from a total of 63 pressure transducers. An example of the time-averaged pressure field, including the positions of the pressure transducers, is depicted in Figure 1.5. It is shown that these measurements can give an improved spatial and temporal description of the pressure field on the ship hull. However, no information is obtained about the flow around the ship hull, which is the source of the hydrodynamic pressure distribution.

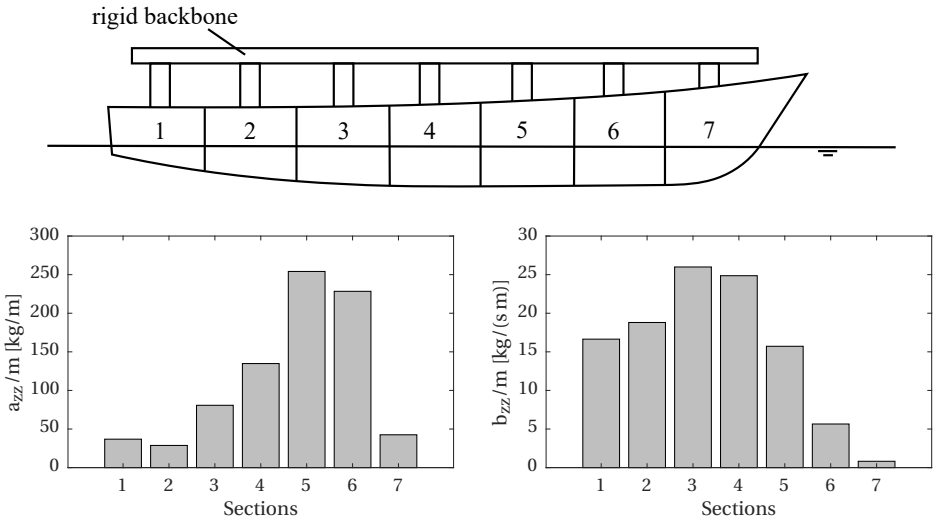

Figure 1.4: Schematic drawing of segmented ship model mounted to a rigid backbone via force balances (top); longitudinal added mass and damping distribution obtained from forced oscillation tests with a segmented model by Keuning (1994)

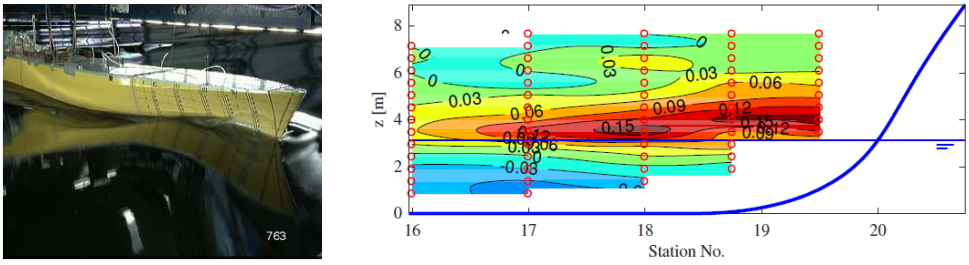

Figure 1.5: Photograph of the fast displacement ship, tested by Van Walree et al. (2016) for pressure measurements in the bow region (left). Location of the pressure sensors and the corresponding time-averaged pressure field on the ship hull (from Choi (2018)) (right)

1

1.3. DETERMINATION OF HYDRODYNAMIC PRESSURE DISTRIBUTIONS FROM MEASURED VELOCITY FIELDS

A technique that has been increasingly applied in recent years to measure the flow field is the particle image velocimetry (PIV) technique (Adrian and Westerweel (2011)). Being a laser optical measurement technique, PIV measurements can be conducted in a fully non-intrusive manner. While the fluid to be investigated is seeded with particles that follow the flow, a laser-sheet illuminates the particles in the measurement plane. Their velocity can be determined from cross-correlation of successive pictures taken with a short time separation. While a single camera arrangement allows for a measurement of in-plane velocities, the extension of the system to a stereo camera setup allows for a measurement of all three velocity components. Recent developments have seen tomographic setups with more than three cameras, which in combination with a volumetric illumination of the measurement area, allows for a volumetric flow field measurement (Elsinga et al. (2006))

To study the flow around ships, the technique has first been applied by Dong et al. (1997) in a towing tank environment for the investigation of the bow wave structure of a ship. Further applications include, amongst others, wake flow measurements (Gui et al. (2001), Falchi et al. (2014)), but also measurements with ship models in waves (Huijsmans et al. (2005), Longo et al. (2001, 2007)). The technique has become a reliable means to determine the velocity field around the ship hull during towing tank tests. In towing tank applications, PIV systems are nowadays mostly realized as submerged camera systems with a watertight housing, which is attached to the towing tank carriage and moves together with the ship model. A typical underwater setup, which has been used for flow field measurements in the bow region, is depicted in Figure 1.6. While numerous towing tank applications have been reported for low-speed applications up to $Fn = 0.45$ (Dong et al. (1997), no measurements have been conducted at high speeds yet.

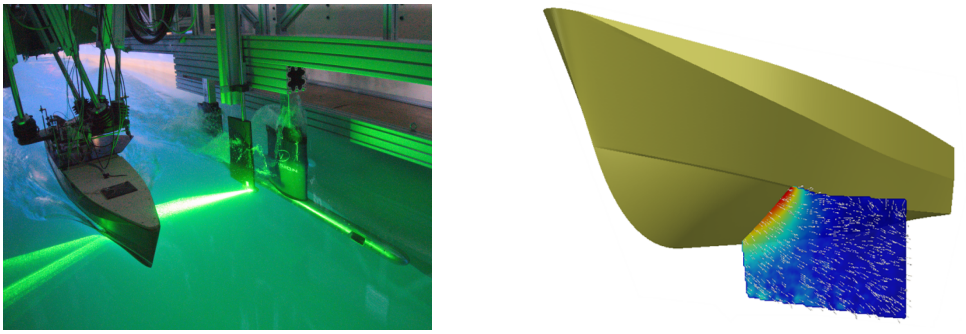

Figure 1.6: Typical underwater PIV setup for the measurement of the flow field around the ship (left). Time-averaged velocity field close to the ship hull, obtained with PIV measurements (right)

While the application of PIV in towing tanks is up to now restricted to the study of the flow kinematics, it has been successfully applied in other research areas such as aerodynamics to derive the pressure distribution in the flow. While the Navier-Stokes equations describe the relationship between the flow field and the pressure field, the measured velocities and gradients can be utilized to reconstruct the pressure field. The recent development of the PIV technique and hardware components nowadays allows for a reconstruction of the 3D volumetric and even time-resolved pressure fields, using tomographic or stereoscopic scanning PIV. A detailed review of the main principles of PIV-based pressure measurement and a discussion of the methods' accuracy has been presented by Van Oudheusden (2013). Pressure reconstruction from PIV measurements is well studied and widely accepted in numerous aerodynamic and a few hydrodynamic applications. A good example of a practical application is given by Ragni et al. (2012), who used multi-plane stereo PIV measurements to assess the loads of an aircraft propeller (Figure 1.7). In the field of ship hydrodynamics, the technique has been successfully applied by Nila et al. (2013) to estimate slamming loads during the water entry of rigid bodies (Figure 1.8).

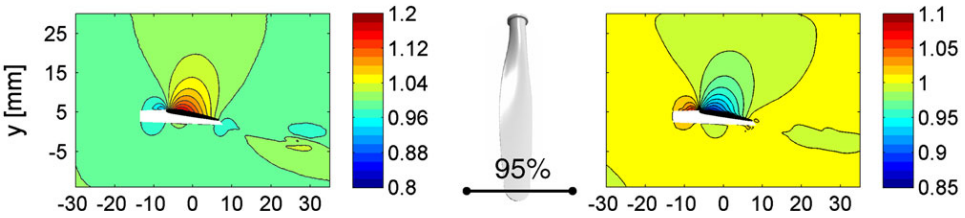

Figure 1.7: Pressure reconstruction from stero PIV measurements for an aircraft propeller: Velocity field Magnitude (left) and reconstructed pressure field (right) (from Ragni et al. (2012))

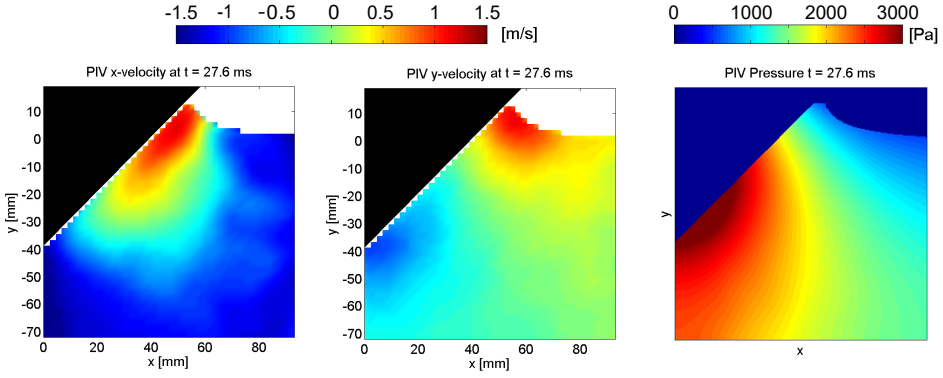

Figure 1.8: Pressure reconstruction from planar PIV measurements for a dropping wedge: Velocity field components and reconstructed pressure field (from Nila et al. (2013))

1

1.4. RESEARCH OBJECTIVES

To further improve the development of fast ships, measurement methods have to give more insights into hydrodynamic pressure distributions on ship hulls. It has been pointed out that actual pressure and load measurement techniques used in towing tank experiments lack spatial resolution. While the PIV technique allows the assessment of the flow field kinematics with as well high spatial as temporal resolution, the reconstruction of the flow dynamics from these measurements poses an interesting alternative to existing methods. Motivated by successful application of this technique in other research areas, the main question to be answered in this dissertation is:

To what extent can the particle image velocimetry technique be used to investigate the hydrodynamics of high-speed ships during model tests in towing tanks?

To identify possible limitations of the measurement method for its application at high towing speeds, the principles of the PIV technique and the pressure reconstruction from flow measurements have to be reviewed. Based on the review, the requirements for operating a PIV system in a towing tank have to be specified.

It is known from towing tank measurements, that with increasing carriage speed, also structural vibrations will increase. As seen from industrial wind tunnel applications by Novara et al. (2015), the quality of PIV measurements is very sensitive to these vibrations. While no measurements have been reported in towing tanks with speeds exceeding $Fn > 0.45$, it has to be determined how the PIV system behaves at high speeds and if structural vibrations of the carriage can affect measurement quality. In case this poses a limitation, solutions have to be found, which enable accurate PIV measurements at high carriage speeds.

While in planar- and stereo-PIV applications, the laser-sheet has only a limited thickness, the length of the time interval between a set of double frames is also very limited to capture particles moving perpendicular to the light-sheet. If the time interval between two frames is too long, particles will leave the light-sheet and cannot be found back in the second recorded frame. It has to be discussed how the resulting short inter-frame time affects the measurements. As ships usually have complex three-dimensional shapes and move due to incoming waves, it has to be investigated how to deal with changing geometry shapes and moving objects in the recorded pictures. A masking procedure needs to be developed for automated processing of PIV images.

Since the quality of the reconstructed pressure fields highly depends on the quality of the measured velocity field, sources of uncertainty have to be defined, and detailed uncertainty analysis is necessary, which includes the propagation of uncertainties towards the pressure fields. Finally, it has to be evaluated, how the proposed method performs compared to numerical simulations.

1.5. CHAPTER OUTLINE

To understand the possible limitations of the PIV method at high speeds in towing tank applications, which have already been anticipated in Section 1.4, Chapter 2 will provide a more detailed explanation of the principles of PIV. A more detailed explanation of possible sources of uncertainties will be also provided.

Chapter 3 will give an overview of the different approaches for pressure reconstruction from PIV. A detailed description of the method used in this thesis is given.

Chapter 4 and 5 will deal both with the analysis of the different factors influencing the pressure reconstruction from PIV quality at high carriage speeds by means of PIV measurements conducted in the TU Delft towing tank.

Chapter 4, in particular, will present results from PIV measurements in the transom region of a fast ship, which is equipped with an interceptor to picture the flow and pressure distribution in the transom region of the ship and investigate the influence of vibrations at high carriage speeds on the measurement quality. Based on the vibration assessment method, a method is presented to correct for vibrations in PIV measurements as a pre-processing operation previous to the vector calculation. Before comparing the findings to the results of numerical simulations, a detailed uncertainty analysis is presented, which takes into account the spatial uncertainty of the velocity field.

By presenting measurement results from PIV measurements in the bow region of an enlarged ship concept in Chapter 5, a test case is presented, where the out-of-plane motion of the flow is considerably higher than the in-plane velocities. Furthermore, the chapter deals with the handling of complex 3D shapes and moving objects in PIV images. With performing stereoscopic multi-plane PIV measurements in a total of 68 planes over a length of 0.68 meters, the averaged volumetric velocity and pressure fields are reconstructed in this region. Additionally, phase-averaged measurements with a vertically oscillating ship are presented. An automatic masking procedure is presented as a pre-processing tool previous to the vector calculation procedure. Results are compared to numerical simulations.

Chapter 6 will give a conclusion and discuss to what extent the particle image velocimetry technique can be used to investigate the hydrodynamics of high-speed ships during model tests in towing tanks to contribute to the improvement of safety and operability of these vessels. The dissertation is concluded with giving recommendations for PIV measurements in towing tanks and the reconstruction of pressures from these.

2

PIV IN TOWING TANK APPLICATIONS

To develop a deeper understanding of the hydrodynamics of high-speed crafts, it is proposed to apply the pressure PIV technique during towing tank tests, where the hydrodynamic pressure field is computed from measured velocity fields. The following chapter will give a brief introduction to the basic principles of the PIV technique, focusing on the application of the technique in towing tank environments. Special attention will be paid to the particularities of the measurement setup, as well as critical issues and error sources during operation of the measurement system.

2.1. PIV PRINCIPLE

Particle image velocimetry is a non-intrusive laser-optical measurement technique to determine the instantaneous velocity vector field in a moving fluid. In contrast to other quantitative flow measurement techniques, such as Pitot tubes or laser Doppler velocimeters, which give a discrete, point-wise measurement at a single location, particle image velocimetry enables an instantaneous, quantitative description at a large number of locations within the flow field. A schematic description of the measurement technique, including the main system components and essential steps in the evaluation procedure, is depicted in Figure 2.1. While the fluid to be investigated is seeded with particles that can accurately follow the flow, a laser-sheet illuminates the particles in the measurement area at two successive time instants. For further processing, the recorded images are split into small sub-regions. Within these interrogation windows, the displacement of the particles can be determined from cross-correlation of successive pictures taken with a short time

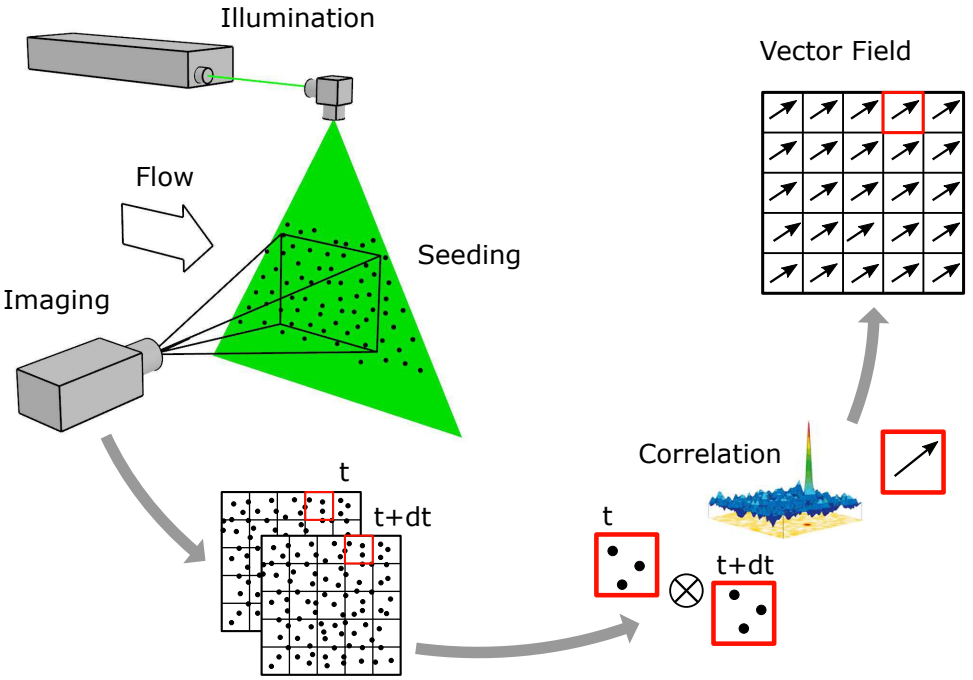

Figure 2.1: Schematic description of the basic PIV principle

separation. Having calibrated the imaging system to generate a mapping function from the object-plane onto the image plane, the velocity field and other properties of the flow can be derived from this.

From the previous description, it is seen that the measurement consists of an experimental part and a processing part. The main components of the experimental part are the **seeding** of the flow with appropriate tracer particles, the **illumination** of the measurement plane, and the **imaging**. The displacement and velocity vector calculation is done as a **processing** of the recorded images. A detailed description of the measurement principle would exceed the scope of this work and can be found in Adrian and Westerweel (2011) and Raffel et al. (2018). A more in-depth discussion of the system components concerning towing tank specific applications will be given in 2.2. For simplicity, Figure 2.1 shows only a single camera setup. This only allows for a measurement of the two velocity components within the plane, which is spanned by the light-sheet. Any out-of-plane motion of the flow results in an erroneous measurement of these, which makes the technique only accurate for two-dimensional flows (Adrian and Westerweel (2011)). While most flows to be studied in experimental facilities are highly three-dimensional, the out-of-plane component has to be taken into account to guarantee an error-free measurement. Following the stereo-vision principle, this can be achieved by looking at the measurement plane

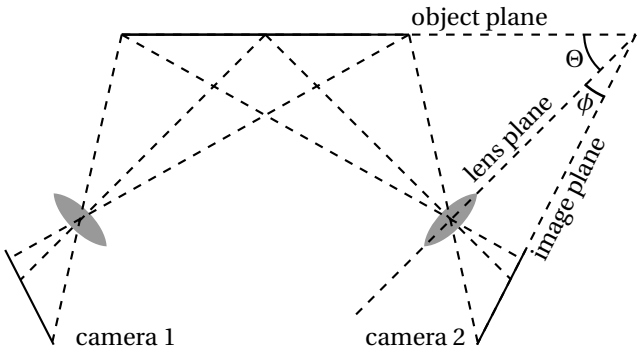

Figure 2.2: Schematic description of a symmetrical stereo-PIV setup

with two cameras from different viewing angles. With this stereoscopic-PIV technique, a measurement of all three velocity components within the light-sheet can be realized. The measurement principle of stereo-PIV will be further explained in the following.

2.1.1. STEREO-PIV

To further outline the stereo-PIV measurement principle, Figure 2.2 shows a schematic drawing of a typical stereo arrangement with two cameras, looking at the same illuminated object plane, with an angular displacement Θ. For simplicity, a symmetric configuration is shown, with both cameras being on one side of the light-sheet. Depending on the setup, also non-symmetric arrangements are possible, and cameras can also be on opposite sides of the light-sheet. While usually, the lens and image plane are parallel to the plane of focus, the rotation of the cameras with respect to the object plane would result in a de-focused image which is only focused at the intersection line of the focal plane with the object plane. While choosing a smaller aperture could compensate for this effect, resulting in a larger field of depth, this is not applicable for PIV applications, where usually large apertures are essential for a high-quality measurement signal. Another possibility is the relocation of the focal plane due to a rotation of the image plane in the camera with respect to the lens plane. As depicted in Figure 2.2, the image plane has to be tilted in such a way that it coincides with the intersection line of object plane and lens plane. This is called the Scheimpflug condition. Another problem related to the angular viewing directions of the cameras is the non-uniform image magnification, which results in a distorted image. This requires a sophisticated calibration of the imaging system to create an accurate mapping function between object and image space. As the quality of the final reconstructed velocity field is highly dependent on the calibration accuracy, it will be discussed more thoroughly in the following section. For the final calculation of the velocity vector field from the particle displacement in the images, different approaches exist. However, all

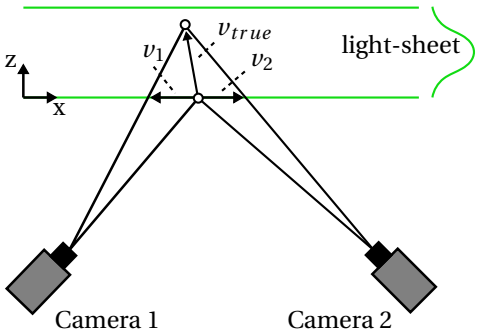

Figure 2.3: Stereo-PIV principle: Reconstruction of the three-component velocity vector from two planar vectors

of these differ only in the order of displacement calculation and back projection to the world coordinate system (Wieneke (2005)). The basic principle, which is common to all methods, can be seen in Figure 2.3, showing that all three velocity components within the measurement plane can be reconstructed from the planar, two-component vector field that is computed for each camera. A clear example of a typical vector calculation procedure under consideration of the mapping function can be also found in Wieneke (2005). Lawson and Wu (1997) show that the accuracy of the single velocity components is highly dependent on the viewing angle between the cameras. While at $2\Theta = 90°$ the random out-of-plane component error $\sigma_{\Delta z}$ and the in-plane component error $\sigma_{\Delta x}$ are equal, the error of the out-of-plane component is increasing with smaller viewing angles. The ratio of the random errors can be approximately described by

$$\sigma_{\Delta z}/\sigma_{\Delta x} = \tan(\Theta)^{-1} \tag{2.1}$$

CALIBRATION AND DISPARITY CORRECTION

As already mentioned, the quality of the stereo PIV measurement is highly dependent on the accuracy of the mapping functions between the image plane of the two cameras and the object plane. To obtain an accurate mapping function, usually, a calibration target with distinct markers (i.e., checkerboard or dot patterns) is inserted into the measurement area. A planar calibration target asks for an accurate repositioning along multiple positions normal to the plane, which is spanned by the light-sheet, to not only give the mapping functions between image and object plane but also the viewing angles of the cameras, which are required for the reconstruction of the out-of-plane velocity component (Adrian and Westerweel (2011)). To overcome the problems related to an accurate repositioning of the calibration target during the calibration procedure nowadays, precisely machined multi-plane targets are mostly used. If cameras are positioned on opposite sides of the

Figure 2.4: Photograph of a multi-plane calibration target

laser-sheet, a double-sided calibration target can be used. However, its thickness has to be precisely known to later account for the offset with respect to the laser-sheet. Figure 2.4 shows an example of a multi-plane calibration target, used for calibration throughout the measurement campaigns, described in this thesis. It has to be mentioned that with this method, a valid calibration can only be obtained if the front plane of the calibration target is perfectly aligned with the laser-sheet plane or if its relative position with respect to the light-sheet is known. Figure 2.5 (top) shows an ideal setup, where the calibration target front plane is perfectly aligned with the laser-sheet. The alignment of the target with the light-sheet guarantees that the velocity information that is obtained at a certain point within the laser-sheet, is later assigned to the correct point in the de-warped images of both cameras. However, a perfect alignment of the calibration target with the light-sheet is not always possible. A more realistic situation is depicted in Figure 2.5 (bottom left), where the calibration plate has a small offset δz with respect to the light-sheet and is slightly tilted at an angle ϕ. In this case, a particle, and thus also the velocity information, obtained at a certain point P within the light-sheet, is registered at two different locations of the de-warped images. The distance between the particles in the de-warped images is called disparity. In other words, the velocity information that contributes to the calculation of a vector at a certain point in the de-warped images contains information from two different positions of the light-sheet 2.5 (bottom right). The distance of these points within the light-sheet is called *registration error*. While in a uniform flow, the registration error would not influence the final reconstructed vector field, its effect on the final vector field increases with the size of the velocity gradient in the flow.

According to Willert (1997), the resulting mismatch of the back-projected images between both cameras from a misalignment of laser-sheet and calibration target can be quantified by the cross-correlation of these:

$$R_{C1,C2} = Cam_1(t) \star Cam_2(t), \tag{2.2}$$

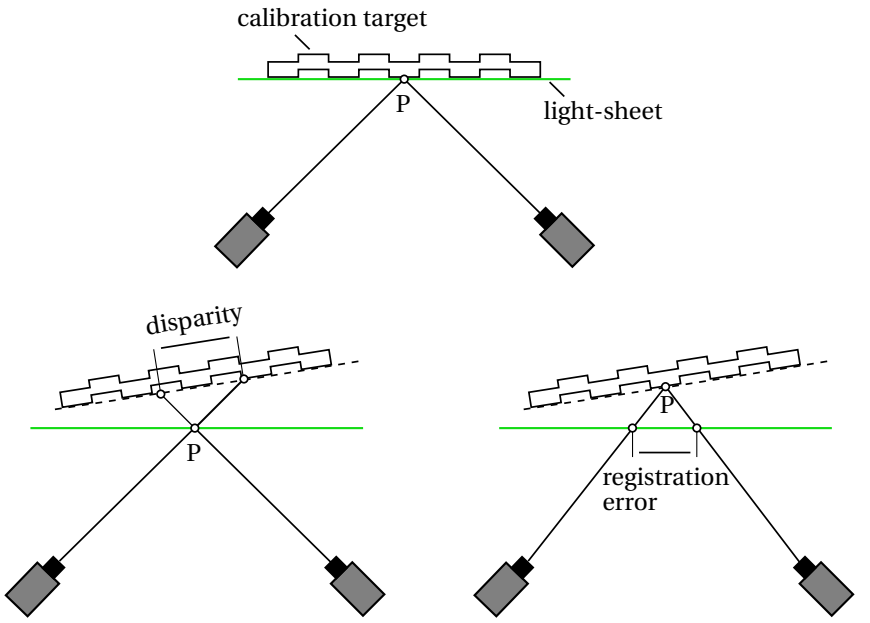

Figure 2.5: Ideal PIV setup with good alignment of calibration target and light-sheet (left). PIV setup with calibration plate and laser-sheet not well aligned and the resulting disparity (right)

with $\star$ being the cross-correlation operator. This results in a description of the spatial distribution of the difference of corresponding particle positions between both cameras called the *disparity-map*. Figure 2.6 shows the principle of the disparity map, obtained from cross-correlation of the images of two different cameras. To correct for this systematic error that is introduced by the misalignment, Willert (1997) proposed to use the obtained disparity map for a correction of the position of the planar vectors of both cameras, before performing the final stereo reconstruction. A more sophisticated method has been proposed by Wieneke (2005), in which the obtained disparity map is used for a correction of the calibration parameters, to obtain a better overlap of the de-warped images. As the method results in a refinement of the initial calibration by using particle images, the method is referred to as self-calibration.

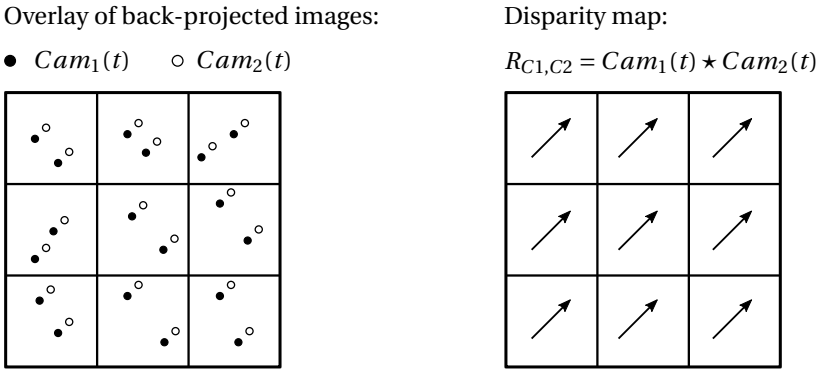

Figure 2.6: Overlay of back projected images from two cameras (left); Disparity map from cross-correlation of both images (right)

2.2. PIV IN TOWING TANK APPLICATIONS

2.2.1. OVERVIEW

To overcome the spatial and operational limitations of pitot tubes and laser Doppler velocimetry and obtain a non-intrusive measurement of the velocity field with high spatial resolution, Dong et al. (1997) first reported the application of the PIV technique in a towing tank facility. By using a single submerged camera and a submerged light-sheet, the two-dimensional velocity field in the bow wave of a ship was obtained, and the vorticity near the free-surface was derived from these measurements. Images were still recorded on a 35 mm film and had to be digitized for further processing and the velocity calculation. These were soon replaced by special digital double-shutter PIV cameras, which made image acquisition and evaluation much easier. First PIV measurements with a digital camera were reported by Gui et al. (2001) and Tukker et al. (2000), both analyzing the wakefield of a ship with a planar PIV system. While the setup of Tukker et al. (2000) was stationary, recording the flow field of the passing ship, the PIV system used by Gui et al. (2001) was fit into a watertight probe which was mounted to the carriage. While the stationary system allowed for only one single measurement at each location along the ship hull, the towed probe can make full use of the whole length of a test run, and multiple vector images can be obtained during a single test run. During the measurements reported by Gui et al. (2001), 200 images were obtained per measurement run. Aiming for a statistical description of the flow, this was a substantial improvement. Considering, that usually a waiting time of approximately 20 minutes is needed in-between single test runs to wait for the residual motions in the basin to be sufficiently damped, the possibility to take multiple measurements per test run, also made the application of PIV systems in towing tanks more efficient. Other studies conducted with the previously presented

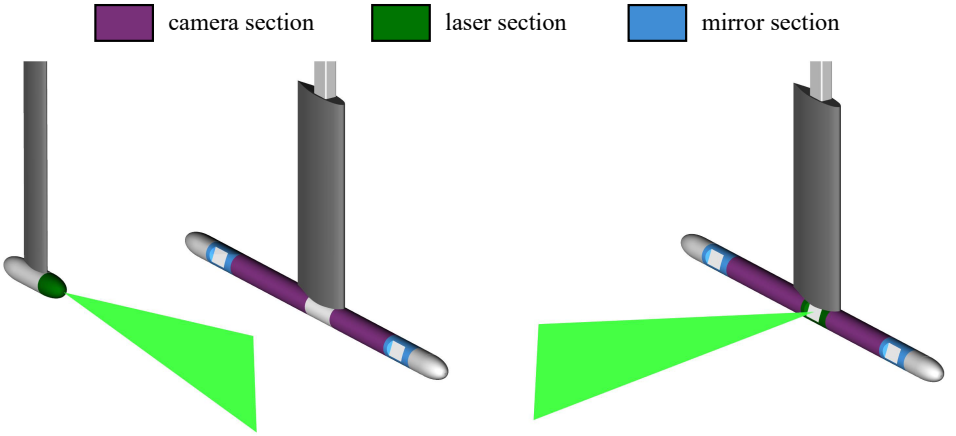

Figure 2.7: Schematic drawing of a modular underwater PIV system and the main system components: Symmetric camera setup with measurement plane aligned with the towing direction (left) and symmetric camera setup with measurement plane perpendicular to towing direction (right).

system are amongst others the phase-averaged measurement of the wake flow a surface combatant DTMB 5512.

Up to this point, all described applications were only able to determine the two-dimensional vector field without the out-of-plane velocity component. To overcome these limitations, Pereira et al. (2003) and later Dautel et al. (2005) and Hallmann et al. (2009) presented similar modular underwater stereo-PIV probe designs. The systems consisted of a torpedo-shaped probe, that contained the two cameras and the laser sheet forming optics. Successful applications are mostly related to wake flow measurements (Anschau and Mach (2012)) and flow field measurements during maneuvering (Falchi et al. (2014) and Jurgens et al. (2006)) or more fundamental studies such as vortex-induced vibrations from an oscillating cylinder (Wilde et al. (2006)). The concept of the submerged stereo-PIV probe proved to be successful, making the torpedo-based stereo-PIV system the state of the art system for most towing tank applications. A variation of the torpedo-based system, with two vertical cylinders in place of a streamlined torpedo, has been presented by Yoon et al. (2015) to investigate the flow around a maneuvering ship model in a phase-averaged manner. Fitting a total of four cameras into the vertical cylinders, the system was later upgraded to a tomographic setup (Egeberg et al. (2014)) for volumetric velocity field measurements.

2.2.2. THE TU DELFT UNDERWATER PIV-SYSTEM

With the torpedo-based stereo-PIV system presented as state of the art, for the measurements which will be presented in this thesis, a modular underwater stereo-PIV-system

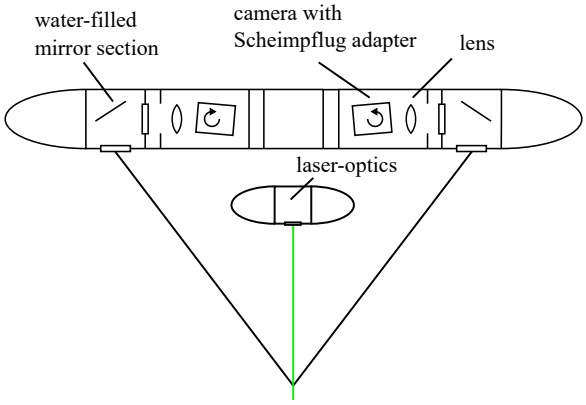

Figure 2.8: Schematic description of the main system components of a torpedo-based underwater system

was rented from LaVision. Figure 2.8 shows the basic modular concept, which is shared by all torpedo-based systems, independent of the system supplier. The depicted example shows a symmetric setup. The cameras are fit into separate camera sections with their optical axis being in-line with the longitudinal axis of the torpedo. The viewing angles are controlled with mirrors. These are located in a separate section, which is filled with water to overcome the problem of different refractive indices of air and water. As mentioned in the previous section, for stereo-PIV systems with an angular displacement of the cameras, the Scheimpflug condition has to be fulfilled to keep the particles across the measurement plane focused. For this reason, the cameras are mounted to a rotation stage to enable a rotation of the sensor plane. To further adjust the viewing angle, the separate modules can be rotated around the longitudinal axis of the torpedo. To guarantee a smooth operation of the system, the Scheimpflug adapter, as well as the focus of the lenses can be remote controlled. The laser beam is guided through a separate strut which contains the sheet forming optics. A plano-concave lens with f=-75 mm in combination with a meniscus lens with f=85 mm is used to adjust the focal point of the light-sheet between 0.3 and 2 m. A cylindrical lens with f=-19 mm is used to form the light-sheet. As the system was a rental system, it could not be fully tailored to the needs of the test campaigns, and the laser strut could not be integrated into the torpedo to form one rigid structure. For the presented test campaigns, different cameras and lasers have been used. Their specifications are given in the description of the respective test setup. A more detailed description of the PIV system components will be given within the following section, where the critical aspects of operating a towed PIV system are discussed.

2.3. CRITICAL OPERATIONAL ASPECTS

While the PIV technique is mostly applied in more controlled laboratory environments, the operation of such a system in a towing tank poses several critical issues. While sufficient optical access is provided by the torpedo configuration, which has been previously presented, the size of the facility and the nature of the observed flows pose additional challenges to the experimentalist. The particularities of a towed PIV system and the critical issues during operation will be discussed in the following, concerning the system components and the operational conditions.

IMAGING AND OPTICS

The different arrangements of the optical components have already been discussed in connection with the description of the underwater probe. The suitable arrangement of the cameras has to be chosen under consideration of the optimal position of the cameras with respect to the measurement area for accurate measurement of the velocity components, but also under consideration of the smallest disturbances due to the PIV system in the measurement area. Jurgens et al. (2006) presented measurements with a symmetric setup. While this arrangement usually gives the lowest error for the out-of-plane velocity component, it was shown with force measurements, that the probe significantly influenced the flow field around the model. Following from this, the footprint of the PIV system has to be reduced to a minimum. A sufficient stand-off distance has to be chosen to guarantee the non-intrusiveness of the technique.

SEEDING

To accurately measure the velocity of the fluid with the PIV technique, tracer particles are needed that accurately follow the flow. In smaller laboratory applications, usually hollow, coated glass spheres are used. However, their uniform size and excellent light-scattering properties come with a high price tag. With the towing tank dimensions being usually in the range of several hundred meters and large cross-sections, large amounts of particles are needed, which makes the use of these particles not very economical. Also, having relatively good light-scattering properties and a relatively narrow range of size distribution, polymer particles, such as Vestosint or Orgasol, provide a cost-effective alternative. These particles can be purchased in large amounts and are available in different sizes of 10 - 60 μm. The application of fluorescent particles is known to prevent reflections from models and bubbles. However, these particles are usually expensive and health-threatening. Ashworth Briggs et al. (2018) recently presented a less expensive alternative to these. Next to the choice of the appropriate particles, also equal distribution of these in the towing tank, as well as a suitable seeding density, is of importance. For this reason, usually, a seeding rake is mounted to the carriage. While seeding during the measurements would disturb the flow field in the towing tank, usually, a retractable

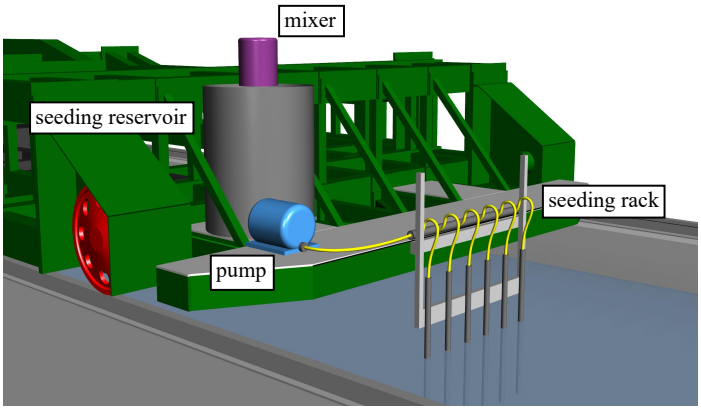

Figure 2.9: Schematic drawing of the retractable seeding rack, mounted in front of the carriage

seeding rake is used for a seeding in-between measurement runs. Figure 2.9 shows a schematic drawing of the seeding system and its main components, mounted to the front of the carriage of the towing tank no.1 of the TU Delft ship hydrodynamics laboratory.

ILLUMINATION

Due to the large size of the facility and the towed ship models, which are usually between three and seven meters long, the region of interest, where the flow field is investigated, also needs to be large. Usual sizes of the area of investigation are approximately 300 x 300 mm^2, but can also be larger. Due to this size and the large stand-off distances of the sheet forming optics to the measurement region, high energy lasers are needed. While for the first presented measurements in a towing tank environment, a laser with a maximum energy of 20 mJ was used, nowadays Nd:YAG lasers up to 200 mJ at a wavelength of 532 nm are common for the application in towing tanks. At these high energies, the maximum repetition rate is usually limited to 7-25 Hz. Higher repetition rates usually come at the cost of a lower pulse energies. The laser, used for the experiments, described in Chapter 5, had a repetition rate of 50 Hz with a maximum pulse energy of 50 mJ.

SYSTEM ALIGNMENT AND STEREO CALIBRATION

One of the major challenges in towing tank applications is the correct alignment of the light-sheet with the measurement plane and the calibration target. As the light-sheet defines the measurement plane, it has to be accurately aligned with the towing tank and model coordinate system. Due to the size of the facility, this problem poses to be non-trivial. Hallmann et al. (2009) proposed several techniques for this. For the alignment of the PIV system with the model Grizzi et al. (2010) proposed the usage of alignment pins, which were temporarily mounted to the model. Also of high importance is the

correct alignment of the calibration plate with the light-sheet, as the calibration target is used to define the mapping function between the towing tank coordinate system and the recorded images. The influence of a misalignment of light-sheet and calibration target on the calculated three-dimensional vector field has already been described in Section 2.1. While the self-calibration method, proposed by Wieneke (2005) can be used to correct for any misalignment of the light-sheet with the calibration target, the fact, that the carriage is performing a unidirectional motion along the rails can be further used to validate alignment and calibration, by measurements of the uniform velocity field, that corresponds to the carriage velocity. Grizzi et al. (2010) even proposed a method where the entire calibration of the system is based on the measurement of this uniform flow field. As important as the alignment of the calibration plate with the laser-sheet, is the determination of the position of the ship model in the recorded images. Therefore, it is proposed to use markers on the model for correct positioning of the PIV system with respect to the object of investigation.

REFLECTIONS AND FEATURE IDENTIFICATION

Another critical issue during the operation of a PIV system is the regular occurrence of light-sheet reflections from the towed ship models. While usually, the flow close to the hull is of interest, these reflections strongly influence the correlation and sometimes even make a correct velocity measurement impossible (Adrian and Westerweel (2011)). To keep reflections from objects at a minimum, the best practice in towing tanks is to paint the model matt black. Tests with fluorescent paint in combination with a suitable narrow band-pass filter with the wavelength of the used laser have also been conducted, but in those cases, only a part of the light from the light-sheet was shifted in frequency and reflections were still visible. While both mentioned options only reduce the intensity of reflections, a measurement in the direct vicinity of the model wall is not possible. Another possibility for these measurements is the construction of the tested object from acrylic glass. However, this is usually restricted to the application with simpler geometrical shapes.

Next to surfaces of an object, light can also be reflected at the interface of different media such as bubbles, entrapped air from breaking waves, and the free-surface. The high light intensities from these reflections may also result in an exceedance of the saturation level on certain locations of the image sensor. In this case, all adjacent pixels are filled with the surplus charge. This phenomenon is called blooming and mostly affects coupled charged device (CCD) sensors. The newer complementary metal-oxide-semiconductor (CMOS) or scientific CMOS sensors are not affected by these problems. While the direction of reflections is not only limited to the plane of the light-sheet, it is also possible that particles, which are not in the designed measurement plane, are illuminated by reflected laser light. To solve a majority of the problems connected to reflections, fluorescent

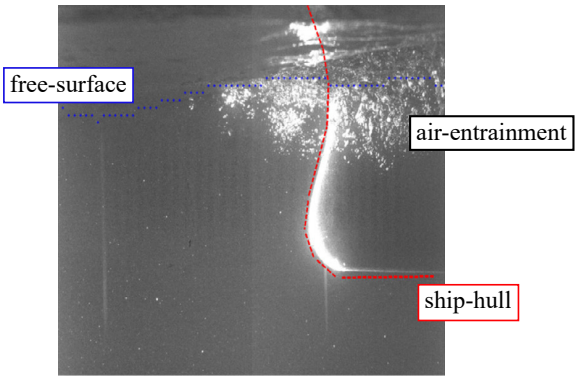

Figure 2.10: PIV recording of the flow field in the bow region of a ship in waves from Dussol et al. (2016), showing the problem of high intensity regions due to air entrainment and reflections of the light-sheet on the ship hull and the problem of the identification of the free-surface.

seeding particles can be used. However, as already mentioned in Section 2.3, these are usually health-threatening and too expensive to be used in large facilities. Figure 2.10 shows a picture of the flow, recorded in the bow region of a ship by Dussol et al. (2016), to investigate the bubble sweep-down in this area. The high light intensities due to air entrainment and reflections on the bow are clearly seen. The red line shows the identified ship hull, which is used for proper masking before the vector calculation. While the previous features could be identified due to the reflections, the free-surface, shown as the blue, dotted line, is not clearly identifiable. However, it needs to be identified to define the measurement region and guarantee a correct vector calculation in this area. The problem of identifying the free-surface will be further discussed in Chapter 5, where a free-surface identification method for time- and phase-averaged flow is presented.

2.4. HIGH-SPEED RELATED ERROR SOURCES

The previously described critical issues summarize the experience of approximately 20 years of conducting PIV measurements in towing tanks after the first application in a towing tank in 1997 (Dong et al. (1997)). While most reported studies were conducted at low carriage speeds, the study of high-speed ships and the herewith associated high carriage velocities pose some additional problems which have so far not been discussed in connection with towing tank applications: structural vibrations and high-out-of-plane velocities. The critical issues related to these will be discussed in the following.

2.4.1. STRUCTURAL VIBRATIONS

Towing tank carriages generally move on two rails that are located on either side of the tank. To guarantee that the position of the towed model with respect to the water surface does not change over the length of the test section, the rails are carefully aligned with a laser. However, as both the rails, as well as the wheels, are build from metal, without any damping material in between, the smallest imperfections will excite the carriage and result in structural vibrations, which are likely to increase with increasing carriage speed. As the ship model is mounted under the center of the carriage, the magnitude of the vibrations is likely to increase in this region, with a shift to a lower frequency range. Being an optical measurement system, the accuracy of a PIV system is highly dependent on an initial calibration, and any change of position of the system components, i.e., cameras and light-sheet with respect to this reference position will result in invalid measurement results. Novara et al. (2015) analyzed the effect of structural vibrations on the PIV recording accuracy for the operation of a PIV system in an industrial wind-tunnel facility. The vibrations were found to result in large fluctuating disparities in the images between different cameras, due to a displacement of the PIV system components with respect to each other. As already described in Section 2.1 for the misalignment of the calibration target with the light-sheet, this results in a registration error, where the velocity information from two different locations in the light-sheet is used for the final reconstruction of the velocity vector. A simplified example of the effect of a displacement of the cameras after an initial calibration on the disparity and the resulting registration error is shown in Figure 2.11. After the initial calibration, in which the light-sheet is perfectly aligned with the calibration target, both cameras are moved in the normal direction of the light-sheet to two different locations. This results in a shift of the coordinate systems of the back-projected images. Figure 2.11 (left) shows both cameras looking at the same particle in the light-sheet. As a result of the shift of coordinate systems, the particle appears at two different locations in the back-projected images. Figure 2.11 (right) shows the same setup, but in this case, the velocity information is evaluated at the same point of the different coordinate systems. In the initial calibration, both cameras retrieve velocity information from the same particle in the light-sheet. In case of a displacement of the cameras and a shift of the coordinate system, it is seen that both cameras retrieve velocity information from different locations of the light-sheet. In case of a vibrating setup, this results in a time-dependent registration error. As described in section 2.1, the disparity in the images of different cameras can be obtained by evaluating the cross-correlation of these, which eventually can be used for a correction of the initial calibration (Wieneke (2005)). Due to the application of a self-calibration for every time-step, the vibrations of the cameras with respect to each other and with respect to the light-sheet can be compensated for. However, while it is proposed to use an average disparity of multiple recordings for accurate correction of the initial calibration, this is not possible here, as the disparity might change in between

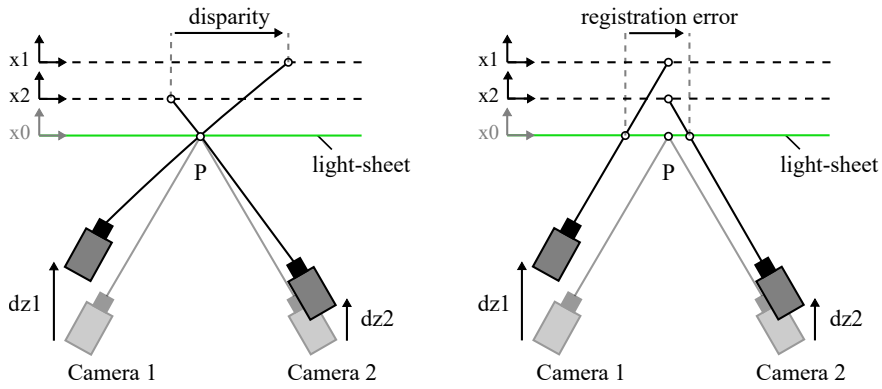

Figure 2.11: Schematic description of the effect of a displacement of the cameras after an initial calibration on the disparity (left) and the registration error (right).

time-steps. To reduce the effect of vibrations on the inter-camera displacements and the displacement with respect to the light-sheet, a stiff connection between cameras and laser optics has to be ensured. This requirement is fulfilled when all system components are fit into the torpedo-shaped probe. However, some setups do not allow this kind of configuration. While the stiff connection in-between system components increases the accuracy of the measurement system itself, it does not correct for a displacement of the measurement system with respect to the measurement plane.

2.4.2. LARGE OUT-OF-PLANE VELOCITIES

The flow field, to be investigated in towing tank tests, often has a strong three-dimensional characteristic. Unless using a tomographic PIV system, where the volumetric flow field is measured, PIV measurements are restricted to the plane, spanned by the light-sheet. This inevitably results in an out-of-plane velocity component. As the orientation of the light-sheet is often perpendicular to the towing direction, i.e., for the observation of vortical structures, the out-of-plane velocity component is often the largest velocity component. In single-camera systems, any out-of-plane motion of the particles resulted in erroneous in-plane components (Prasad (2000)). This so-called perspective error restricted the measurement with these systems to two-dimensional flows. The problem was overcome with stereo-PIV systems, where this error was eliminated due to a reconstruction of the complete three-dimensional velocity vector. However, due to the planar nature of the method, a large out-of-plane particle motion still influences the measurement accuracy. Due to the limited thickness of the light-sheet, a high out-of-plane velocity component strongly influences the correlation peak signal strength. Assuming a Gaussian distribution of the intensity across the thickness of the light-sheet, a particle that travels across the

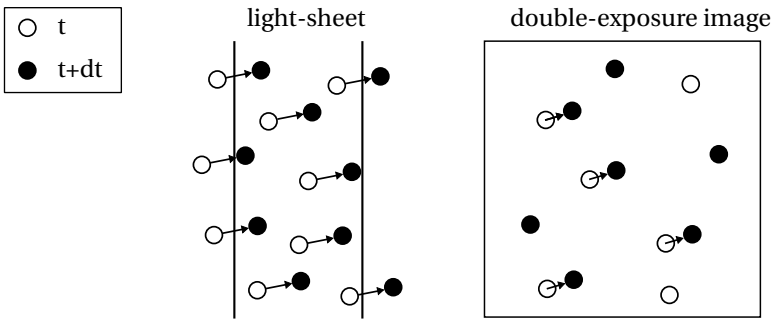

Figure 2.12: Schematic description of the introduction and loss of particles due to high out-of-plane velocities

light-sheet may change its intensity in-between pictures. Additionally, particles disappear, as they leave the light-sheet, and new particles will be visible as they enter the sheet (see Figure 2.12). As shown in Adrian and Westerweel (2011), the correlation peak amplitude is proportional to the out-of-plane loss of correlation. The random error that results from this is often one of the dominant error sources (Wieneke (2017)). To constrain the out-of-plane loss of particles, it has to be guaranteed that less than one-quarter of the particles leave the light-sheet in-between two laser pulses (Adrian and Westerweel (2011)). According to Scharnowski et al. (2017), it has to be ensured that the number of particle image pairs N should not be less than N<5 in every correlation window. To limit the out-of-plane loss of particles according to Raffel et al. (2018), several recording parameters can be adjusted. However, all adjustments also come with disadvantages. One possibility to limit the motion of particles across the light-sheet is the adjustment of the time between two laser pulses Δt. As the velocity is reconstructed from the displacement of the particles over a certain time, this results in a reduced dynamic velocity range, not only of the out-of-plane velocity component but also of the in-plane components. Another option would be to increase the thickness of the light-sheet. However, as the energy density reduces proportionally to the light-sheet thickness, this will again result in a lower correlation signal strength. While measurements at high carriage speeds often ask for a large dynamic range, the previously mentioned limitations will ultimately result in a lower resolution if the largest velocity component is perpendicular to the light-sheet. Whenever the setup and test-case allows an alignment of the light-sheet with the main flow direction, this problem can be avoided. The use of a multi-pass interrogation with an offset of the correlation windows significantly reduces the in-plane loss of correlation (Westerweel et al. (1997)). The offset is hereby detected from the displacement estimate of the previous iteration. This allows for much larger pixel-shifts and increases the dynamic range of the measurement.

3

PRESSURE RECONSTRUCTION FROM VELOCITY FIELDS

The previous chapter has described the capabilities of the PIV technique to capture the kinematic characteristics of the flow field. However, as mentioned in Section 1, for the study of high-speed craft hydrodynamics, often the hydrodynamic pressure distribution in the flow field, as well as on the surface of the investigated object is of interest. The well-established techniques, such as pressure sensors for surface pressure measurement or pitot-probes for the measurement of the pressure in the flow field, often suffer from either low spatial resolution or are intrusive. In aerodynamic applications, the usage of pressure-sensitive paint (PSP) is a common means to accurately measure the pressure distribution on a surface with a high resolution (McLachlan and Bell (1995)). This cannot be considered as an option for towing tank applications, where due to the incompressibility of the fluid, this technique can only detect the oxygen concentration (Sakaue et al. (2009)), but no pressure. With the Navier-Stokes equations describing the relationship between the kinematic and dynamic flow properties, an alternative approach is the reconstruction of the pressure field from the measured velocity field, and its obtained derivatives, using this relationship. First applied in the late 90s by Jakobsen et al. (1997), pressure reconstruction from PIV measurements became more and more popular and is nowadays well studied and widely accepted in numerous aerodynamic and hydrodynamic applications. The general principle of the technique will be discussed in the following, together with an introduction of the basic equations.

3.1. GENERAL APPROACH

Having obtained the velocity field with the PIV technique, the relation of the measured velocities, their spatial and temporal derivatives, and the pressure gradient, is given by the momentum equation. Under the assumption, that the flow is incompressible, the divergence-free condition holds, i.e., $\nabla \cdot u = 0$ and the momentum equation can be written as:

$$\frac{Du_i}{Dt} = -\frac{1}{\rho}\frac{\partial p}{\partial x_i} + \nu \frac{\partial^2 u_i}{\partial x_j \partial x_j} \tag{3.1}$$

Considering the later implementation of the technique, the flow is looked at from an Eulerian perspective and the material acceleration is split into the local and convective acceleration.

$$\frac{Du_i}{Dt} = \frac{\partial u_i}{\partial t} + u_j \frac{\partial u_i}{\partial x_j} \tag{3.2}$$

Resulting from this, the pressure gradient can be described as:

$$\frac{\partial p}{\partial x_i} = \rho \left(-\frac{\partial u_i}{\partial t} - u_j \frac{\partial u_i}{\partial x_j} + \nu \frac{\partial^2 u_i}{\partial x_j \partial x_j} \right) \tag{3.3}$$

For the reconstruction of the pressure field, Equation 3.3 has to be integrated. Starting from a single point, or area, where the reference pressure is known, the pressure field is found through spatial marching. To reduce the accumulation of errors during spatial integration, different marching schemes have been proposed. However, all methods follow the same basic principle.

An alternative solution opens up, when applying the divergence operator to the momentum equation 3.3.

$$\frac{\partial}{\partial x_i}\left(\frac{\partial p}{\partial x_i}\right) = \rho \frac{\partial}{\partial x_i}\left(-\frac{\partial u_i}{\partial t} - u_j \frac{\partial u_i}{\partial x_j} + \nu \frac{\partial^2 u_i}{\partial x_j \partial x_j} \right) \tag{3.4}$$

This gives a Poisson equation, which can be solved with the help of appropriate boundary conditions. Under consideration of the divergence-free condition $\nabla \cdot u = 0$, the local acceleration and the viscous term disappear and the pressure Poisson equation further reduces to:

$$\frac{\partial^2 p}{\partial x_i^2} = -\rho \frac{\partial}{\partial x_i}\left(u_j \frac{\partial u_i}{\partial x_j} \right) \tag{3.5}$$

The disappearance of the acceleration and viscous term, does not mean, that their influence is neglected, as they will still be present in the boundary conditions. These can be either of Dirichlet or Neumann type. The latter condition is obtained from the momentum equation (3.3) to prescribe the non-homogeneous pressure gradient at the boundary

of the measurement area:

$$n_i \cdot \frac{\partial p}{\partial x_i} = -\rho n_i \cdot \left(\frac{\partial u_i}{\partial t} + u_j \frac{\partial u_i}{\partial x_j} - \nu \frac{\partial^2 u_i}{\partial x_j \partial x_j} \right) \tag{3.6}$$

with n_i being the normal vector of the domain boundary. Dirichlet type boundary conditions can be applied at boundaries, where the pressure is known, this can be the pressure of the undisturbed flow, or even a reference pressure obtained from additional measurements.

The performance of both methods, the direct integration and the solution of the Poisson equation, has been compared by several authors. A summary of the advantages and disadvantages of both methods is given by Van Oudheusden (2013). The performance of both methods often depended on the case of application. However it was often reported, that due to the accumulative error due to the spatial marching scheme, the direct integration is more sensitive to measurement noise (Albrecht et al. (2012)). For this reason in this thesis, the Poisson approach has been chosen to reconstruct the pressure field.

3.2. TIME AND PHASE-AVERAGED PRESSURE FIELDS

Given the planar character of most PIV measurements, even with a stereo-PIV setup, the out-of-plane gradient cannot be measured. For a full description of the flow field and all spatial gradients, a tomographic PIV setup would be necessary. Following from this, the technique is mostly applied to two-dimensional flows, or problems, where the out-of-plane gradient is negligible (Van Oudheusden (2013)). However, being often interested in the time-averaged flow and its pressure field, i.a. the validation of CFD codes, the time- or phase-averaged volumetric flow field can be reconstructed from multiple planar measurements. Ragni (2012) presented the reconstruction of the phase-averaged volumetric flow field around a propeller blade from multiple planar measurements and a reconstruction of the pressure in the flow field and on the propeller surface (Figure 3.1).

Having obtained the mean velocity field and its fluctuations from the statistical ensemble of the recorded velocity fields, one can derive the Reynolds averaged momentum equation. The formulation is based on the assumption, that the flow variables, velocity and pressure, consist of an average and a fluctuating part:

$$u(x,t) = \overline{u} + u'(x,t) \tag{3.7a}$$

$$p(x,t) = \overline{p} + p'(x,t) \tag{3.7b}$$

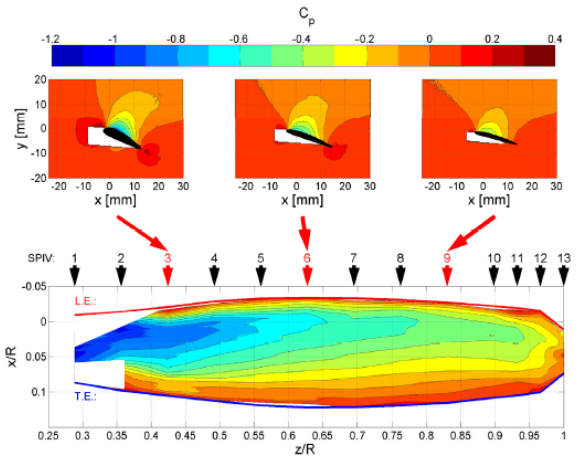

Figure 3.1: Time-averaged pressure distribution in the flow field and on the surface of a propeller blade, reconstructed from multi-plane PIV measurements (from Ragni (2012))

Given, that $\overline{u'} = 0$, the Reynolds-averaged momentum equation is

$$\overline{u}_j \frac{\partial \overline{u}_i}{\partial x_j} = -\frac{1}{\rho}\frac{\partial \overline{p}}{\partial x_i} + \nu \frac{\partial^2 \overline{u}_i}{\partial x_j \partial x_j} - \frac{\partial \overline{u'_i u'_j}}{\partial x_j} \tag{3.8}$$

While the temporal derivative vanishes, an additional term is introduced due to the Reynolds-averaging procedure, the Reynolds stress tensor which can be obtained from the variances and co-variances of the measured velocity vectors. The application of the divergence operator to Equation 3.8 gives the modified Poisson equation:

$$\frac{\partial^2 \overline{p}}{\partial x_i^2} = -\rho \frac{\partial}{\partial x_i}\left(\overline{u}_j \frac{\partial \overline{u}_i}{\partial x_j} + \frac{\partial \overline{u'_i u'_j}}{\partial x_j} \right) \tag{3.9}$$

To solve the Poisson equation a Neumann boundary condition is obtained from the Reynolds averaged momentum equation 3.8 to prescribe the non-homogeneous pressure gradient at the boundary of the measurement area:

$$n_i \cdot \frac{\partial \overline{p}}{\partial x_i} = -\rho n_i \cdot \left(\overline{u}_j \frac{\partial \overline{u}_i}{\partial x_j} - \nu \frac{\partial^2 \overline{u}_i}{\partial x_j \partial x_j} + \frac{\partial \overline{u'_i u'_j}}{\partial x_j} \right) \tag{3.10}$$

In case of phase-averaging, the temporal average is replaced by ensemble average and the temporal velocity derivative, becomes the derivative of the ensemble-averaged velocity with respect to the phase-angle ω. This has to be considered when using a

Neumann boundary condition

$$n_i \cdot \frac{\partial \overline{p}}{\partial x_i} = -\rho n_i \cdot \left(\frac{\partial \overline{u}_i}{\partial t} + \overline{u}_j \frac{\partial \overline{u}_i}{\partial x_j} - \nu \frac{\partial^2 \overline{u}_i}{\partial x_j \partial x_j} + \frac{\partial \overline{u'_i u'_j}}{\partial x_j} \right) \tag{3.11}$$

For the solution of the previously described equations, the C++ toolbox OpenFOAM (Open Field Operation and Manipulation) is used, which is released as free and open-source software under the GNU General Public License. The toolbox provides a development package for customized numerical solvers, and utilities for the solution of continuum mechanics problems with a focus on fluid dynamics. The equations are discretized with the finite-volume method.

4

THE APPLICATION OF PIV FOR THE ANALYSIS OF INTERCEPTOR HYDRODYNAMICS

The previous chapter has presented the main principles of PIV measurements and identified possible sources that affect the accuracy of measurements in towing tanks, especially at higher carriage speeds. To further study the feasibility of performing pressure PIV measurements in towing tanks, this chapter presents the first application of the proposed technique for studying the hydrodynamics of high-speed crafts. Especially when operating a towing tank carriage at high speeds, the measurement setup can be exposed to significant structural vibrations. As outlined in Chapter 2, the PIV technique, being an optical measurement technique, is sensitive to any displacement of the cameras after initial calibration, which ultimately leads to an erroneous vector calculation. It has been shown for stereo-PIV systems, where the three-component vector field is reconstructed from the images of two cameras, that the errors due to an erroneous reconstruction are one of the main sources of uncertainty. While the reconstruction error is not noticed in flows with small velocity gradients, it especially affects the vector calculation of flows with high velocity gradients (Van Doorne et al. (2004)). For determining the accuracy of the pressure PIV technique, the effect of vibrations on image acquisition needs to be quantified, and where necessary, a correction procedure needs to be applied to minimize

Parts of this chapter have been published in Int. Conference on Hydrodynamics, Jacobi et al. (2016), and Journal of Ocean Engineering, Jacobi et al. (2019b).

the disparity between the recorded images. To investigate the performance of the pressure PIV technique under the previously described conditions, this chapter describes PIV measurements, which were performed in the transom region of a high-speed craft. The vessel is equipped with an interceptor to create a stagnating flow, associated with a high pressure peak at its transom. The flow close to the ship hull is captured with an underwater stereoscopic PIV system, and the pressure peak in front of the interceptor is reconstructed from time-averaged velocity fields. As shown by Brizzolara (2003), the pressure peak highly depends on the characteristics of the boundary layer, which makes this test case predestined for the analysis of the previously mentioned aspects. The chapter will discuss the reconstruction of 2d pressure fields in the center-plane of the model from planar PIV measurements showing the effect of different interceptor heights. To capture the 3d effects of the flow on the pressure distribution in front of the interceptor, multi-plane PIV measurements are performed, and a volumetric flow field is reconstructed from a total of 15 measurement planes. Next to an analysis of the structural vibrations and their influence on the recorded images, a correction procedure is proposed to correct for these. Furthermore, the spatial variation of the measurement uncertainty is analyzed and propagated to the pressure field uncertainty. A comparison with numerical results from steady Reynolds Averaged Navier Stokes (RANS) simulations will finally evaluate the potential of the pressure PIV method to be a valid approach for the validation of CFD codes.

4.1. TEST CASE: HYDRODYNAMICS OF INTERCEPTORS

To investigate the possibilities of capturing the dynamic aspect of the flow around ships and loads on the ship hull, the pressure PIV technique will be applied to flow measurements in the direct vicinity of a ship model. The measurements are conducted in the transom region of a generic hull of a planing vessel with a flat bottom aft section. The transom of the model is equipped with an interceptor, which behaves comparably to a forward-facing step. When deployed at high speeds, the interceptor blade creates a stagnation region on the bottom of the hull in front of the transom, which is associated with a high pressure peak. Typical blade heights are of the order of magnitude of the boundary layer thickness. A schematic drawing of the interceptor and its influence on the boundary layer flow and the wall pressure distribution is depicted in Figure 4.1. Mainly used in static configurations, the generated lift is used to influence the trim of a ship. By dynamically changing the height of the interceptor, it is also used for active ride-control of fast ships in waves.

The flow around interceptors and the resulting hydrodynamic forces are well studied with numerical methods by Brizzolara (2003) and Villa and Brizzolara (2009) with potential and RANSE methods. Molini and Brizzolara (2005) also discussed the 3d effects of an

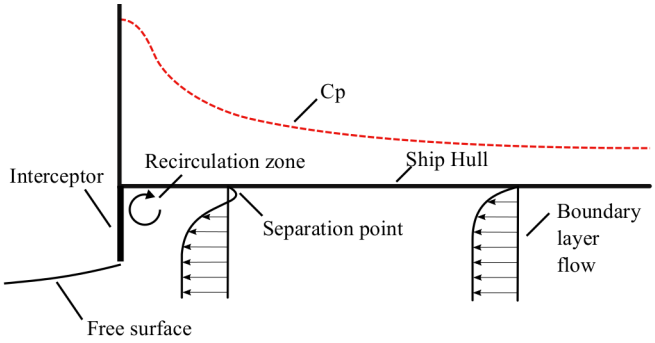

Figure 4.1: Schematic drawing of the boundary layer flow and wall pressure distribution in front of an interceptor (add picture of ship with interceptor next to interceptor principle)

interceptor with a finite span. However, 3d results were obtained without taking the influence of the boundary layer into account. A more recent study has been undertaken by Pearce and Brandner (2014) who compared analytical and potential methods to predict the cavitating flow over a wall-mounted fence. On the experimental side, segmented model tests have been performed by Rijkens et al. (2013) to investigate the hydrodynamic characteristics of different interceptor configurations. Mansoori and Fernandes (2015) performed a more fundamental analysis by experimentally and numerically analyzing the performance of an interceptor, which was mounted to a flat plate.

4.2. EXPERIMENTAL SETUP

The PIV experiments are conducted in the large towing tank of the ship hydrodynamics laboratory at the Delft University of Technology. The tank has a cross-section of 4.22 m width and 2.5 m depth over a test section length of 142 m. The carriage can operate at a maximum speed of 7 m/s. A model of a generic planning hull with an overall length of 1.8 m is used in this study (Figure 4.2). The same model has already been used by Rijkens et al. (2013) to experimentally study the hydrodynamic performance of interceptors and transom flaps for the motion control of fast ships during segmented model tests. Its transom section has a simple box shape with a constant cross-section being 0.4 m wide and 0.8 m long. To provide optical access to the measurement area for illumination with the laser-sheet, the bottom of the segment is replaced by an acrylic glass plate. The bow segment is designed from developable surfaces with the purpose to divert the flow to the transom segment smoothly. At the transom of the model, an interceptor of adjustable height is attached. Manufactured from a simple plate, the interceptor covers the whole beam of the model. Four guiding rails guarantee a smooth and accurate setting of the interceptor intrusion height. To accurately position the model within the field of view of the PIV system and to set it to its correct running trim and sinkage, the model is mounted

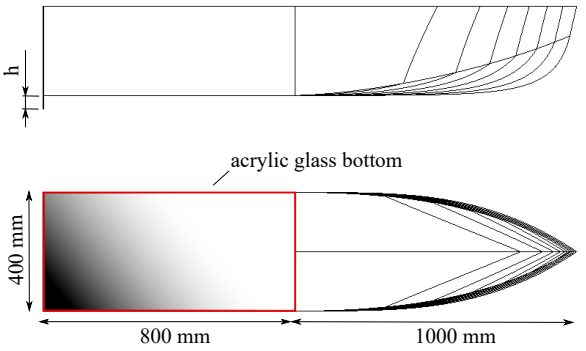

Figure 4.2: Schematic drawing of the ship model used during the experiments

	2D	3D	Unit
Speed	3,4,5	3,4	[m/s]
Trim angle	3.0	3.0	[deg]
Interceptor deflection	0,5,10,15,20	10,20	[mm]
Measurement plane y position	0	0-100 $\Delta y = 20$ 100-180 $\Delta y = 10$	[mm]

Table 4.1: Test parameters for 2D and multi-plane 3D measurements

to the carriage via a Symmetrie NOTUS hexapod. With its linear travel range of ±250 mm, it was also used to reposition the model in between runs during the scanning PIV tests and makes an extra traversing system for the PIV system obsolete. For all test runs, the model is kept at a constant draft of 50 mm and constant bow-up trim of 3 degrees, resulting in a wetted length of 1.52 m. For the 2d PIV measurements in the center-plane of the model, test runs with carriage speeds of 3, 4, and 5 m/s are performed, while the interceptor intrusion height is step-wise increased from 0 mm up to 20 mm with increments of 5 mm. The carriage speeds are equivalent to length based Froude numbers of 0.71, 0.95, and 1.19. Reynolds numbers, based on the wetted length of the ship, range from $5.44 \cdot 10^4$ to $9.0 \cdot 10^5$. A volumetric reconstruction from scanning PIV measurements is obtained for selected conditions at speeds of 3 and 4 m/s with interceptor heights of 10 and 20 mm. To capture the three-dimensionality of the flow field, the model position is shifted in the transverse direction between runs, resulting in a total number of 14 measurement positions from the center plane to the side of the model. As the three-dimensionality of the flow is expected to increase with increasing distance from the center plane, the spacing in-between measurement planes is reduced from 20 mm in the center plane to 10 mm at the side of the model. A summary of the parameters for both, 2d and 3d measurements is listed in Table 4.1

4.2.1. PIV SETUP

The flow in the vicinity of the interceptor is investigated with an underwater stereoscopic PIV setup. To minimize reflections from the bottom of the ship hull and increase the near-wall resolution, the laser head and optics are placed above the water, and the laser sheet is guided through the acrylic glass bottom of the model to the field of view. The two cameras are each located in a watertight torpedo-shaped housing. To get optical access to the region in front of the interceptor, the cameras are located approximately 680 mm in front of the transom, looking backward to the field of view with a 60-degree mirror section. A symmetric arrangement with one camera on either side of the light-sheet is used to accomplish a high accuracy determination of the out of plane velocity component. Furthermore, in this configuration, the cameras were within the forward scattering direction of the laser light. To prevent any disturbance of the flow in the measurement region, the struts which connect the torpedo to the carriage are positioned as far aft as the transom of the ship model and have a streamlined shape. The immersion depth of the torpedoes is 490 mm, and their horizontal stand-off distance is 1000 mm. Figure 4.3 shows a schematic drawing of the PIV setup indicating the position of the cameras and measurement planes. A photograph of the underwater setup, as well as the position of the laser head and the optical setup above water, is shown in Figure 4.4. For the illumination of the measurement plane a Litron Bernoulli Nd:YAG laser with 200 mJ/pulse energy at a wavelength of 532 nm is used. Image acquisition was done with two LaVision Imager Pro SX cameras with a sensor size of 2448 x 2050 pixels and 12-bit color depth. Equipped with lenses of 28 mm focal length, the field of view was approximately 200 x 200 mm^2. To keep the particles focused over the whole field of view, a Scheimpflug-adapter is mounted in front of each camera. With a pixel pitch of 3.45 μm, the digital resolution is approximately 10 pixels/mm. Images are recorded at a double frame acquisition rate of 7 Hz, resulting in 210 image pairs per measurement run at the lowest speed and 120 image pairs at the highest speed. Calibration of the cameras is done with a two-level double-sided 3d calibration plate, which is carefully aligned in an iterative process with the moving direction of the carriage. Mounting the calibration plate to the hexapod enables accurate repositioning of the plate during the calibration process. To guarantee uniform distribution of the 50 μm polymer (Vestosint) particles in the measurement area, a retractable seeding rake is mounted in front of the carriage. Before releasing the particles into the towing tank in-between measurement runs, they are premixed in a high shear flow to prevent clustering. While after every measurement run, the tank is reseeded, a waiting time of 25 minutes allows the water to settle in between runs. Data acquisition is done using the commercial software package DaVis 8.4.0.

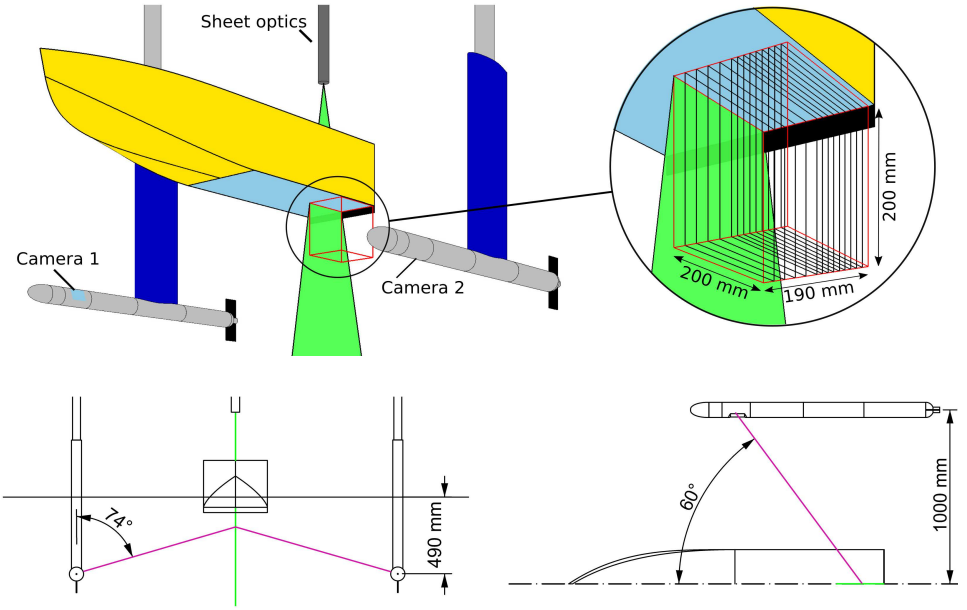

Figure 4.3: Schematic drawing of the PIV setup

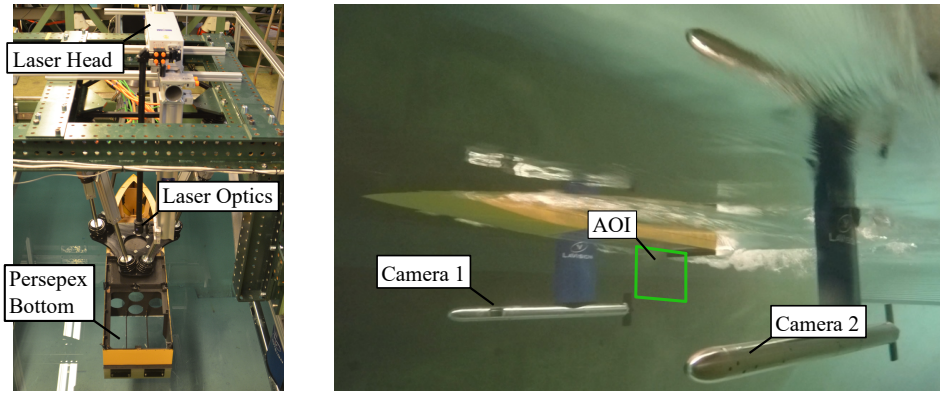

Figure 4.4: Photo of PIV setup

4.3. PIV PROCESSING

To get an impression of the recorded images, Figure 4.5 shows a particle image, recorded with camera 1 and dewarped to the world coordinate system with the previously obtained calibration parameters. At the top of the picture, one can see the reflections within the acrylic glass bottom of the ship model, through which the laser-sheet is guided to illuminate the measurement area. In the top-left corner the interceptor can be identified, which in this case has an intrusion height of 20 mm.

As described in Chapter 2, the PIV system, being an optical measurement system, is sensitive to structural vibrations, which produce a displacement of the PIV system components. From aerodynamic applications in wind-tunnel facilities, it is known that these vibrations can have a significant influence on the measurement quality. Novara et al. (2015) quantified the vibration characteristics of a multi stereo PIV setup in an industrial wind-tunnel facility and reported pixel shifts in between images of up to 10 pixels. While using a cross-correlation window size of 18 pixels, such high fluctuations of disparity were found to have a significant influence on the reconstructed velocity field. This so-called registration error, which is introduced due to a mismatch of the images in the stereo reconstruction process, is typical for stereo-PIV applications and is one of the largest error sources in stereo-PIV applications. A detailed overview of the registration error and the influence vibrations on the stereo-reconstruction has been given in Section 2.2.

As the PIV system in the present study is operated at high towing tank carriage speeds up to 5 m/s, it is also expected that structural vibrations of the carriage will result in a time-varying displacement of the imaging components, ultimately affecting the measurement quality. With both cameras placed in separate struts on either side of the ship model and the laser head above the model, the present setup is thought to be prone to vibrations, as the single system components are not rigidly connected with each other. From an initial visual inspection of recorded images, this can be confirmed, observing a change of position of significant features such as ship bottom and interceptor in the images. To analyze whether the disparities due to vibrations exceed the maximum acceptable level, which has been defined as half the particle image size, the level of vibrations needs to be quantified, and if necessary, a correction procedure needs to be applied to reduce the disparity in-between images. As this is of the order of a correlation window, not applying the shift correction would strongly influence the results in regions with strong gradients.

4.3.1. VIBRATION ANALYSIS AND CORRECTION

As already described in Chapter 2, the misalignment of the recombined images from two cameras can be obtained by the cross-correlation of these. For clarity Equation 2.2 is rewritten here:

$$R_{C1,C2} = Cam_1(t) \star Cam_2(t) \tag{4.1}$$

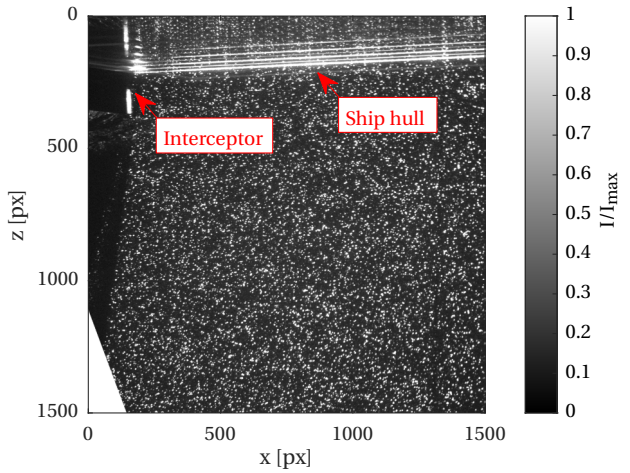

Figure 4.5: Dewarped raw particle image

Using the resulting disparity map $R_{C1,C2}$, Wieneke (2005) proposed a self-calibration procedure to correct the calibration coefficients from an initial calibration for a static misalignment. As discussed in Section 2.1, under the assumption of a laboratory environment, where light-sheet and cameras do not move with respect to each other during the measurements, this method can completely correct for any disparity caused by a misalignment of laser-sheet and calibration plate. When applying the self-calibration procedure to the recorded data sets, a mean disparity between both cameras can be found, which is used to correct for any initial misalignment of the images that is caused by a misalignment of the laser-sheet and the calibration plate. However, as seen in Figure 4.6, a time-varying residual disparity is left. The figure shows the result of the application of Equation 4.1 to the images of representative runs at 1, 3, and 5 m/s after an initial self-calibration has been performed. By looking at the time traces of the disparity amplitudes in Figure 4.6 (left), large temporal fluctuations can be observed, which increase with the carriage speed. A clearer picture of the level of vibrations is given by the box-whisker-plot in Figure 4.6 (right), which summarizes the statistics of the test runs, each consisting of 100 image pairs. While the line within the box indicates the mean level of vibrations, the box indicates the interquartile range, which contains 50 % of the measured values and is bounded by the upper and lower quartile. The whiskers extend to the most extreme values, which are not considered to be outliers. These are plotted separately and are defined as deviations from the mean, which are larger than 1.5 times the interquartile range. At 1 m/s, the residual mean disparity, as well as 50 % of the obtained disparities, are well below 1 pixel. Maximum outliers are found to be in the range of 2 pixels and are thus still within the

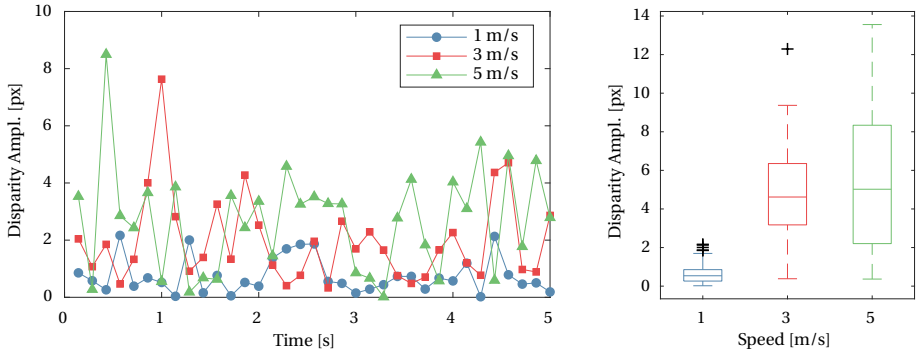

Figure 4.6: Temporal fluctuations of the disparity amplitude

acceptable range of half the particle image size, which in this case is approximately 4 pixels. As the carriage speed is increased, to 3 and 5 m/s, the level of structural vibrations increases, and with these also the mean level of disparities. The mean disparity amplitude at both speeds is in the range between 4 and 5 pixels. However, the upper level of the interquartile range reaches up to 8 pixels at 5 m/s. Maximum disparities of approximately 13 pixels can be found at these high carriage speeds. In both cases, the acceptable level of disparity in-between images from both cameras is exceeded.

While having analyzed the disparity between cameras with the cross-correlation of particle images, taken at the same instant of time, the same technique can also be applied to analyze the shift of images, recorded with the same camera. This will be done by cross-correlating the first frame of every recorded set, with the n-th frame, recorded with the same camera.

$$R_{t0,tn} = Cam_i(t(0)) \star Cam_i(t(n)) \tag{4.2}$$

However, in the previous approach, correlated images would see the same particles. As the particle position changes with time, particle images cannot be used to find the temporal shift of images. Instead, a feature is needed within the field of view, which does not change position over time and is present in every recorded frame. Therefore, only a region of 128 x 128 pixels around the interceptor is used for correlation, which contains as well reflections on the interceptor, as well as reflections on the hull bottom. The proposed procedure is applied to three representative runs at 1, 3, and 5 m/s for both cameras. Results from this feature-based correlation are presented in Figure 4.7. The correlation is always performed with the first exposure of a double frame image. Figure 4.7 (left) shows the time traces of image shifts, obtained from the feature-based cross-correlation of camera 1. The level of vibrations detected with this approach is comparable to the disparities shown in Figure 4.6 and increases with increasing carriage speed. The statistics of the time traces of both camera 1 and camera 2 are again summarized in a box-whisker-plot in Figure 4.7 (right).

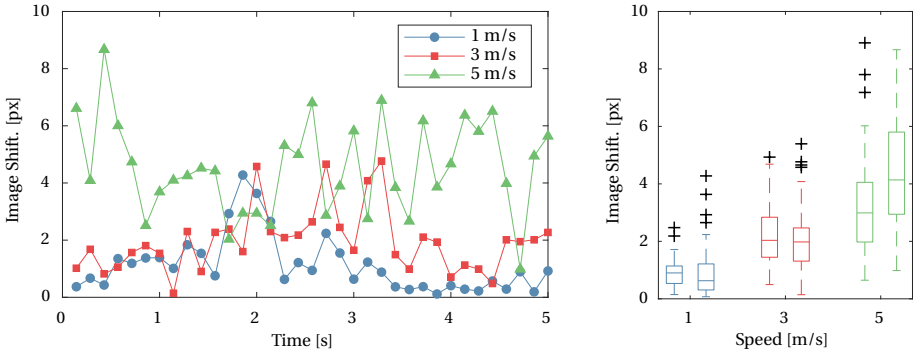

Figure 4.7: Image shift with respect to the first image for camera 1

While at 1 m/s, the mean detected image shifts of both cameras are well below 1 pixel, a few outliers were found where image shifts larger than 2 pixels were detected. Looking at the obtained values at 3 and 5 m/s, the mean amplitude of detected image shifts linearly increases with increasing speeds. At 5 m/s the mean detected image shift is similar to the detected disparity in Figure 4.6. However, the maximum detected shifts are smaller than the detected disparities. This can be seen even more clear by looking at the 3 m/s run. The detected mean disparities and maxima are approximately 50 % smaller than the disparities in-between cameras. As the cameras are mounted to different locations of the carriage and are not rigidly connected, the cameras can move in opposite directions. In this case, the shift of both cameras adds up to a disparity that can be significantly larger than the detected shift of a single camera.

From both the particle-based, as well as the feature-based analysis of vibrations, it can be concluded, that the PIV setup is affected by structural vibrations if the carriage is operated at speeds equal to or higher than 3 m/s. Thus, next to an initial self-calibration, additional effort is needed to reduce the effect of vibrations on the recorded images.

The correction approach proposed in this study is a two-step approach, based on both methods, previously used to quantify the vibrations: A particle based correction and a feature based correction. A schematic description of the approach is given in Figure 4.8. Before applying the vibration correction procedure, a self-calibration is performed. By calculating the disparity fields at every time instant, a mean disparity can be found, which is used to correct for major misalignments of the calibration target with the laser-sheet. The residual fluctuating disparity, which is left after this initial correction, will be corrected in two successive processing steps. In the first step of the correction approach, images from camera 1 and camera 2 are separated into two data sets. Applying Equation 4.2 to each separate data set, a feature-based shift detection is performed, which detects the shift of images with respect to the first image of the data set. The detected shifts will

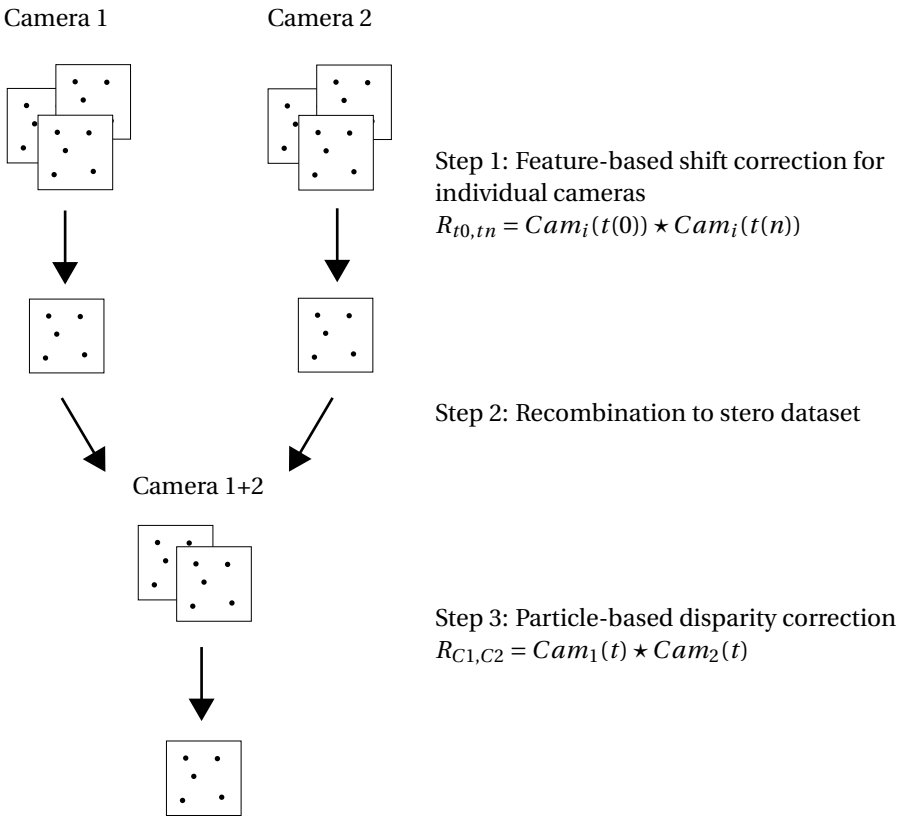

Figure 4.8: Schematic description of the vibration correction procedure

be used to perform a shift correction with respect to the master frame. Having performed a shift correction for both cameras independently, the image sets from both cameras will still have a constant offset when merged. This offset will be detected by applying Equation 4.1 to the merged data set and additionally correcting for the detected shift. The second step is equal to a second self-calibration, using the mean disparity vector field of all recordings. The result of the correction procedure can be seen in Figure 4.9 (left), showing a time trace of the disparity amplitude before and after applying the shift correction for a 3 m/s run. Statistical results for all tested velocities of 1, 3 and 5 m/s are shown in Figure 4.9 (right). While the disparity amplitude was increasing with the carriage speed before the correction procedure, the disparity could be significantly reduced. At 5 m/s, the mean disparity is approximately 1 pixel. While at 1 m/s, all image pairs have a remaining disparity smaller than 1 pixel, at 3 and 5 m/s 50 % of all image pairs have a disparity smaller than 1.2 pixels. A disparity of 3 pixels is only exceeded by single outliers. These image pairs will be deleted from the data set.

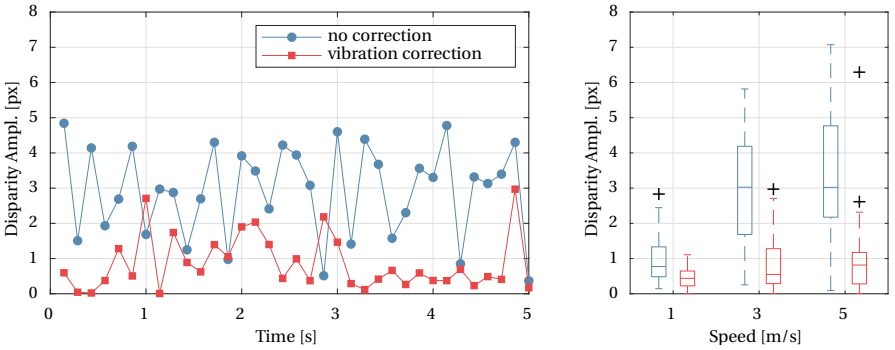

Figure 4.9: Disparity before and after vibration correction procedure

The herein proposed approach is similar to the method proposed by Novara et al. (2015). They corrected the camera vibrations by cross-correlating each image pair of two cameras and correcting the camera mapping function for each time instant. Subsequently, they used a flow-feature based method to correct the shift between different stereo PIV systems. To eliminate the time-varying shift of their velocity fields, they correlated the instantaneous velocity fields with a master velocity field. The resulting disparity vector was then used to correct the position. While initial disparities were of the order of 10 pixels, their corrected image pairs had a remaining disparity of 1.5 pixels.

4.3.2. VECTOR FIELD CALCULATION

Before finally calculating the velocity fields, a mask has to be applied to the recorded images, to mask out reflections on the acrylic glass plate and interceptor and to enhance correlation close to the ship hull and interceptor. As the ship has a simple geometry and the bottom of its aft section is visible in the images as a straight line, there was no need for automation of the masking procedure. For each interceptor height, a manual mask has been created, which was then applied to all images. The calculation of the velocity vector field is done in multiple correlation iterations. Starting with an interrogation window of 64 x 64 pixels in the initial pass, the window size is iteratively decreased to 24 x 24 pixels. The windows are overlapping by 50 %, and a Gaussian weighting function was used. Being ultimately interested in the mean value and other statistical properties of the flow, robust outlier detection is needed in-between passes, as already a small number of false vectors can significantly change the final result. For this reason, in-between passes, a 4-pass regional median filter is used to reject groups of spurious vectors. This type of robust outlier detection is well suited to remove most of the outliers, although with the drawback that some good vectors might be rejected, too. Figure 5.20 shows an example of the in-plane components from the mean velocity field, which was obtained from 200 vector

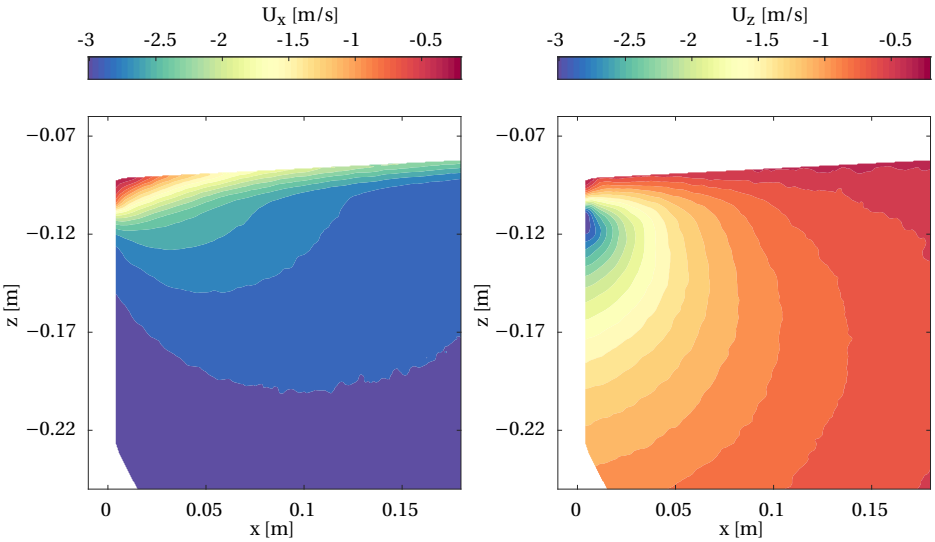

Figure 4.10: In plane velocity components of the time-averaged velocity field

images. As seen from the velocity fields, the stagnation region in front of the interceptor is well captured, as well as the downward acceleration towards the tip of the interceptor. The coordinate system is chosen to match the ship coordinate system with the origin located at the transom of the model at 0 degrees trim angle.

4.4. PRESSURE RECONSTRUCTION AND FORCE DETERMINATION

Having obtained the mean velocity field and its fluctuations from the statistical ensemble of the recorded velocity fields, one can describe the pressure gradient of the mean pressure field with Reynolds averaged momentum equation Equation 3.8. As already shown in Chapter 3, under the assumption, that the flow is incompressible, the viscous term disappears, and the pressure Poisson equation reduces to:

$$\frac{\partial^2 \overline{p}}{\partial x_i^2} = -\rho \frac{\partial}{\partial x_i} \left(\overline{u}_j \frac{\partial \overline{u}_i}{\partial x_j} + \frac{\partial \overline{u_i' u_j'}}{\partial x_j} \right) \tag{4.3}$$

The Reynolds stresses are found from variances and covariances of the velocity vectors. While in the symmetry plane of the ship model, the flow is assumed to be two dimensional, all spatial derivatives necessary for calculating the planar pressure field are obtained from a single-plane measurement. For a calculation of the three-dimensional pressure field in front of the interceptor, the spatial derivatives of the out-of-plane direction have to

be obtained from the measured fields of adjacent measurement planes obtained from multi-plane stereo PIV measurements along the transverse direction of the ship model.

As already mentioned in Chapter 3, the Poisson approach has been chosen over a direct integration to reconstruct the pressure field, as it is reported to produce less noisy results ((Albrecht et al., 2012)). To solve the Poisson equation, a Neumann boundary condition is obtained from the Reynolds-averaged momentum equation 3.8 to prescribe the non-homogeneous pressure gradient at the boundary of the measurement area:

$$n_i \cdot \frac{\partial \overline{p}}{\partial x_i} = -\rho n_i \cdot \left(\overline{u}_j \frac{\partial \overline{u}_i}{\partial x_j} - \nu \frac{\partial^2 \overline{u}_i}{\partial x_j \partial x_j} + \frac{\partial \overline{u_i' u_j'}}{\partial x_j} \right) \tag{4.4}$$

As only Neumann boundary conditions are used, a reference pressure is needed to scale the reconstructed pressures correctly. As no data from a reference pressure sensor is available, it is favorable to choose the reference pressure point to be in a region of undisturbed flow where it can be determined with the Bernoulli equation. However, due to the limited size of the measurement area, this was only possible for the smallest interceptor heights where the flow disturbance is small. To compare the reconstructed field with results from simulations, a reference pressure is taken from the numerical results 180 mm in front of the transom and 180 mm below the ship bottom, where the flow is disturbed the least. Figure 4.11 gives an example of the reconstructed pressure field in front of the interceptor and indicates the location P of the reference pressure point. The reconstructed pressure field, shows an increase of the pressure coefficient towards the transom, with a clear pressure peak right in front of the interceptor in the stagnation region. As the maximum blade stroke is smaller than the boundary layer height, and the flow is decelerated towards the wall in the boundary layer, the maximum pressure coefficient is well below 1.

The generated lift force from the interceptor will be obtained from numerically integrating the extrapolated pressure distribution over the length of the analyzed longitudinal segment of the model hull:

$$l = \int \bar{p} \vec{n} \cdot \vec{e}_z dS = \sum_{i=1}^{N} \bar{p}_i \cos(\theta) ds_i \tag{4.5}$$

Here, $\vec{n}$ is the surface normal vector and $\vec{e}_z$ describes the vertical unit vector normal to the freestream. θ is the trim angle of the ship model. With S being the length of the segment and V_c being the carriage velocity, the sectional lift coefficient per unit span is calculated as:

$$c_l = \frac{2l}{\rho V_c^2 S} \tag{4.6}$$

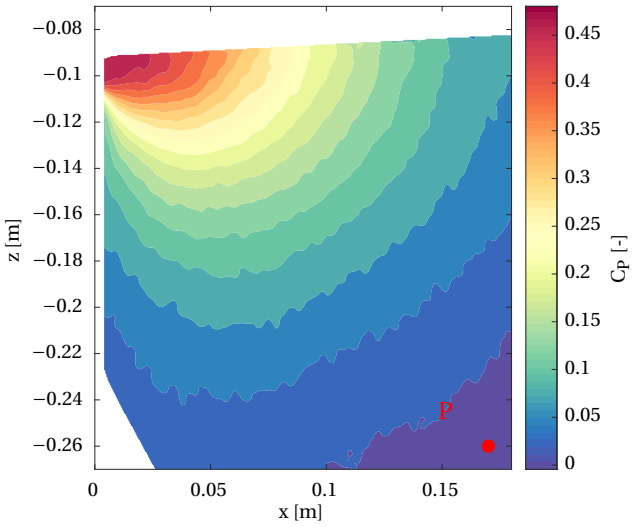

Figure 4.11: Reconstructed pressure field with reference pressure point P

4.5. MEASUREMENT UNCERTAINTY ASSESSMENT AND PROPAGATION

4.5.1. MEASUREMENT UNCERTAINTY

As multiple error sources influence the quality of PIV measurements, it is challenging to consider all of these for a reliable estimation of velocity field uncertainty. However, a number of a posteriori uncertainty estimation methods have been developed recently. Amongst these, the quantification of uncertainty based on the correlation statistics by Wieneke (2015) has shown to give a reliable estimate of the random uncertainty components. Looking only at the statistical quantities of the measured velocities, the uncertainty is, due to the finite sample size, typically dominated by random errors, and justifies a limitation to this component in the following analysis. Boomsma et al. (2016) have shown that these random errors are well predicted with the correlation statistics uncertainty quantification method.

To further assess the performance of the correlation statistics method to identify the random uncertainty components of the measured velocity field in towing tank applications, additionally, a series of uniform flow measurements were performed. Furthermore, these tests are performed to identify any bias introduced by the misalignment of the calibration plate. Since the laser is guided through the acrylic glass bottom of the model, the bottom has to be immersed in the water. To minimize the disturbance from the model

on the flow, it is trimmed to 0 degrees and its draft is changed to a minimum of 0.01 m. The temporal statistics of the freestream flow are subsequently analyzed at a single point with a distance of 0.1 m from the ship bottom for carriage speeds from 3 m/s to 5 m/s. In all analyzed cases, the laser pulse separation Δt was chosen to yield a pixel displacement of approximately 10 pixels for the freestream velocity. According to Sciacchitano and Wieneke (2016), the standard deviation of the measured velocities σ_u contains the true velocity fluctuations $\sigma_{u,fluct}$, as well as the measurement errors $\sigma_{u,err}$.

$$\sigma_u^2 = \sigma_{u,fluct}^2 + \sigma_{u,err}^2 \tag{4.7}$$

Assuming still water before every measurement run, in the case of no obstruction in the flow, the disturbance of the flow $\sigma_{u,fluct}$ is assumed to be negligible. Thus, any measured velocity fluctuations are due to errors in the measurement system and the vector calculation procedure. Provided, that the used uncertainty quantification is accurate (Sciacchitano and Wieneke (2016)), the error variance can be approximated with the mean square of the uncertainty of the instantaneous velocities $\overline{U_u^2}$ and Equation 4.7, can be simplified to

$$\sigma_u^2 = \sigma_{u,err}^2 \approx \overline{U_u^2} \tag{4.8}$$

Following from this, the performance of the uncertainty quantification method can be assessed by the comparison of the error standard deviation, and the root mean square (RMS) of the uncertainty. The error standard deviation σ_u is defined as

$$\sigma_u = \sqrt{\frac{\sum_{i=1}^{N}(u_i - \bar{u})^2}{N}}, \tag{4.9}$$

with u_i describing the instantaneous velocity and $\bar{u}$ the temporal average of the velocity. The RMS of the uncertainty $\sqrt{\overline{U_u^2}}$ can be found from the instantaneous uncertainties U_{u_i} and their temporal mean value $\overline{U}_u$:

$$\sqrt{\overline{U_u^2}} = \frac{\sum_{i=1}^{N}(U_{u_i} - \overline{U}_u)^2}{N} \tag{4.10}$$

Table 4.2 shows the uncertainty estimates and calculated errors for 3 m/s and 5 m/s freestream velocities. While the bias for the vertical velocity component is found to be negligible, the bias of the x and y velocity components indicate an initial rotation of the calibration target around the vertical axis of approximately 0.2°. For all velocity components, the RMS of the estimated uncertainty is slightly over predicted, compared to the standard deviation of the measured velocities. An explanation for this over-prediction may be found by looking at the uncertainty quantification procedure, where next to random errors, also small bias errors can be introduced for larger particle image sizes,

where the PIV algorithm does not converge to a fixed value Wieneke (2015). While in both cases the water was considered to be at rest, the increasing fluctuations at a higher carriage velocity may be due to an increase of the structural vibrations.

Vel. [m/s]	Comp.	Bias [px]	Error std. dev. [px]	Uncertainty RMS [px]
3	x	0.037	0.099	0.122
0	y	0.131	0.126	0.157
0	z	0.017	0.065	0.085
5	x	0.026	0.125	0.132
0	y	0.127	0.163	0.167
0	z	0.010	0.088	0.085

Table 4.2: Comparison of bias, errors, and uncertainties from freestream tests for the different velocity components

Having reported an estimation of the uncertainty in the undisturbed flow, it has to be noted that the uncertainty can vary significantly in space, depending on the local characteristics of the flow. In the present case, it is expected for the uncertainty to significantly increase in the boundary layer region due to the higher velocity gradient. As shown by Van Doorne et al. (2004) in areas with no velocity gradient, the registration error is zero, but increases in regions with high velocity gradients, due to the mismatch of the back-projected images. Especially at high speeds, this component is considered to be the largest uncertainty component due to the structural vibrations of the carriage. Furthermore, the correlation noise is expected to increase towards the ship hull due to the turbulent flow in the boundary layer. Figure 4.12 shows an example of the RMS of the velocity field uncertainty contours calculated from 200 images. The model speed is 3 m/s, and the interceptor height is 20 mm. A clear difference between the boundary layer region and the outer free-stream region can be seen. While values in the outer region comply with the initial freestream reference runs, the uncertainty increases towards the boundary layer. The highest values are found in the stagnation region close to the interceptor with uncertainties up to 3 % of the freestream velocity component.

4.5.2. UNCERTAINTY PROPAGATION

As the main uncertainty components are random, their magnitude scales with the number of samples N when calculating the uncertainty of the time-averaged velocity field components. Following Sciacchitano and Wieneke (2016) the uncertainty of the mean velocity $U_{\bar{u}}$ can be calculated as:

$$U_{\bar{u}} = \frac{\sigma_u}{\sqrt{N}} \tag{4.11}$$

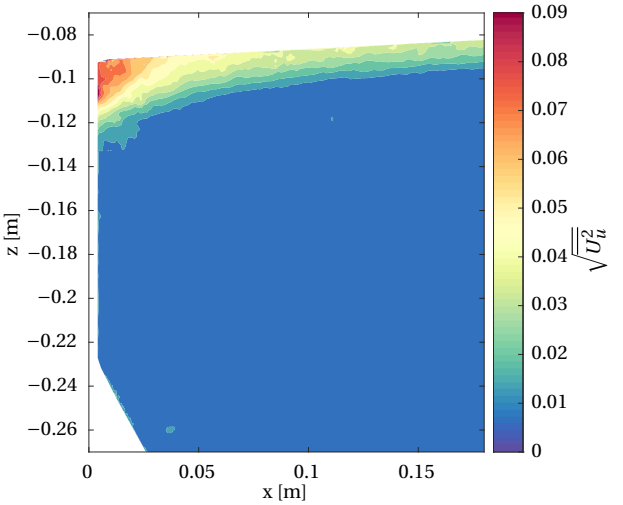

Figure 4.12: Spatial variation of the RMS of the velocity field uncertainty at $V_c =$ 3m/s with interceptor height h = 20 mm

Here, the velocity standard deviation σ_u contains the true velocity fluctuations, as well as the measurement errors. Using the derived formulas from Sciacchitano and Wieneke (2016) also the uncertainty of the Reynolds stresses can be determined. As the uncertainties of the mean velocity field are small compared to the velocity fluctuations, the uncertainty of the normal stresses equals the uncertainty of the variance:

$$U_{R_{uu}} = \sigma_u^2 \cdot \sqrt{2/(N-1)} \tag{4.12}$$

However, having quantified the uncertainties of the instantaneous velocities, the Reynolds stresses can be corrected by the subtraction of these.

$$R_{uu,corr} = R_{uu} - \overline{U_u^2} \tag{4.13}$$

As derived by Sciacchitano et al. (2015), this enables a corrected, more accurate uncertainty propagation, leading to:

$$U_{Ruu,corr} = \sqrt{Ruu^2} + \left(\sqrt{2}\sigma_{U_u} \overline{U_u} \sqrt{1 + \frac{\sigma_{U_u}^2}{2\overline{U_u}^2}} \right) \sqrt{\frac{2}{N}} \tag{4.14}$$

with σ_{U_u} being the standard deviation of the uncertainty. The uncertainty of the Reynolds shear stress can be calculated with the covariance uncertainty equation, which, under

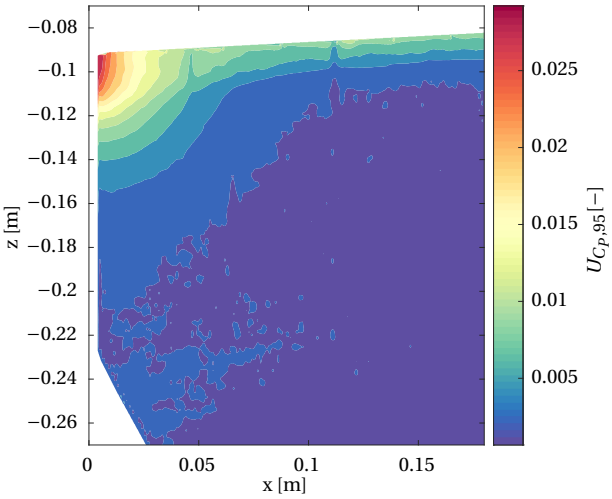

Figure 4.13: Pressure uncertainty map from propagated uncertainties at 95 % confidence level at V_c = 3m/s with interceptor height h = 20 mm

the assumption of a zero correlation coefficient, is:

$$U_{R_{uv}} = \sigma_u \sigma_v / \sqrt{N-1} \tag{4.15}$$

For further propagation of the assessed uncertainty components of the mean velocity and Reynolds stresses towards the time-averaged pressure field $\bar{p}$, it is chosen for a Monte Carlo approach, according to ISO (2009). Compared to the linear uncertainty propagation, described according to ISO (2008), this method gives a generally improved estimate of the output quantity $\bar{p}$. As found by Azijli et al. (2016), a linear uncertainty propagation of the measured components towards the pressure field leads to an underestimation of pressure uncertainty by about 30 % compared to results from Monte Carlo simulations. Under the assumption of the measured input variables to be Gaussian distributed, simulations with 10.000 realizations are done to evaluate the uncertainty of the reconstructed pressure field. The Monte Carlo simulations were performed within the OpenFOAM package, using the `GaussNormal` member function of the `Random` class to generate variations of the input variables. The final expanded uncertainty $U_{\bar{p},95}$ is then calculated by multiplying the resulting standard uncertainty with a coverage factor of 2 for a confidence interval of 95 %. As seen in Figure 4.13 the expanded uncertainty in the freestream region is below 0.5 % of the maximum pressure and increases towards the boundary layer. Starting from approximately x/h=1 the uncertainty increases significantly to up to 6.5 % of the peak pressure right in front of the interceptor. Knowing the discrete uncertainty distribution of

the pressure field on the ship hull, the uncertainty of the sectional lift can be estimated as:

$$U_l = \sqrt{\sum_{i=1}^{N} U_{\bar{p}_i}^2 \, ds_i^2} \tag{4.16}$$

4.6. NUMERICAL SIMULATIONS

For a comparison of the obtained PIV results with numerical results, CFD simulations of the performed towing tank tests are made with the open-source code OpenFOAM 5.0. The incompressible unsteady Reynolds-Averaged Navier-Stokes equations are solved with the interFoam solver, where the Volume of Fluid (VOF) approach is applied to capture the two-phase interface. The governing equations are discretized with second-order central-differencing schemes, and a two-equation k-omega-SST model is used for modeling the turbulence. As the ship model is symmetric, only one half of the ship is meshed to reduce the number of cells. The numerical grid is generated with the hexahedral mesher snappyHexMesh, which is modified to fit the needs for the meshing of marine applications and allows for higher aspect ratio cells in the free-surface region. After calculating an initial solution with a coarse grid, the grid is further refined in the free-surface region and in front of the interceptor. An example of the final mesh in the free-surface region is depicted in Figure 4.14, including the dimensions of the domain. While the cross-section of the domain was chosen to fit the TU Delft towing tank dimensions, the outlet position of the domain was chosen according to the ITTC guidelines (ITTC (2011)) to prevent wave reflection. Also depicted in Figure 4.14 is the refined region in front of the interceptor with the prismatic boundary layers inserted on the ship hull. To guarantee similarity of meshes with different interceptor heights, one mesh is generated for each speed. The interceptor is modeled with baffle cells to keep mesh deformations close to the interceptor as small as possible.

To find the optimal mesh size and prove the grid independence of the final solution, a grid convergence study is conducted with a total of three meshes, varying the cell count from 593,984 up to 2,120,864 cells. For the finest mesh, the target cell size of the smallest cells outside the boundary layer is specified as $Lpp/710$, with Lpp being the length between perpendiculars at floating position. Choosing a grid refinement ratio of $r = \sqrt{2}$, the coarser meshes are generated, resulting in an edge length of $Lpp/353$ of the smallest cell outside the boundary layer for the coarsest mesh. The boundary layer is designed for all meshes to yield a dimensionless wall distance y^+ of 30 for the cell closest to the wall, which enables the correct application of wall functions for modeling of the flow in the near-wall region. The growth ratio for the boundary layer cells is chosen as 1.2. While usually the resistance is used to observe the grid independence, in this case, the hydrodynamic lift L in the aft section from x=0 to x=800 mm was found to be more

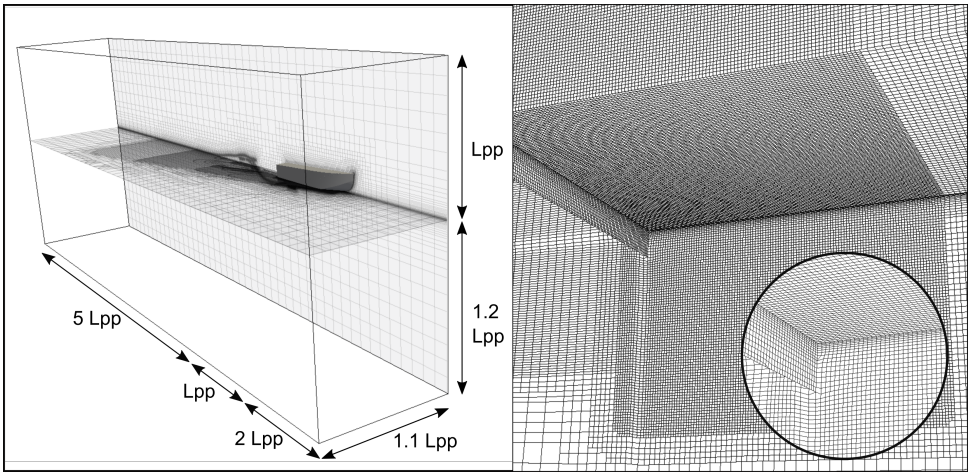

Figure 4.14: Computational domain with main dimensions (left); Refined mesh in front of the interceptor with detail view of the boundary layer mesh (right)

meaningful to evaluate the influence of the grid on the flow around the interceptor. The result of the grid refinement study is shown in Figure 4.15, where the hydrodynamic lift for all three meshes is plotted over their normalized grid spacing. The ship speed selected for the refinement study is 4 m/s, and the average y^+ value is within the range between 28 and 40 for all meshes. While the red dots indicate the total resistance from the CFD simulations, the green square shows the Richardson extrapolate, which gives an estimate of the lift force at zero grid spacing. While the grid refinement ratio is constant, the order of convergence was determined with the solutions from the three grids:

$$p = \frac{L(1) - L(\sqrt{2})}{L(\sqrt{2}) - L(2)} / ln(r) \tag{4.17}$$

The determined order of convergence for these grids is 1.44. This value is used for the calculation of the extrapolated solution at zero grid spacing which is:

$$Pr_{h=0} = L(1) + (L(1) - L(\sqrt{2}))/(2^p - 1) \tag{4.18}$$

To give a measure of the percentage, the computed value is away from the asymptotic value, Roache (1998) proposed the grid convergence index (GCI).

$$GCI = \frac{F_s|\epsilon|}{r^p - 1} \tag{4.19}$$

with ϵ being the relative error between the two finest grids and F_s being a factor of safety, which is 1.25. For the two finest grids, the GCI is obtained to be 3.8%. For further analysis

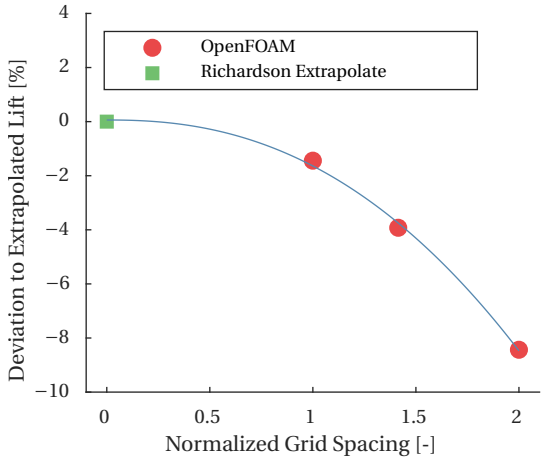

Figure 4.15: Grid convergence study: Deviation of hydrodynamic lift forces on the aft section of the ship model to extrapolated value at zero grid spacing

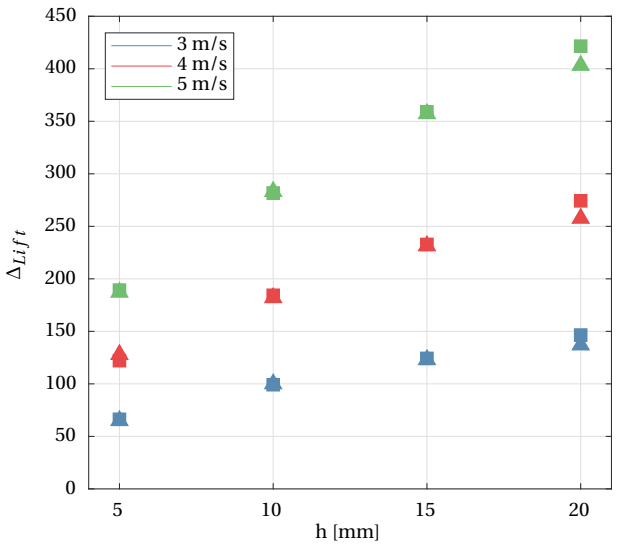

Figure 4.16: Comparison of lift forces from numerical simulations (■) and segmented model tests (▲) acting on the aft model section

of the accuracy of the simulations, the lift, generated by the interceptor in the aft section of the model, is compared the results of segmented model tests performed by Rijkens et al. (2013). Figure 4.16 shows the comparison of the generated lift force on the aft segment of the ship hull for different speeds and interceptor intrusion heights. The lift force generated by the hull without interceptor is subtracted from the results. The numerical results are found to be in good agreement with the experimental results. Especially for interceptor heights up to 15 mm the comparison error is below 2 %. Interestingly at interceptor heights of 20 mm the CFD results systematically under predict the measured lift force. The maximum comparison error here is approximately 6 %.

4.7. DISCUSSION AND COMPARISON OF EXPERIMENTAL AND NUMERICAL RESULTS

4.7.1. 2D RESULTS

The flow field in front of the interceptor is recorded in the center plane of the ship model while systematically varying of intruder height and ship speed. While the ship hull is considered to be symmetrical, the flow in the center plane can be considered to be two dimensional with no out-of-plane velocity. As shown by Brizzolara (2003), already small changes in the boundary layer shape can significantly change the pressure distribution in front of the interceptor. Following from this, it has to be checked carefully if the simulated flow field close to the ship hull is in good agreement with the experimental conditions before comparing simulated and reconstructed pressure fields. Figure 4.17 gives an insight into the flow in front of the interceptor close to the ship hull. The mean velocity and pressure profiles in the center plane of the model are plotted for different stations in front of the transom. Results are presented for an interceptor intrusion height of 20 mm. Measured velocities and reconstructed pressures are compared to results from the performed CFD calculations to judge the quality of the near-wall resolution. The velocity magnitude is made dimensionless with the free-stream velocity. Wall distance and longitudinal distance from the transom are expressed relative to the interceptor height h. Affected by the adverse pressure gradient, which is generated by the interceptor, the flow in the boundary layer is decelerated towards the transom. Measured and simulated velocity and pressure profiles are in good agreement with each other. As expected, the good agreement of the velocity field in the boundary layer also leads to a good agreement of the reconstructed and simulated pressures.

Contour plots of the reconstructed pressure field in front of the interceptor in the center plane of the model are depicted in Figure 4.18 (left), where they are compared to the simulation results (right). Pressure fields are shown for 5, 10, and 20 mm interceptor intrusion heights at a speed of 3 m/s. Both the reconstructed pressure fields and

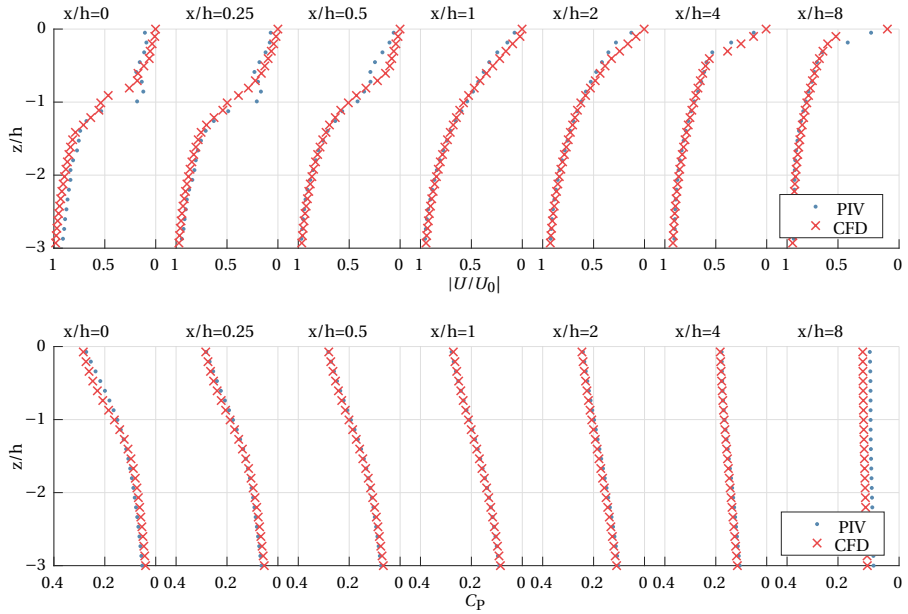

Figure 4.17: Velocity profiles normal to the ship hull at different stations in front of the interceptor (top); Corresponding pressure profiles normal to the ship hull at different stations in front of the interceptor (bottom)

simulations predict the influence of the interceptor on the pressure peak in front of the interceptor well, and results are in good agreement with each other. With increasing the interceptor intrusion height, not only the peak pressure in front of the interceptor increases but also the length of the high pressure region. Largest differences can be found close to the interceptor in the stagnation region, where both reconstructed results give a higher maximum pressure compared to the simulations.

To further analyze the dependency of the pressure distribution on the ship hull on interceptor height, the pressure field is interpolated to the ship hull. Figure 4.19 shows the pressure distribution on the ship hull for interceptor heights increasing from 0 to 20 mm in steps of 5 mm at constant model speed. While the lines represent the CFD results, the dots represent the reconstructed pressures. As the original resolution of the PIV vector grid resulted in a total of approximately 135 measurement points over the length of the measurement section on the ship hull, for the sake of clarity, only every fourth measurement point is plotted. In all conditions, the flow is smoothly separating from the transom, leaving the transom dry. Resulting from this, without any interceptor, the pressure drops to atmospheric pressure towards the transom due to the presence of the free-surface, leading to a negative dynamic pressure at the transom. Due to the stagnation region in front of the interceptor, this pressure becomes positive and is increas-

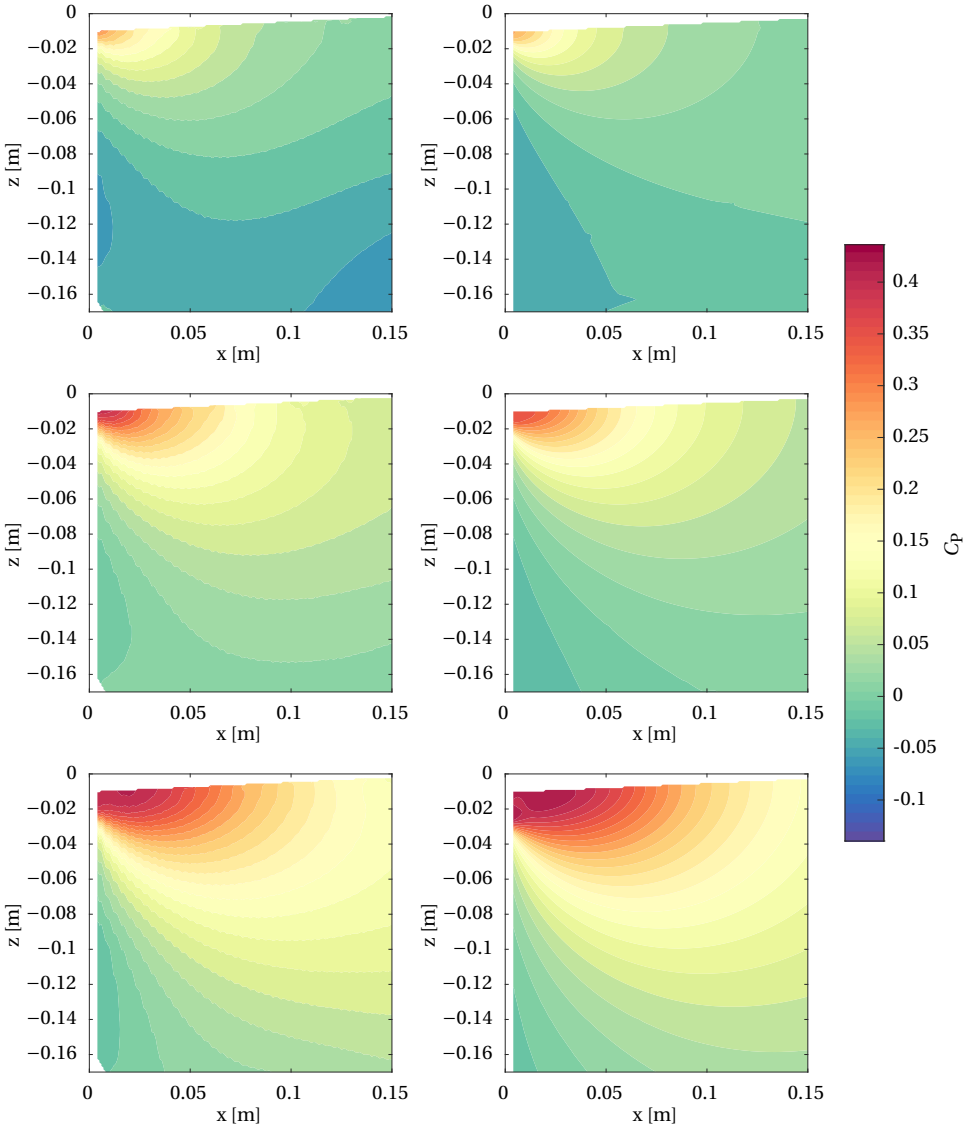

Figure 4.18: Comparison of reconstructed pressure contours (left) and numerical results obtained with OpenFOAM (right) for interceptor heights of 5,10 and 20 mm (top to bottom) at 3m/s

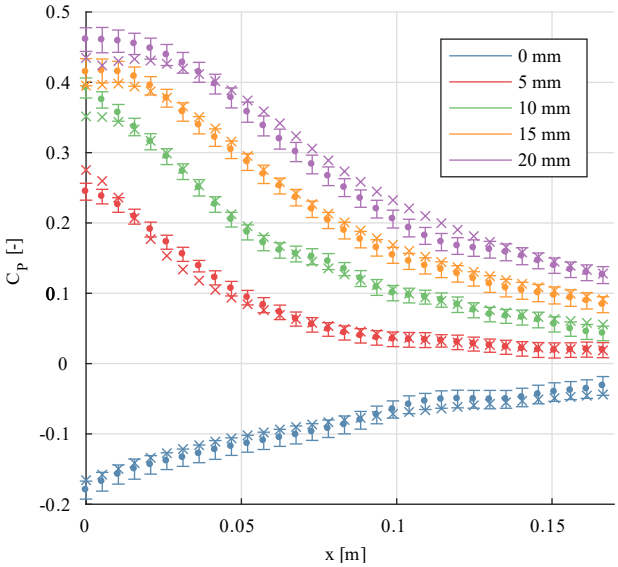

Figure 4.19: Influence of the interceptor height on the pressure distribution on the ship hull in the center plane of the model – comparison of reconstructed pressures (•), including their extended uncertainty bounds, with results from numerical simulations (×)

ing with interceptor height. It is interesting to see that already the smallest interceptor intrusion height creates a significant change in the pressure distribution at the transom. Also, the point of separation shifts further forward, resulting in an increasing region of constant pressure right in front of the interceptor. Both results from measurements and simulation are in good agreement with each other, with the largest differences in the region of the pressure peak. However, the difference of the peak pressures still lies within the uncertainty band of the PIV results, which was estimated to be approximately 6 % of the peak pressure value in this region. The reconstructed 2d pressure fields in the center plane of the ship hull were integrated to yield the total dynamic lift force component in the aft region of the ship, disregarding any 3d effects. Figure 4.20 shows the lift force for all analyzed speeds and interceptor heights per unit ship width and compares experimental results and their calculated uncertainty with results from CFD simulations. The uncertainties of the integral forces were found from integrating the uncertainties of the single measurement points. While for 3 m/s experimental results are in good agreement with simulations, the integrated values at 4 and 5 m/s are slightly overpredicted for most analyzed conditions with maximum differences of approximately 8 percent. As the laser pulse separation has been initially chosen to yield a constant pixel displacement in the freestream for all tested velocities, the actual uncertainty values increase proportionally with carriage velocity. This trend is also propagated to the integral forces.

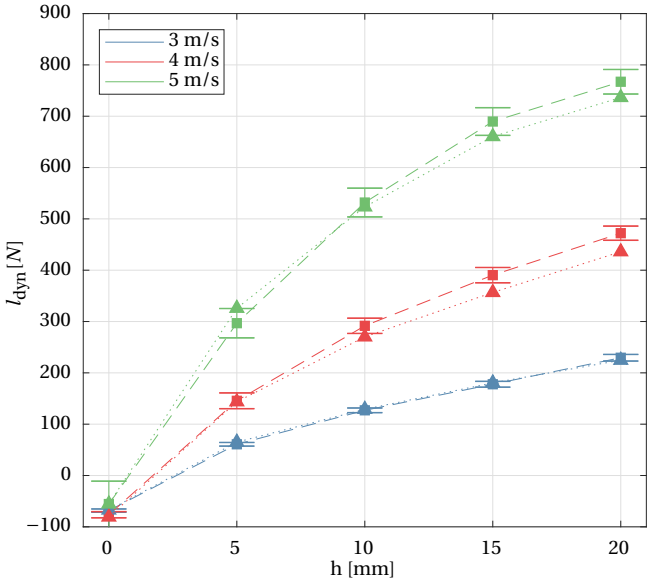

Figure 4.20: 2d lift force dependence on interceptor height (h) and model speed – comparison of reconstructed lift force (■), including extended uncertainty bounds, with results from numerical simulations (▲)

4.7.2. 3D RESULTS

For selected conditions at 3 and 4 m/s the measurement planes were shifted stepwise towards the side of the model to reconstruct a volumetric velocity field from a total of 14 measurement planes and analyze the three-dimensionality of the flow around the interceptor. Figure 4.21 shows contour plots of the three velocity components and reconstructed pressures at 3 transverse positions from a selected run with an interceptor height of 20 mm at a speed of 3 m/s. At y=0 m, in the center plane of the ship model, the mean flow is purely two-dimensional. While the out-of-plane component is close to zero in the whole field of view, the in-plane components show a deceleration of the flow towards the interceptor in x-direction and an acceleration in z-direction. As seen from the contour plots at y=0.1 m and 0.18 m, the out-of-plane component steadily increases towards the side of the model, while the downward component decreases. With the increasing out-of-plane component towards the side of the interceptor blade, the high pressure region in front of the interceptor significantly reduces in size.

The reconstructed volumetric pressure field has been extrapolated to the ship hull to analyze the three-dimensional effects of the flow on the surface pressure distribution. Results presented in Figure 4.22 and 4.23 (top) show the reconstructed pressure coefficient on the ship hull for interceptor heights of 10 and 20 mm at 3 and 4 m/s model speed

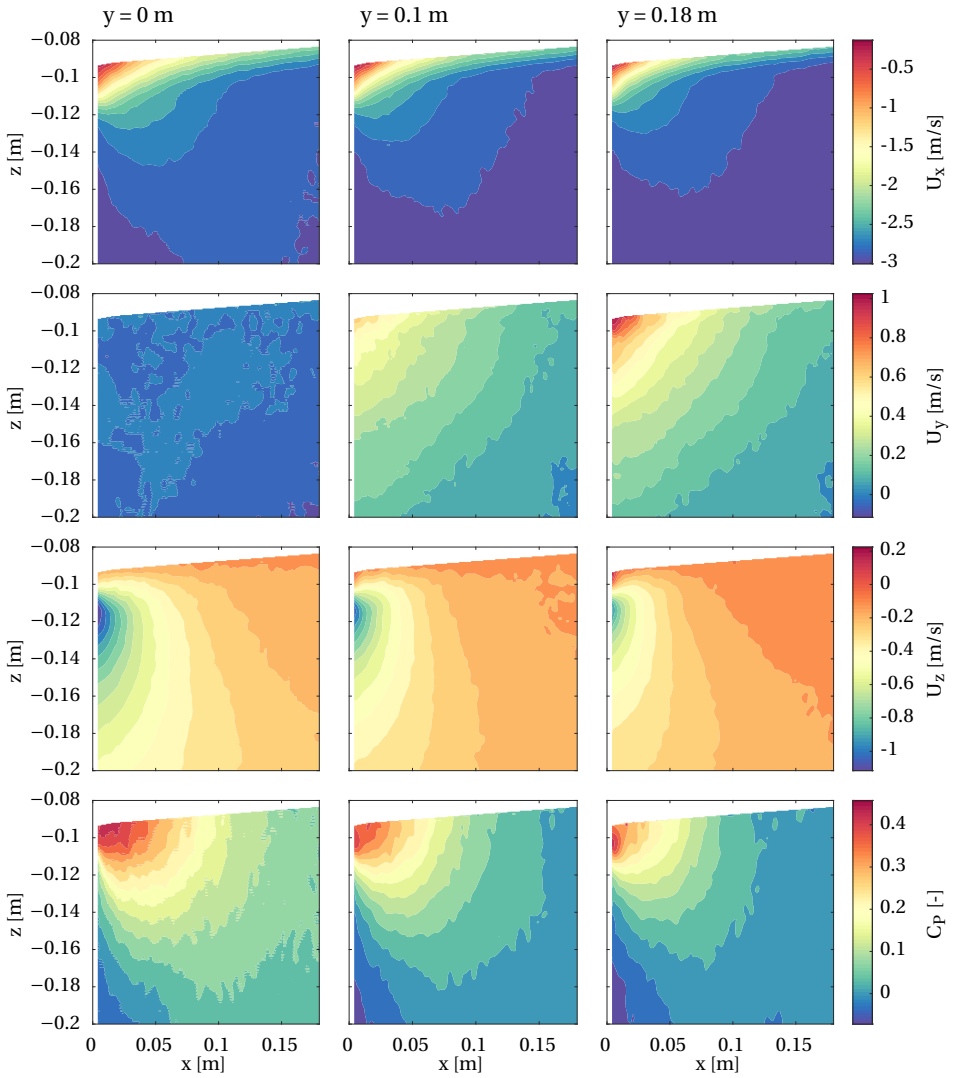

Figure 4.21: Velocity components at different transverse positions with reconstructed pressure fields at 3 m/s with h=20 mm

on an area of 180 x 190 mm^2. For comparison in Figure 4.22 and 4.23 (bottom) pressure distributions which were obtained from CFD simulations are presented. As already seen in Figure 4.21, due to the increased transverse flow component in front of the interceptor, the pressure reduces towards the side of the interceptor blade. While there is a good agreement between results from CFD and PIV measurements in the far-field, larger deviations can be found in the peak pressure region, especially at interceptor heights of 20 mm. As already seen from the two-dimensional results, the reconstructed peak pressure from the PIV measurements is slightly higher compared to the CFD results.

The integration of the surface pressure along the ship's longitudinal direction at different transverse sections quantifies the hydrodynamic lift reduction towards the side of the interceptor due to the three-dimensionality of the flow. Figure 4.24 shows the sectional lift coefficient and its uncertainty, calculated according to Equation 4.16, from all 14 measurement planes and compares them to the numerical results. Results from experiments and simulations both clearly show a reduction of lift towards the side of the interceptor and are in good agreement with each other for all analyzed velocities and interceptor heights. Due to the overprediction of the pressure peak in the center planes of the ship, here, the total dynamic lift is also overpredicted by the pressure reconstruction from PIV results. However, an integration of the sectional loads over the width of the ship leads to maximum differences of approximately 3 % of the hydrodynamic lift between experimental and numerical results. General conclusions about the lift reduction due to three-dimensional effects and its dependency on interceptor height and speed cannot be drawn from these results, as the measurement area is too small, not fully covering the whole region where the pressure distribution is modified due to the influence of the interceptor. While the aft-segment of the segmented model, used by Rijkens et al. (2013) had a length of 400 mm, the obtained lift forces of both experiments are also not comparable. Further, no volumetric field is reconstructed for runs without an interceptor, which would allow for isolation of the pressure increase due to the interceptor.

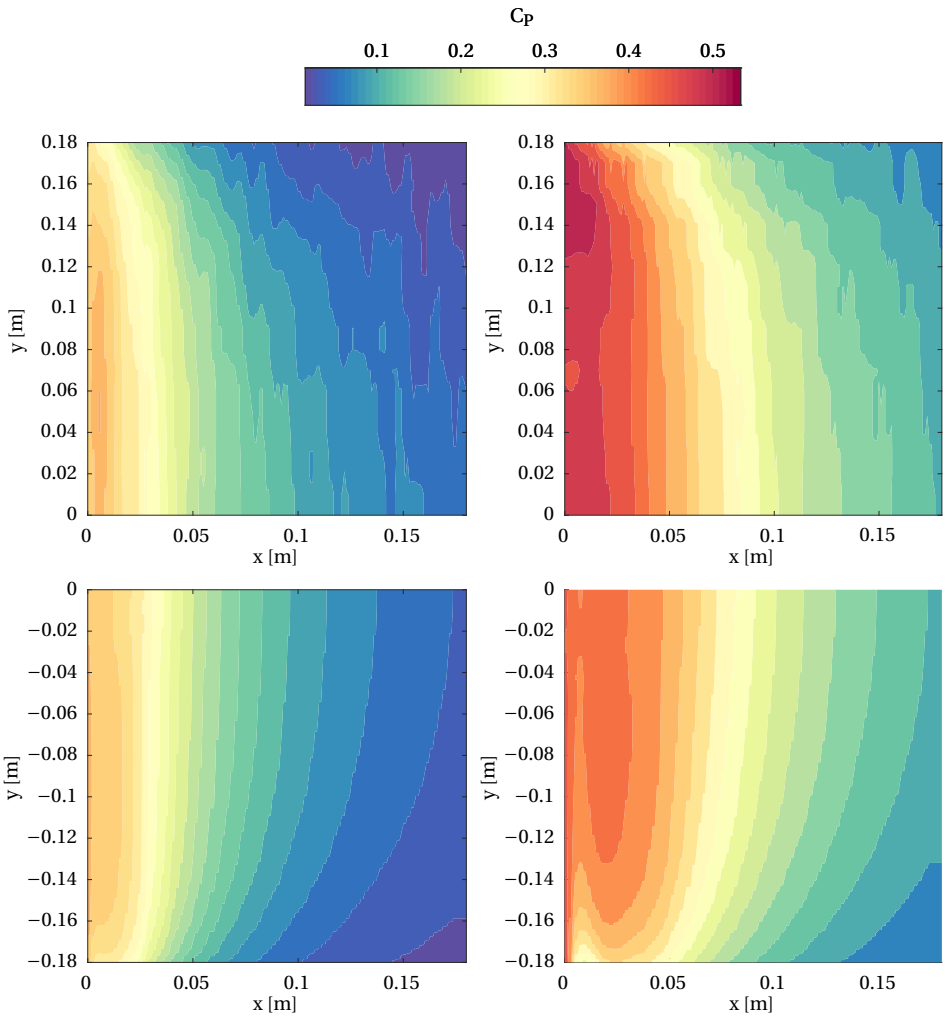

Figure 4.22: Comparision of reconstructed pressure fields on the ship model (top) with results from CFD simulations (bottom) at 3 m/s and interceptor heights of 10 mm (left) and 20 mm (right)

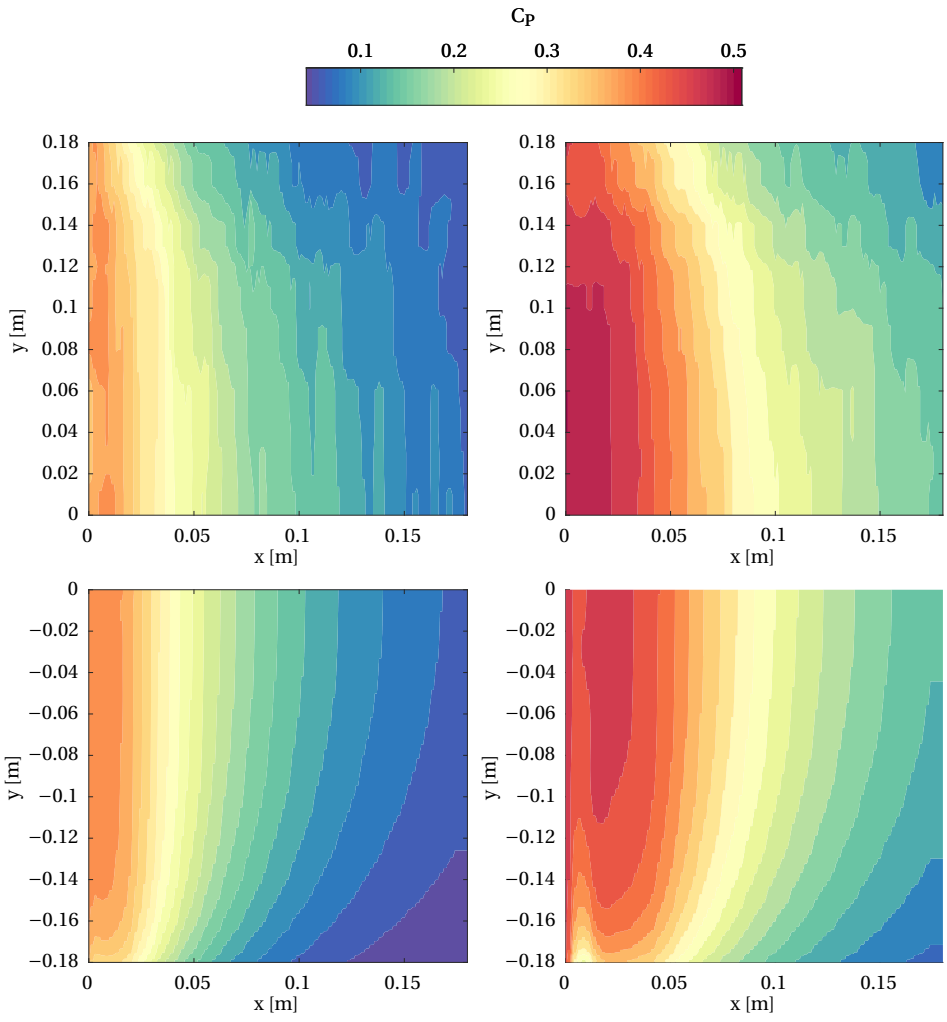

Figure 4.23: Comparision of reconstructed pressure fields on the ship model (top) with results from CFD simulations (bottom) at 3 m/s and interceptor heights of 10 mm (left) and 20 mm (right)

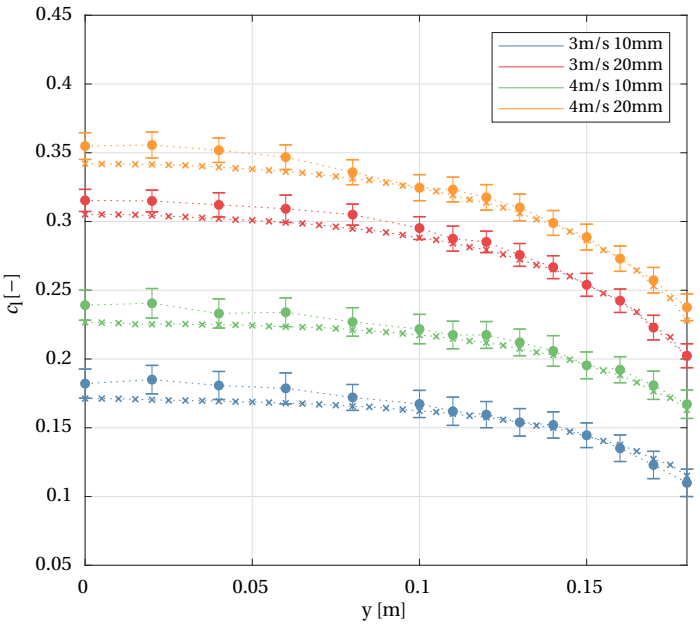

Figure 4.24: Lift coefficients for varying speeds and interceptor heights at different transverse sections – comparison of reconstructed lift force (•), including extended uncertainty bounds, with results from numerical simulations (×)

4.8. DISCUSSION

In the present chapter, the influence of high towing tank carriage speeds on the performance of an underwater stereo-PIV is evaluated. Having found large disparities between both cameras due to structural vibrations, a method is presented to correct for these and reduce the disparities to an acceptable level. To study the characteristics of the flow around an interceptor, the underwater stereo-PIV system is utilized to obtain the time-averaged velocity field close to the transom of a ship model that is equipped with an interceptor, which can be adjusted in height. The obtained results are eventually used together with the Poisson pressure equation to reconstruct the average pressure field in the flow field as well as on the ship model. While a broader range of conditions is analyzed with single plane PIV measurements in the center plane of the model, for selected conditions also a volumetric flow field, spanning the whole width of the transom, is reconstructed from multi-plane stereo PIV measurements. When comparing experimental results with those from simulations, often the question arises if the experimental conditions have been accurately modeled in the numerical simulations. Especially in the case of the flow in front of an interceptor, the pressure distribution is very sensitive to differences in boundary layer characteristics (Brizzolara (2003)). By comparing the measured velocity field in front of the interceptor with results from simulations, it is made sure that the experimental conditions are accurately reproduced within the numerical simulations. The following analysis of the dynamic pressure fields for a range of interceptor heights and model speeds shows that the pressure distribution in the flow field, as well as the extrapolated pressures on the ship hull, are in good agreement with each other. With performing multi-plane stereo PIV measurements, an alternative technique is proposed to measure the average dynamic pressure distribution on a whole segment of a ship model. In case of the present study, the 3d effects of an interceptor with a finite span on the pressure distribution on the ship hull are successfully captured. However, for a systematic study of the effect of the three-dimensionality of the flow, more configurations have to be analyzed.

To judge the accuracy of the reconstructed pressures, the random uncertainty component of the recorded velocity field has been quantified and was propagated towards the pressure field with Monte Carlo simulations. The resulting uncertainty maps of velocity and pressure fields showed large local variations with a steep increase of uncertainty values in the boundary layer of the ship model, emphasizing the necessity for a consideration of the spatial uncertainty distribution and not only rely on freestream measurements. However, the combination with freestream measurements is advised as a good measure to identify and correct for any systematic errors, such as calibration target misalignment.

5

VELOCITY AND PRESSURE MEASUREMENTS IN THE BOW REGION OF A FAST SHIP

Results from the previous chapter have shown that the pressure PIV technique can be applied for the reconstruction of hydrodynamic pressures in the flow field around a fast ship. It was focused on testing the overall feasibility of the method at high towing tank carriage velocities and assessing the occurrence of vibrations. For this purpose, the model of a generic planing hull was chosen, with no geometrical variations in between different measurement planes. However, ships mostly have complex hull geometries. As has been outlined in Chapter 2, masks have to be applied to recorded images to improve correlation close to features such as the ship hull or the water surface. An appropriate mask, which is based on the recognition of features in the images, is also key for a correct application of boundary conditions for the solution of the pressure Poisson equation. Especially when the position of objects and interfaces changes in-between measurements, may it be due to the change of the measurement position or the transient manner of the flow problem, an automated procedure is necessary. Furthermore, during the measurements, presented in Chapter 4, the measurement plane was aligned with the main flow direction, resulting in comparatively large in-plane velocity components. While this is considered to be ideal, in towing tank applications, the measurement plane often has to be perpendicular to the flow to capture the main features of specific flow structures, such as vortices. It has been

Parts of this chapter have been published in Int. Conference on Advanced Model Measurement Technology for The Maritime Industry, Jacobi et al. (2019a).

shown in Chapter 2, that the out-of-plane component can have a significant influence on the correlation peak quality. A perpendicular alignment of the measurement plane with the main flow direction is considered to become even more critical when in-plane velocity components are small compared to the out-of-plane components, which for towed PIV systems are mostly dominated by the carriage speed. Especially at high carriage velocities, an orientation of the measurement plane perpendicular to the main flow direction is thus considered as critical. Both of the previously addressed topics are discussed in the following chapter with the aid of a practical application. PIV measurements of the flow in the bow region of a fast-displacement vessel and subsequently a reconstruction of the pressure field from these are presented for a steady captive model, as well as for a model that performs forced heave oscillations. In case of the steady model, the time-averaged flow is measured in a total of 60 measurement planes to reconstruct the three-dimensional flow field in the bow region and finally derive the hydrodynamic pressure distribution on the hull. During forced oscillation tests, the flow field is recorded in three successive planes, to obtain a local phase-averaged description of the velocity and hydrodynamic pressure field. Results from PIV measurements are compared to numerical results from RANS and unsteady RANS simulations.

5.1. TEST CASE

As already outlined in Chapter 1, the bow shape of a high-speed craft can significantly influence its hydrodynamic behavior. The work of Keuning (1994) extensively analyzed the influence of the bow shape of high-speed monohulls, with focussing on its influence of the seakeeping behavior. As a result of the numerical as well as experimental assessment, there was the development of two innovative concepts: the enlarged-ship concept (Keuning and Pinkster (1995)) and the axe-bow concept (Keuning et al. (2001)). The idea behind the enlarge ship concept was to increase the vessels length up to 50%, while displacement and other dimensions remained unchanged. As a result, the length to beam as well as length to displacement ratio was increased. This design allowed for much larger deadrise angles in the bow region, which significantly reduced wave exciting forces and hydrodynamic lift in this region. As shown by Keuning (2006), who extensively assessed the calm water performance and behavior in irregular seas during towing tank tests, this resulted in an improved and more linear motion response, compared to existing vessels. The linesplan of the tested conceptual design is depicted in Figure 5.1. The ship was designed as a prototype for the U.S. Coast Guard who dictated a waterline length of 55 m and a maximum target speed of 50 knots.

The same vessel has been later used by De Jong (2011), to validate the seakeeping code Panship, which is based on a non-linear time-domain simulation approach. For this purpose, additional experiments were conducted in regular waves, as results from

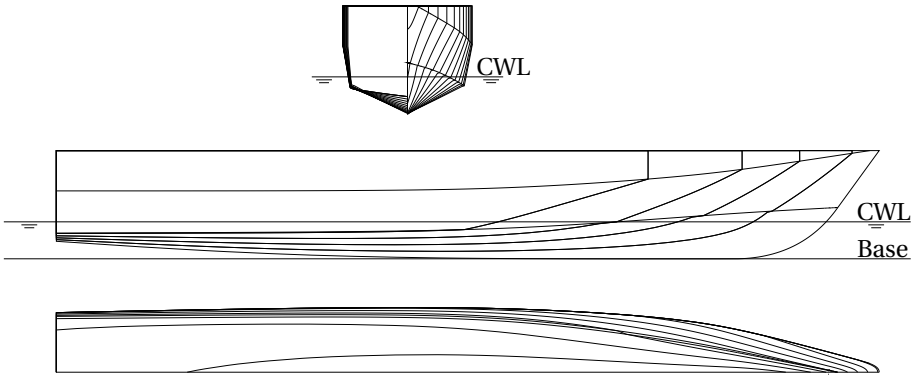

Figure 5.1: Lines plan Enlarged Ship Concept

these were more suited for comparison with numerical results. Comparing the calm water running trim and sinkage of experiments with numerical results, it was concluded, that the trend of both parameters was reasonably predicted, but still, significant differences in the absolute values existed. As both trim and sinkage significantly influence the hydrodynamic behavior of a ship sailing in waves, these results were not satisfying, and it was advised that further analysis is necessary to understand the underlying physics that cause these differences. The overall comparison of regular and irregular wave computations with conducted experiments gave good agreement. However, more significant differences were found in pitch motion, and the numerical model did not predict vertical acceleration peaks. While the validation of the numerical code was only based on the comparison of global motions, loads, and acceleration levels, it was concluded that an experimental assessment of the detailed pressure distribution on the ship hull would enable a better understanding of the obtained differences. Instead of only comparing experiments and numerical simulations, a better understanding of the underlying physical effects is needed.

Motivated by the findings and recommendations of De Jong (2011), PIV measurements are conducted in the bow region of the previously described enlarged ship concept vessel, to capture the local flow and reconstruct the hydrodynamic pressure field in this region. The aim is to capture the pressure distribution during towing tank tests with a captive model in calm water, as well as during forced heave oscillation tests. Experimental tests are conducted with a scaled version of the previously described model at a scale of 1:30. The model scale particulars and their full-scale equivalents are shown in Table 5.1.

Quantity	Symbol	Full scale	Model scale	Unit
Length between perpendiculars	L_{pp}	22	1.83	m
Beam on waterline	B_{WL}	3.38	0.28	m
Draft	T	1.06	0.09	m
Volume of displacement	∇	33	0.02	m^3
Wetted area	S_W	76.89	0.53	m^2
Vertical position CoG	KG	1.54	0.13	m
Longitudinal position CoG	LCG	9	0.75	m
Pitch radius of gyration	k_{yy}	5.5	0.46	m

Table 5.1: full-scale and model-scale main particulars of the ESC

5.1.1. CALM WATER

Before one turns towards looking at the behavior of a moving ship, it has to be made sure that the calm water behavior of a ship is correctly modeled. This is especially important for fast ships, as their calm water behavior strongly influences their seakeeping behavior, with the high forward speed resulting in significant changes of trim and sinkage and thus influence the submerged geometry of the vessel. Results from calm water tests, which were conducted by Keuning and Van Walree (2006) are presented in Figure 5.2, showing the dependency of trim, sinkage, and resistance on the forward speed. As seen from the dependency of the sinkage of the vessel on forward speed, the vessel starts to generate a positive hydrodynamic lift at Fr_L 0.5, resulting in a significant change of the vertical position in the water. Based on the results of these tests, a model speed of Fr_L 0.8 is selected for an in-detail investigation with the pressure PIV technique. The selected speed is equal to 37 kn in full-scale and 3.32 m/s in the selected model scale. While keeping the model captive, at the determined trim and sinkage, multi-plane PIV measurements are conducted to record the flow field in the bow region of the model over a length of 0.6 m, starting 1.2 m in front of the transom. With a spacing of the measurement planes of 0.01 m, the time-averaged flow field is obtained in a total of 60 measurement planes, to finally reconstruct a volumetric description of the flow field in this area. A schematic drawing with the position and orientation of the measurement planes is shown in Figure 5.3. Using this velocity field, finally, the hydrodynamic pressure distribution in the flow field and on the ship hull is calculated by applying the Poisson equation.

5.1.2. FORCED HEAVE OSCILLATIONS

To assess the performance of a seakeeping code, De Jong (2011) conducted tests with the model sailing in regular waves. This was considered more suitable for the direct comparison of the time traces of both simulation and measurement results. While this made differences more clear than a simple statistical comparison of results, the reasons for any differences between simulation results and experiments were still not known,

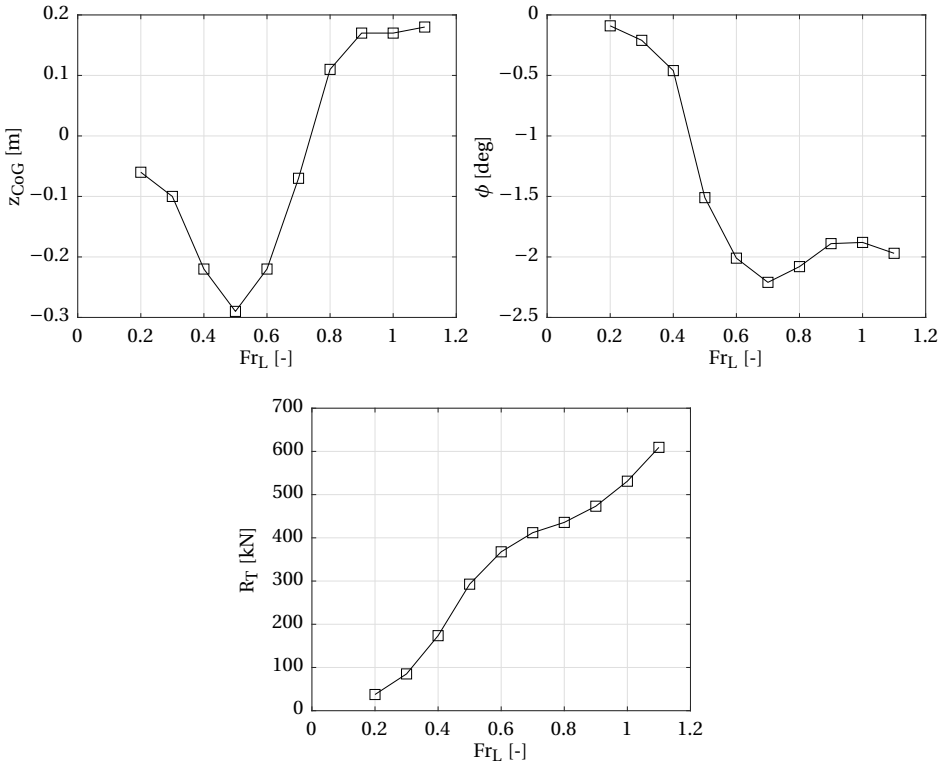

Figure 5.2: Results from calm water tests performed by Keuning and Van Walree (2006)

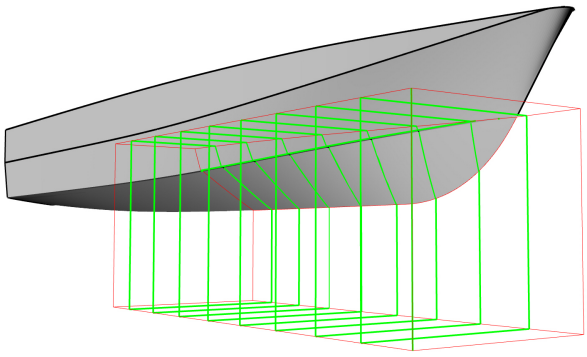

Figure 5.3: Schematic drawing of Multi Plane PIV test case with captive model in calm water

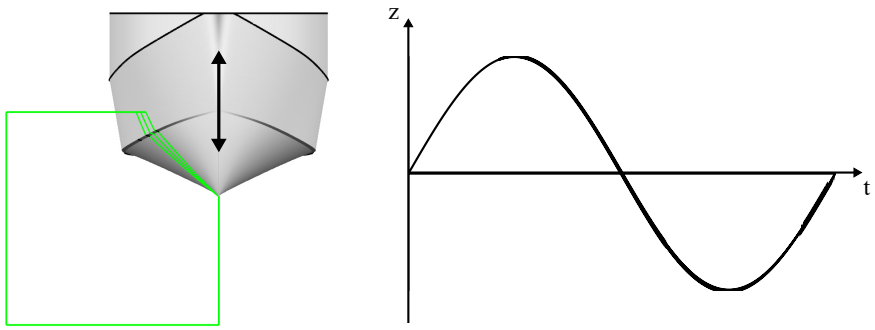

Figure 5.4: Schematic drawing of oscillation test case

as only global forces and motions were compared. For this reason, the usage of the pressure PIV technique for the pressure reconstruction on a moving ship model is further investigated, to measure the pressure field in the vicinity of the ship model. For simplicity, the model is not tested in regular waves but is subject to forced heave oscillations. This simplifies the synchronization with the PIV system and also allows for an assessment of the phase-averaged flow field. During the forced oscillation tests, the flow field is recorded in three successive planes which are perpendicular to the flow direction to obtain all necessary velocity components and their derivatives to reconstruct the phase-averaged pressure field. A schematic description of the test case is given in Figure 5.4, indicating the position of the ship with respect to the measurement plane. For all test cases, the model oscillates at a frequency of 1 Hz. This is comparable to the lower end of the wave encounter frequency range selected by De Jong (2011) during tests in regular waves. As described in Section 5.3, the PIV system acquisition frequency is limited to 50 Hz. For this reason, no higher oscillation frequencies are chosen to guarantee a sufficiently small time step. The model oscillates with amplitudes of 0.25 and 0.5 T, with T being the draft of the model. The longitudinal position of the measurement plane is determined with the help of CFD simulations, which are also used for a final comparison with experimental results.

5.2. NUMERICAL SIMULATIONS

To obtain a data set that can be used, for comparison of the measured velocity field and the derived pressures, additional CFD simulations are performed with the open-source code OpenFOAM 6.0. Simulations are conducted for the calm water conditions with the model set to a fixed trim and sinkage, as well as for the forced heave oscillations. Results from the forced heave oscillations are further used to determine a suitable measurement plane for the forced oscillation tests. For the solution of both problems, the two-phase transient solver interFoam is chosen to solve the incompressible unsteady Reynolds-

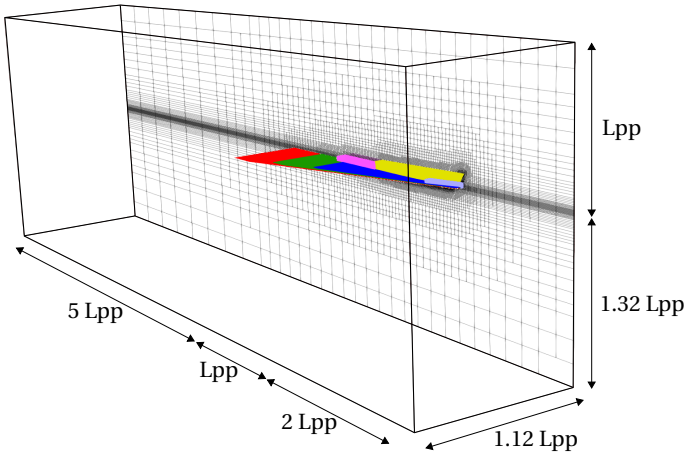

Figure 5.5: Computational domain

averaged Navier-Stokes equations. These are discretized with second-order accuracy. For turbulence modeling, the k-omega-SST model is used. The numerical grid is generated with the hexahedral mesher *snappyHexMesh*. As already mentioned in Chapter 4, the meshing procedure is modified, to allow for higher aspect ratio cells in the free-surface region and along the ship hull. The main dimensions of the numerical domain are chosen to fit the dimensions of the TU Delft towing tank, which is 4.5 m wide and 2.50 m deep. The position of the inlet and outlet are chosen according to the ITTC guidelines (ITTC (2011)) to prevent wave reflections. Due to the symmetry of the model, only one half of the ship model is meshed, to reduce the overall cell count and reduce simulation time. An overview of the domain, with all major dimensions, is given in Figure 5.5, including an indication of the different refinement regions for the wake and bow wave.

5.2.1. CALM WATER SIMULATIONS

To find the optimal mesh size and proof the grid independence of the final solution, a grid convergence study is conducted with a total of 4 meshes. The same procedure, already described in Chapter 4, is followed. During the systematic refinement of the numerical grid, the cell count is varied from 337,542 up to 2,291,617 cells. For the finest mesh, the target cell size of the smallest cells outside the boundary layer is specified as $Lpp/1000$, with Lpp being the length between perpendiculars at floating position. Choosing a grid refinement ratio of $r = \sqrt{2}$, the coarser meshes are generated, resulting in an edge length of $Lpp/353$ of the smallest cell outside the boundary layer for the coarsest mesh. The boundary layer is designed for all meshes to yield a dimensionless wall distance y^+ of 30 for the cell closest to the wall, which enables the correct application of wall functions

for modeling of the flow in the near-wall region. The growth ratio for the boundary layer cells is chosen as 1.2. The result of the grid refinement study is shown in Figure 5.6, where the total resistance for all four meshes is plotted over their normalized grid spacing. The ship speed selected for the refinement study is 3.32 m/s, which is equal to Fr_L 0.8, and the average y^+ value is within the range between 32 and 36 for all meshes. While the red dots indicate the total resistance from the CFD simulations, the green square shows the Richardson extrapolate, which gives an estimate of the total resistance at zero grid spacing. While the grid refinement ratio is constant, the order of convergence is determined with the solutions from the three finest grids $f_{1..3}$:

$$p = \frac{R_T(1) - R_T(\sqrt{2})}{R_T(\sqrt{2}) - R_T(2)} / \ln(r) \tag{5.1}$$

The determined order of convergence for these grids is 1.7. This value is used for the calculation of the extrapolated solution at zero grid spacing which is:

$$Pr_{h=0} = R_T(1) + (R_T(1) - R_T(\sqrt{2}))/(2^p - 1) \tag{5.2}$$

To give a measure of the percentage, the computed value differs from the asymptotic value, the grid convergence index is calculated according to Roache (1998) as:

$$GCI = \frac{F_s|\epsilon|}{r^p - 1} \tag{5.3}$$

with ϵ being the relative error between the two finest grids and F_s being a factor of safety, which is 1.25. For the two finest grids, the GCI is obtained to be 0.98 %.

The total resistance is used as an initial indicator for grid independence. However, for the comparison with PIV measurements, the pressure distribution in the bow region is of larger interest. Figure 5.7 gives an overview of the hydrodynamic pressure distribution on the ship hull for the finest mesh at Fr_L 0.8, showing the high pressure regions at the front of the bow and within the bow wave. To investigate the influence of the grid on the pressure distribution on the ship hull, the hydrodynamic pressures are investigated at three different sections $P1$, $P2$, $P3$, whose position is indicated in Figure 5.7. In Figure 5.8, the hydrodynamic pressure coefficient Cp on these sections is plotted over the height of the ship hull for all four grids with different refinement levels. For the three finest meshes, a good overall agreement can be found, with only minor differences. The pressure distribution obtained with the coarse grid, however, shows larger deviations in the region close to the chines. While the previously analyzed resistance monotonically converges with grid refinement level, the analysis of the local pressure distribution shows a fluctuation of the hydrodynamic pressures, within a narrow band. Eventually, the finest mesh is chosen to be used for the calm water simulations. For the simulations

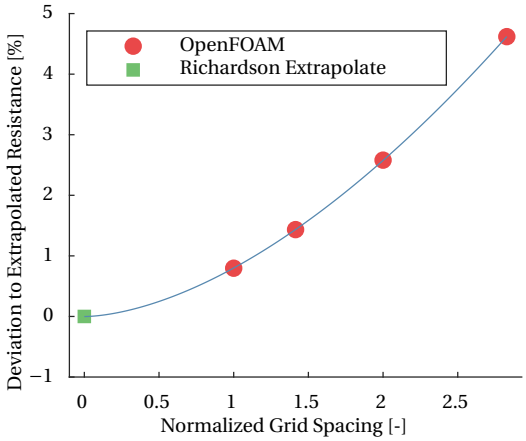

Figure 5.6: Grid convergence study: Total resistance of grids with systematically varied grid refinement and extrapolated resistance value at zero grid spacing

with forced oscillations of the ship model, the medium-sized mesh is used to reduce the computational costs of the transient simulations.

5.2.2. FORCED OSCILLATION SIMULATIONS

For the simulation of forced heave oscillations also the interFoam solver and additionally the dynamicMotionSolverFvMesh class are used. With specifying the sinusoidal motion for the ship hull,a Laplace equation is solved to calculate the updated position of the grid points at every time step. Mesh morphing is inversely proportional to the distance from the ship's hull patches. To specify the final location of the PIV measurement plane for the experiments, the temporal evolution of the pressure distribution in the bow region is looked at. Figure 5.9 and 5.10 show the hydrodynamic pressure distribution in the bow region during the downward motion of the ship between $\pi/4$ and $\pi/2$, for heave amplitudes of 20 % and 40 % of the ship's draft. In both cases, the peak-pressure region close to the chine starts to build up with the immersion of the chine, which begins at approximately $x = 1.35m$ at the lower amplitude and at $x = 1.2m$ at the higher amplitude. From this analysis, the ship section at $x = 1.35m$ is chosen for comparison with the experimental results. The deadrise angle in the selected section of interest 42.5°.

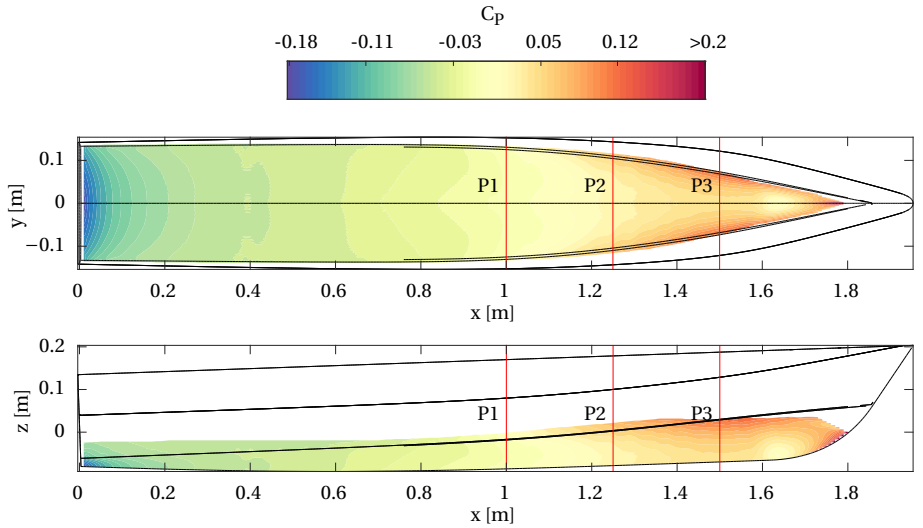

Figure 5.7: Pressure distribution of the ship hull at Fr_L 0.8

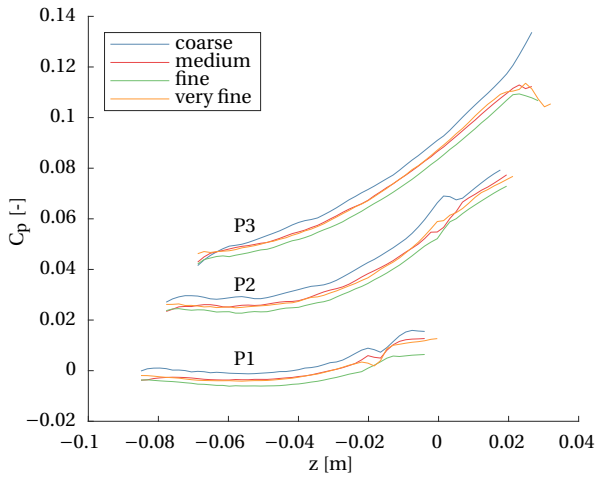

Figure 5.8: Comparison of local pressure distribution of different numerical grids at x=1 m ,1.25 m and 1.5 m

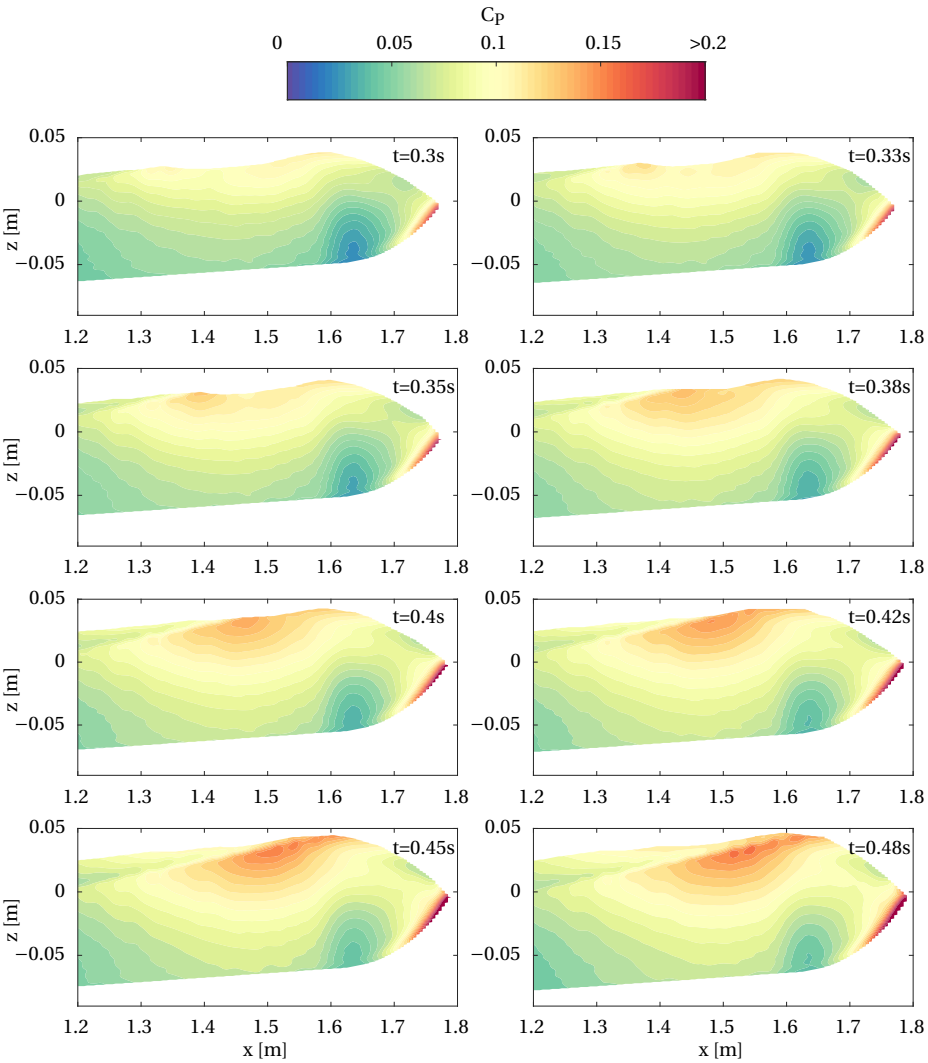

Figure 5.9: Temporal evolution of the pressure distribution in the bow region during forced oscillation simulations at Fr_L 0.6 with an amplitude of 0.0175 m

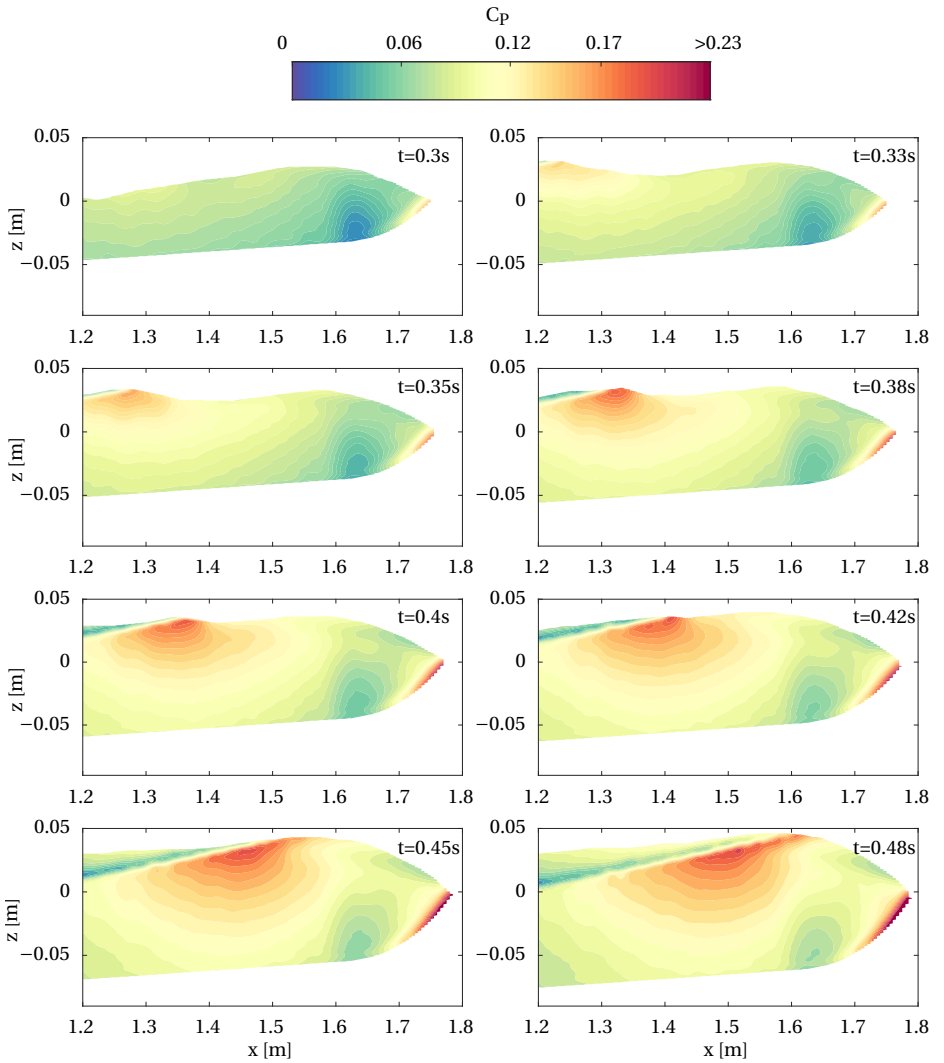

Figure 5.10: Temporal evolution of the pressure distribution in the bow region during forced oscillation simulations at Fr_L 0.6 with an amplitude of 0.035 m

5.3. EXPERIMENTAL SETUP

The towing tank experiments are carried out in the large towing tank of the ship hydrodynamics laboratory of TU Delft. The main dimensions and specifications of the tank are already introduced in Chapter 4. Both calm water tests with the captive model as well as forced heave oscillations, are conducted with the same setup. An overview of the setup is given in Figure 5.11, which shows the ship model mounted to a hexapod next to the stereo-PIV system. The hexapod is used to accurately position the model within the field of view of the PIV system and set the model to its correct running trim and sinkage. To increase the stiffness of the stereo PIV system, no traverse system is used to change the measurement plane position during the multi-plane PIV measurements in calm water. Instead, the hexapod is used to reposition the model during the test runs. During the forced oscillation tests, the hexapod is additionally used to perform the forced heave oscillations.

5.3.1. PIV SETUP

To record the flow field, the underwater stereoscopic PIV system, already presented in Chapters 2 and 4 is used. Due to the modularity of the system, the underwater housing is reconfigured to fit both camera sections in a single torpedo, with the intention to increase the stiffness of the PIV system and remove a large part of the vibration-induced disparity in-between cameras. The laser beam is guided through a separate strut below the water surface, where it leaves the strut through a cylindrical lens, forming the light-sheet perpendicular to the towing direction of the carriage. It has to be mentioned that the favored setup would have been to integrate the laser optics in the torpedo as well. However, this option was not available from the system supplier at the time that the tests were performed. A schematic drawing of the optical setup is shown in Figure 5.12. To reduce the disturbance of the flow in the measurement area, the foremost strut, that penetrates the water surface is at the same longitudinal position as the measurement plane. From this position, the underwater torpedo, that accommodates the camera system extends further to the front, to allow for a symmetric camera setup. Both cameras are looking at the measurement area through a water-filled mirror section, with mirror angles being 120 degrees with respect to the camera viewing direction. This symmetric arrangement with one camera on either side of the light-sheet and each camera looking at the measurement plane at an angle of 30 degrees is used to accomplish a high accuracy determination of the out-of-plane velocity component. The torpedo, which accommodates the camera system, has a horizontal stand-off distance of 1000 mm and is submerged 570 mm below the water surface. The camera sections are rotated by 30 degrees around the longitudinal axis of the torpedo, to look upwards at the measurement area. This enables a better view of the flow within the region of the bow wave. A photograph of the setup during operation

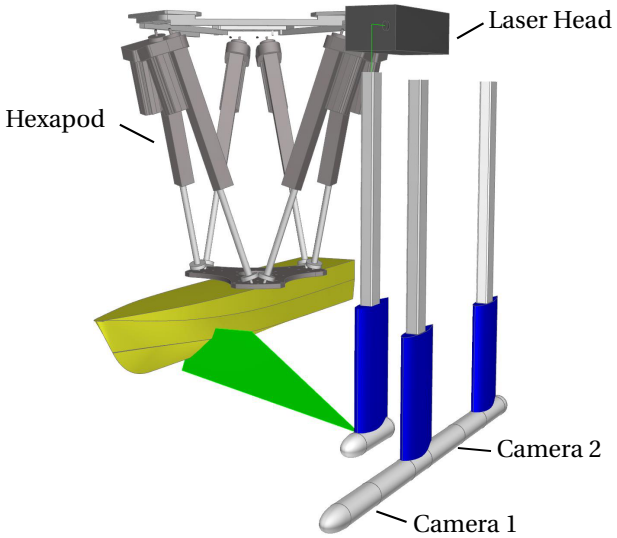

Figure 5.11: Experimental setup overview

in the towing tank is shown in Figure 5.13. While the setup described in Chapter 4 was operating at a recording rate of 7 Hz, the system is upgraded towards a higher acquisition rate. The measurement plane is illuminated with a Litron Nano PIV Nd:YAG laser with 50 mJ/pulse energy at a wavelength of 532 nm. The laser has two cavities, with each having a maximum repetition rate of 50 Hz. For image acquisition, two LaVision Imager MX 4M cameras with a sensor size of 2048 x 2048 pixels and 10-bit color depth are used. The cameras are capable of recording double frame images at a maximum frequency of 75 Hz. However, due to the laser specifications, the frame rate is restricted to recording double frame images at 50 Hz. The cameras have a pixel size of 5.5 x 5.5 μm^2 and are equipped with lenses of 28 mm focal length. This results in a field of view of approximately 250 x 250 mm^2 with a digital resolution of approximately 7 x 7 pixels/mm^2. As the viewing direction of the cameras was not perpendicular with respect to the measurement plane, a Scheimpflug-adapter is placed in front of the cameras, to keep particles focused over the whole field of view. Calibration of the cameras is done with a 320 x 320 mm^2 two-level double-sided 3d calibration plate, which is carefully aligned in an iterative process perpendicular to the moving direction of the carriage. Mounting the calibration plate to the hexapod enables for accurate repositioning of the plate during the calibration process. To guarantee a uniform distribution of the 50 μm polymer (Vestosint) particles in the measurement area, a retractable seeding rake is mounted in front of the carriage. Before releasing the particles into the towing tank in-between measurement runs, they are premixed in a high shear flow to prevent clustering. While after every measurement run,

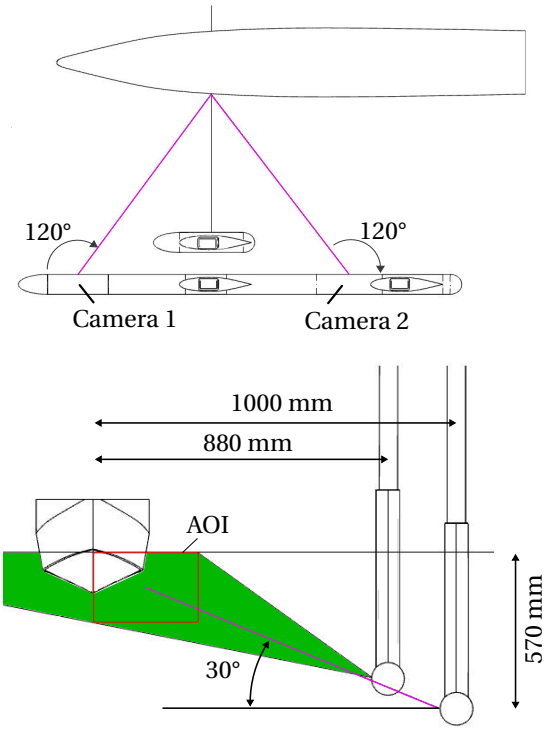

Figure 5.12: Schematic description of the optical setup

the tank is reseeded, a waiting time of 25 minutes allows the water to settle in-between runs. The data acquisition is done using the commercial software package DaVis 8.4.0 from LaVision.

For the calculation of the time-averaged velocity field, it is aimed at 400 vector images per measurement plane for the multi-plane measurements. Due to the image acquisition frequency of 50 Hz, velocity fields can be obtained in multiple planes within a single run. Therefore, the PIV system is triggered with a 5 V TTL signal generated by the hexapod control file, which starts the image acquisition once the model is moved to its new position. Taking into account the acceleration and deceleration phase of the carriage, the flow field is measured in up to 3 planes at Fr_L 0.8, which reduces the overall testing time. To guarantee a high temporal accuracy for the determination of the phase-averaged velocity field during forced oscillation tests, the PIV system is triggered at the beginning of every oscillation cycle to start a recording at 50 Hz. The drawback of this method is that the last three frames in every oscillation cycle have to be omitted to reset the trigger. At a carriage speed of 2.54 m/s, a total of 38 oscillation cycles are recorded per run.

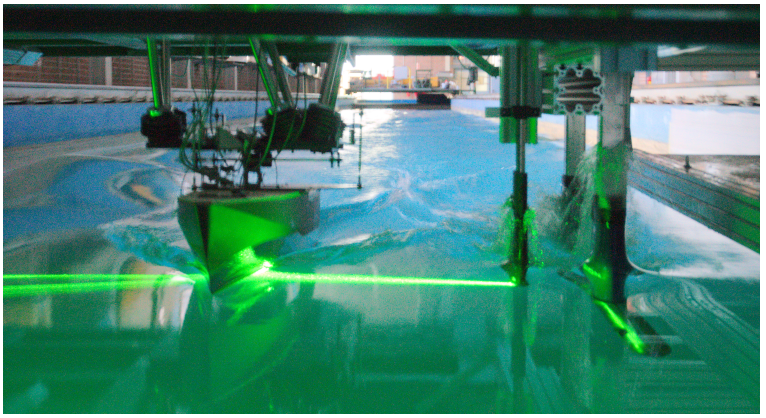

Figure 5.13: Photograph of Experimental setup during towing tank tests

5.4. FEATURE DETECTION AND MASKING OF PIV IMAGES

Before calculating the vector field from the recorded images, the free-surface and the ship hull need to be identified in the images. This is necessary for an accurate vector calculation close to the boundaries and an accurate description of the boundaries for the correct application of boundary conditions during pressure reconstruction from the velocity fields. While having obtained a total of 60 measurement planes during the multi-plane measurements and a total of 48 time-steps during oscillation tests, an automated procedure is needed to correctly identify the ship hull and the free-surface, which are varying in position and shape.

Figure 5.14 shows two examples of raw images taken during the multi-plane measurements at x=1.4 m and x=1.2 m. Both images are transformed to the world coordinate system using the obtained parameters from the initial calibration. In both pictures, the ship hull can be identified due to the high-intensity reflections of the laser-sheet. The free-surface, however, is hardly recognizable in both pictures, and its position and shape can hardly be obtained from these single images. Instead of having a clear border, the area above the water surface shows reflections of the particles from beneath the surface. The position of the free-surface can only be guessed from particle agglomerations (Figure 5.14 (right)) and disturbances of the free-surface due to wave breaking (Figure 5.14 (right)). For this reason, the identification of the free-surface and the ship hull will looked at separately. Image processing and feature identification are performed using MATLAB.

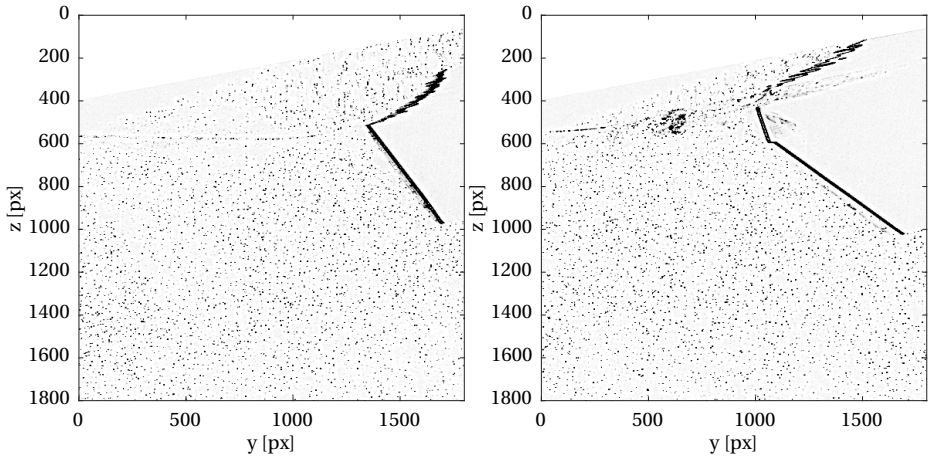

Figure 5.14: PIV raw images taken during the multi-plane measurement runs at x=1.3 m and x=1.5 m

5.4.1. SHIP HULL IDENTIFICATION

IMAGE FILTERING AND THRESHOLDING

As being interested in the detection of the high intensity reflections on the ship hull, initially, the PIV particles have to be removed from the images. The removal of small objects is done with morphologically opening an image with a specified structure element. Image opening is an erosion followed by a dilation, where all objects smaller than the used structure element are removed. In this case, a 3 x 3 structure element is used for PIV particle removal from the grayscale images. To account for small variations in the outline of the reflections on the ship hull due to small changes in intensity, the image is morphologically closed. By also using a 3 x 3 structure element, this operation performs a dilation followed by an erosion to fill small holes in the foreground of the picture. To apply the final feature detection, the image needs to be binarized. For this, a threshold value is needed. To keep the user input to a minimum during the identification procedure, the threshold level is automatically chosen, by using Otsu's method (Otsu (1979)). Assuming that the reflections on the ship hull are significantly different from the rest of the image, which is considered as background noise, the image pixels can be divided into high-intensity foreground pixels and low-intensity background pixels. Dividing the image in these two classes of pixels, Otsu's method calculates the optimal threshold by finding the maximum inter-class variance. To remove spurious elements from the image and smoothen the contour of the reflections on the hull, the images are again morphologically opened and closed. On the top-left of Figure 5.15, an example of the final binarized image is given, which is used for feature detection.

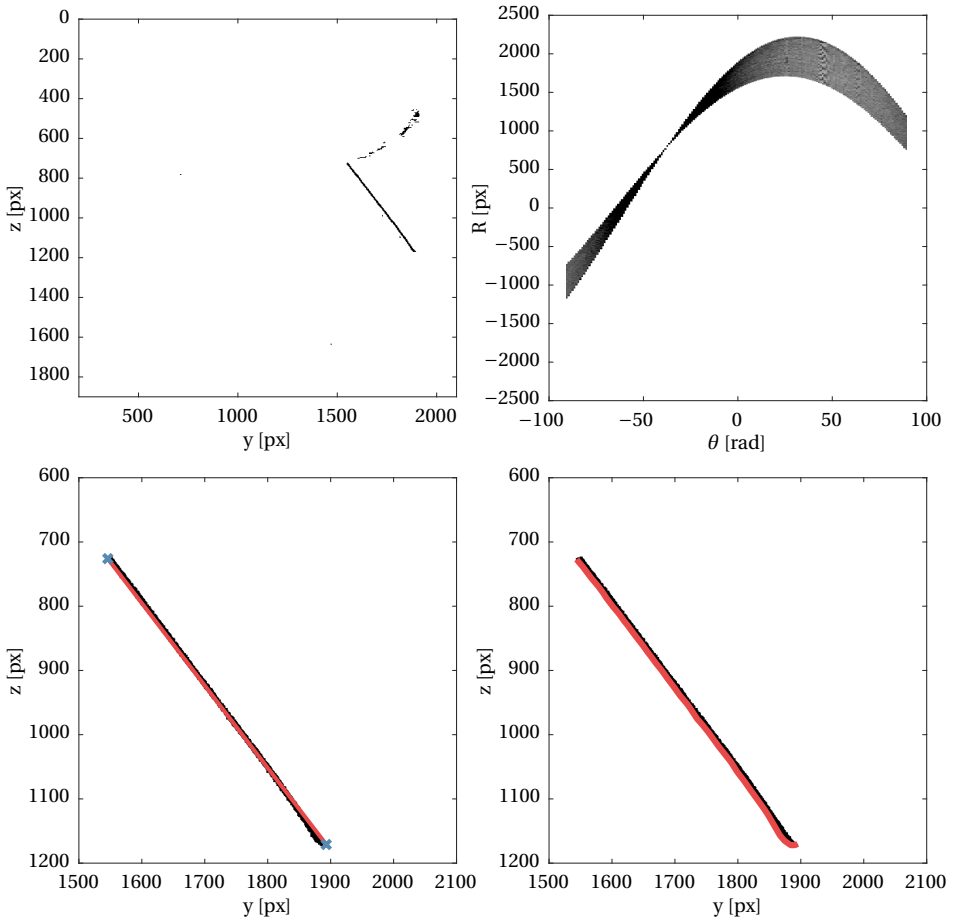

Figure 5.15: Ship hull identification procedure: filtered image of Figure 5.14 (left), (top left); Hough transform (top right); identified line (bottom left); lower edge of ship hull (bottom right)

FEATURE IDENTIFICATION

For the final feature identification and extraction step, it is made use of the fact that the ship hull has a wedge-like shape, being visible as a single or a combination of straight lines in the image. After the largest objects are identified in the image, it is checked for every object if it has a line shape, starting at the manually defined centerline of the ship and a realistic deadrise angle in the range between 20° and 90°. If an object fulfills the preciously described criteria, its boundary is extracted for masking of the PIV image. Within the field of digital image processing, a well-known technique for the extraction of features and especially lines is the Hough transform (Duda and Hart (1971)). The Hough

transform of the previously filtered image is shown in Figure 5.15 (top-right). With a line through an arbitrary point (x_0, y_0) in the image, described in the polar coordinate system as:

$$r_\theta = x_0 \cdot \cos\theta + y_0 \cdot \sin\theta \, ds \tag{5.4}$$

a family of lines of different angles θ, with each line intersecting this point, can be created for $r > 0$ and $0 < \theta < 2\pi$. Plotting the properties r over θ of every line of the family results in a sinusoidal curve. In Figure 5.15 (top-right) this curve is plotted for every single point in the image. The intersection of curves results in increased intensity in these plots with the peaks indicating the angle and position of the dominant lines in the processed image. The herein used MATLAB function *houghLines* gives next to the angle and position also start and end of the detected line. Figure 5.15 (bottom-left) shows the image with the object that is identified as the ship hull and its associated line segment, which has been detected with the Hough transform. Also seen in 5.15 (bottom-right) is the lower boundary of the object, which is finally extracted with a moving maximum filter for masking the image.

The previously described procedure is applied for the identification of the ship hull in every measurement plane. Figure 5.16 (left) shows the identified ship hull outline in selected sections. It is seen that the proposed procedure successfully identifies the outline of the ship hull for a large range of deadrise angles. Furthermore, the procedure is also capable of identifying objects that consist of multiple connected straight lines, as seen from sections with submerged chine. Figure 5.16 (right) shows the identified section outline of the ship at x=1.35 m during the downward motion of the model at the forced oscillation tests. Also, here, the section outline is successfully captured for every position.

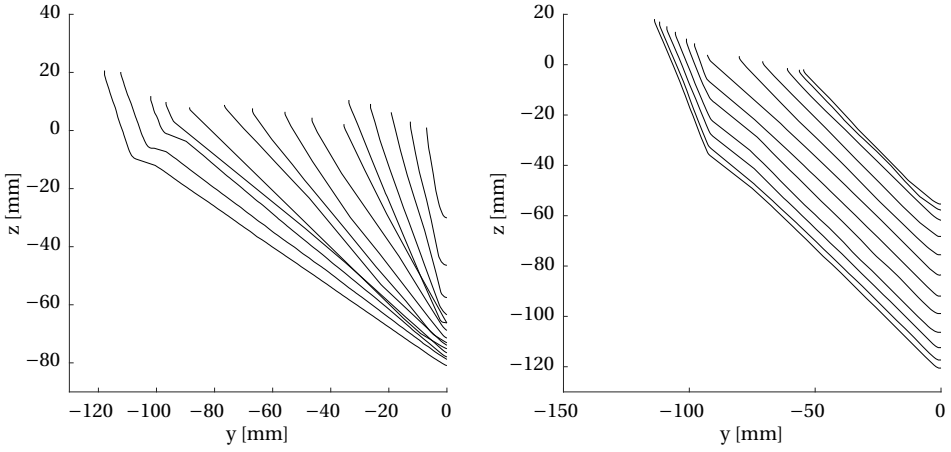

Figure 5.16: selected identified ship hull sections: multi-plane measurements (left), oscillation tests (right)

5.4.2. FREE-SURFACE IDENTIFICATION

TEMPORAL FILTERING

As initially stated, the free-surface can hardly be identified from a single picture. Due to the unfavorable viewing angle of the cameras, the area above the waterline shows mirror images of the PIV particles, and no clear border is visible to identify the water-air interface. However, by having a closer look at the images, which are re-plotted in Figure 5.17, the position of the free-surface can be guessed due to small particle agglomerations in this area and small high-intensity areas from air entrainment due to the breaking bow wave. To improve the visibility of the free-surface in the images, a temporal filtering procedure is introduced. As the particles in the flow field change position in between images, the images are binned in groups of 10 pictures. Images of every group are then added on top of each other, to increase the number of particle agglomerations at the surface. Isolated PIV particles are removed by morphologically opening the image. The final images, as seen in Figure 5.17 (bottom) are the sum of all bins, which are morphologically closed to remove local variations of intensity. Compared to the initial images, the free-surface, as well as the region of the disturbance of the free-surface due to the breaking bow wave, can now be identified.

PIECE-WISE SURFACE DETECTION

For the final extraction of the free-surface and its lower boundary, the image is masked with the identified ship hull. Furthermore, it is binarized using an appropriate threshold value. As already applied for the ship hull identification, Otsu's method is used to find the best threshold value to guarantee a fully automatized identification of the free-surface. However, the application of Otsu's method to the entire picture does not give satisfying results, due to small variations of intensities in the background and the free-surface itself. To overcome this problem, a piecewise surface identification procedure is introduced, which considers a local threshold within a certain window. The steps of the procedure are shown in Figure 5.18 and 5.19 (top). The method starts the identification at the image boundary and moves along the free-surface towards the ship. The starting point for the initial window is chosen from the still water position during the calibration procedure. Within the initial window, the local threshold is determined, and the free-surface is approximated with a line through a Hough transform. In case the approximation is successful, the outline of the free-surface is determined. The detected line is used to predict the location of the next segment, where the previously described procedure is repeated. If no line can be detected within a window, the line detection stops. With this procedure, the approximate outline of the free-surface is specified. In a final step, a new threshold is calculated for the area within the specified outline, which enables a better approximation of the lower boundary of the surface. The result of the procedure is shown in Figure 5.18 and 5.19 (bottom) for images with and without breaking waves.

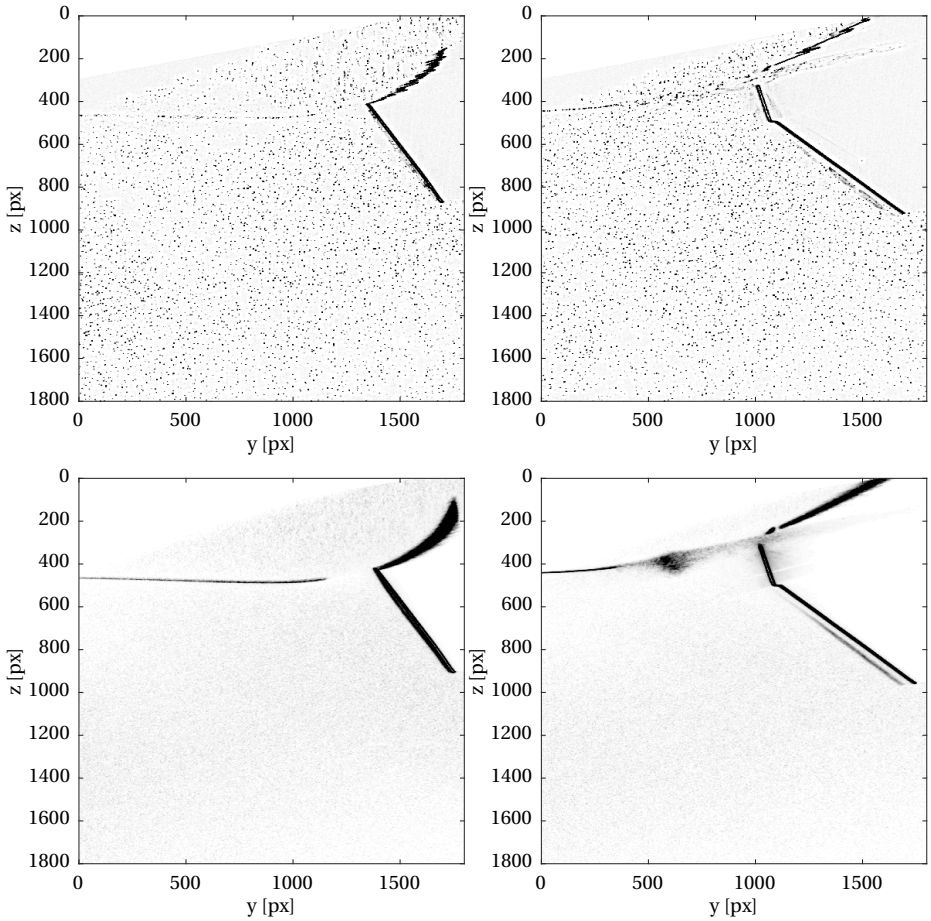

Figure 5.17: Comparison of enhanced raw images (top) and time-filtered images (bottom)

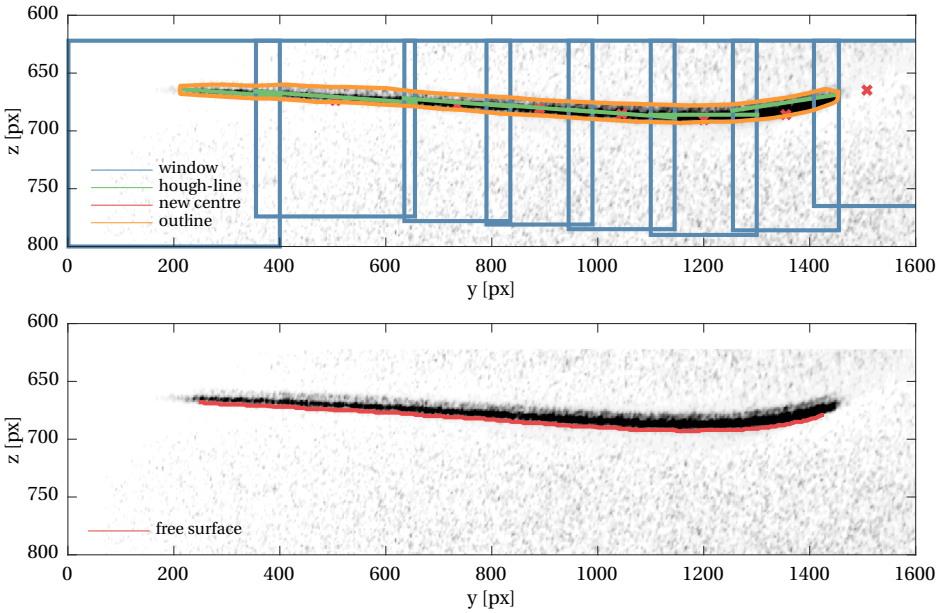

Figure 5.18: Free-surface identification procedure (top) and final identified lower edge of free-surface (bottom) at x=1.5 m

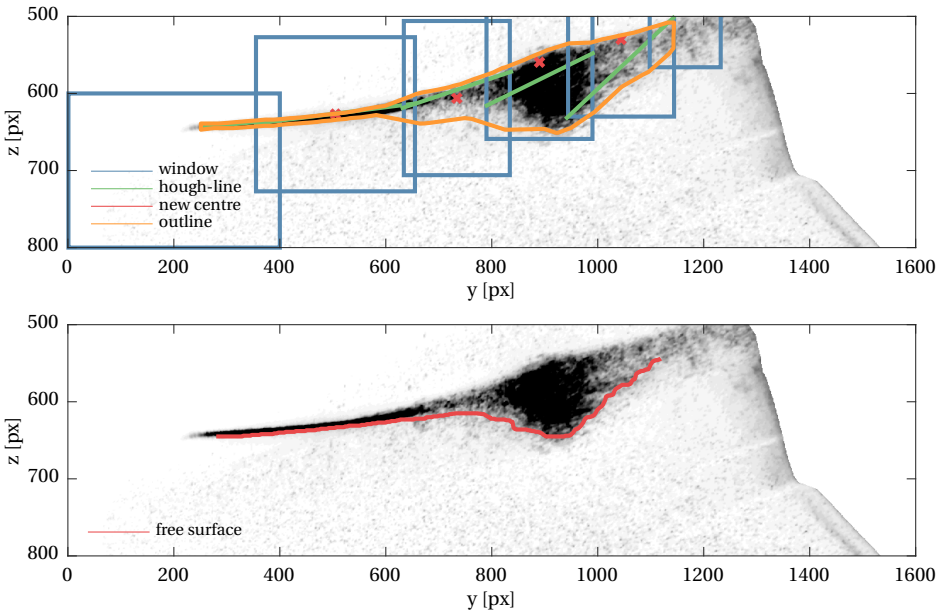

Figure 5.19: Free-surface identification procedure (top) and final identified lower edge of free-surface (bottom) at x=1.3 m

5.5. VECTOR FIELD CALCULATION AND DATA REDUCTION

After the application of the individual masks to each image, the calculation of the velocity vector field is done in multiple correlation iterations. Starting with an interrogation window of 64 x 64 pixels in the initial pass, the window size is iteratively decreased to 24 x 24 pixels. The windows are overlapping by 75 %, and a Gaussian weighting function is used. Being ultimately interested in the mean value and other statistical properties of the flow, robust outlier detection is needed in between passes, as already a small number of false vectors can significantly change the final result. For this reason in-between passes, a 4-pass regional median filter is used to reject groups of spurious vectors. This type of robust outlier detection is well suited to remove most of the outliers, although with the drawback that some good vectors might be rejected, too.

5.5.1. MULTI-PLANE MEASUREMENTS

Figure 5.20 shows an example of the out-of-plane and in-plane velocity components from the mean velocity field which was obtained from 400 vector images. To investigate the convergence of the time-averaged value, the residual of the mean value $|\overline{u_{xi}} - \overline{u_{xi-1}}|$ is evaluated for a single point P close to the ship hull, which is depicted in Figure 5.20. The result from the convergence analysis is shown in Figure 5.21. For all components the residual shows a clear convergence. After 150 samples, the mean value of all components is converged and oscillates around 10^{-4} m/s with maximum values of $4 \cdot 10^{-4}$ m/s.

For further processing of the multi-plane measurements, the time-averaged velocity fields of all measurement planes are combined to a discrete description of the volumetric velocity field. Therefore, the velocity field data is converted to a regular numerical grid, which can be handled by the open-source code OpenFOAM. Figure 5.22 shows the reconstructed volumetric velocity field from a total of 60 measurement planes and its position relative to the ship model. The grid spacing in the longitudinal direction of the ship is 1 cm and equal to the original spacing of the PIV measurement planes. The grid spacing along the y and z-axis is 0.0018 m, resulting in a total grid size of approximately 10^6 cells. With the information from the masking procedure, the outer surface of the domain is split into separate patches to allow for the application of different boundary conditions on the ship and the free-surface during the final pressure reconstruction.

SPATIAL SMOOTHING

As the volumetric description of the flow field is obtained from planar measurements, small discontinuities are expected in between these planes. In particular, it is expected that the flow fulfills the divergence-free condition. However, as the pressure Poisson equation assumes that the flow is divergence-free, this eventually influences the quality of the reconstructed pressure field. For this reason, the divergence-free correction scheme (DCS), which was first proposed by De Silva et al. (2013), is implemented for smoothing of

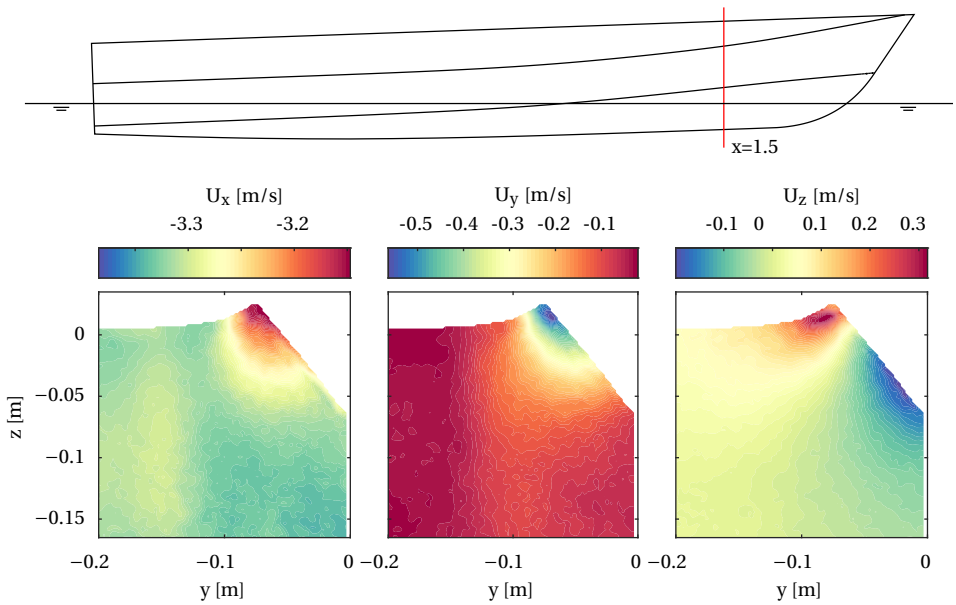

Figure 5.20: Time averaged velocity field components at x=1.5m

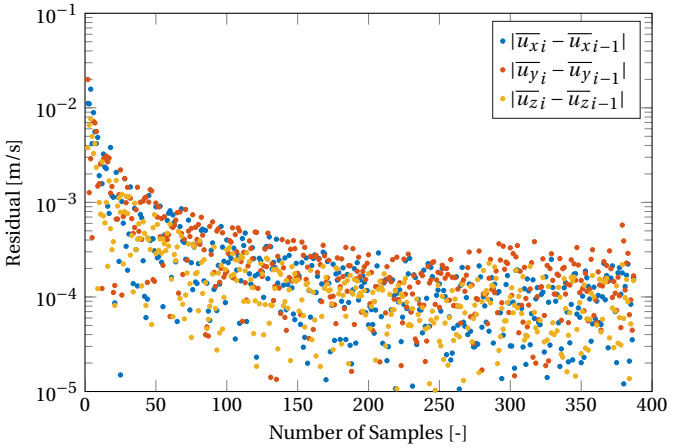

Figure 5.21: Convergence analysis of the temporal mean for the three velocity components U_x, U_y, U_z, evaluated at a single point P within the measurement plane at x=1.5 m.

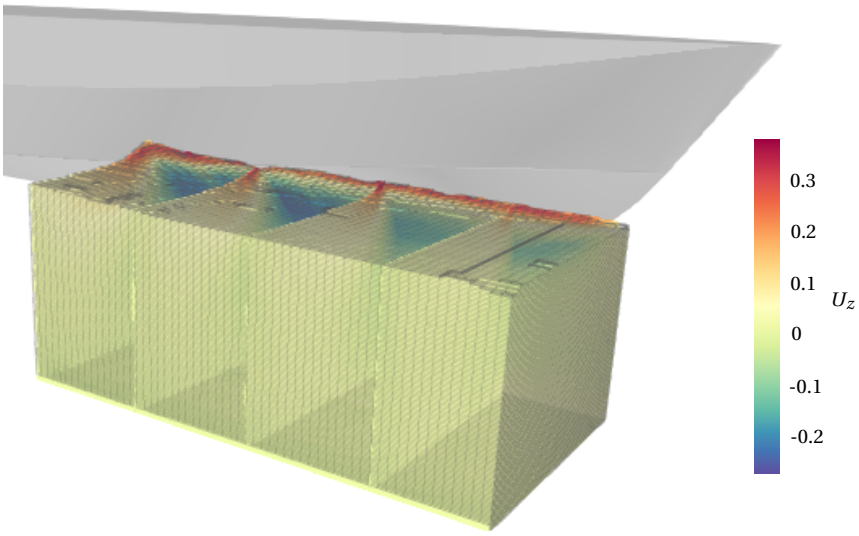

Figure 5.22: Example of the reconstructed volumetric velocity field.

the velocity field. The approach is based on the solution of a constrained minimization problem. The objective is to minimize the energy of the difference between the velocity fields from PIV measurements u_{PIV} and their corrected field u_{corr} with the additional constraint, that the corrected velocity field is divergence-free:

$$\min_{u_{sol}} \int (u_{sol} - u_{PIV})^2 \, d\Omega \quad \text{with} \tag{5.5}$$

$$\nabla \cdot u_{sol} = 0 \tag{5.6}$$

While De Silva et al. (2013) solved the problem using MATLAB's *fmincon* solver to find the minimum of the constrained function, Azijli and Dwight (2015) noted, that the minimization problem can be reformulated to a quadratic programming problem with linear equality constraints. With the introduction of the Lagrange multiplier, the problem can be formulated with the help of a Lagrange function, which eventually results in the following system of equations:

$$2u_{sol} - 2u_{PIV} - \nabla\lambda = 0 \tag{5.7}$$

$$\nabla u_{sol} = 0 \tag{5.8}$$

,with λ being the Lagrange multiplier. As the measurement data format is already converted to the OpenFOAM data format, the minimization problem is also solved within this toolbox as an optional pre-processing step prior to the solution of the pressure equation. An advantage of the DCS is that no further boundary conditions are needed.

5.5.2. OSCILLATION TESTS

Image acquisition during the oscillation tests is synchronized with the motion of the hexapod and each oscillation cycle stored in a separate data set with each image associated with a fixed phase-angle. With performing 38 oscillation cycles per carriage run, for each condition, a total of 190 cycles were recorded in three consecutive measurement planes, ultimately resulting in 190 vector images per assessed phase-angle. From these images, the phase-averaged velocity fields are calculated for 48 phase angles. Figure 5.23 shows the in-plane components of the obtained phase-averaged velocity fields during the downward motion of the ship at three selected phase angles, equal to 0.1, 0.22 and 0.34 s within the oscillation cycle. Figure 5.23 (top) shows the vertical position and vertical velocity of the ship during the oscillation cycle with an indication of the selected phase angles where the velocity field components are evaluated.

TEMPORAL SMOOTHING

As already mentioned, for the determination of the phase-averaged pressure field during the forced oscillation tests, it is necessary to account for the complete material acceleration. This includes next to the convective term, the time derivative of the velocity field. Due to the phase-averaged manner in which the velocity field is obtained, it is expected that the time signal of the velocity field is not smooth, and the noise from the phase-averaged velocity fields ultimately affects the quality of the temporal derivative. To evaluate the quality of the time signal of the velocity field and its effect on the derived acceleration, the velocity field is examined for a single point located close to the ship hull. The exact position of the point P is indicated in Figure 5.23. Figure 5.24 shows the time traces of the three phase-averaged velocity components at this location and their standard deviation (blue), both calculated from 190 samples. For all velocity components, a clear sinusoidal signal is obtained as a response to the forced oscillations. However, for all signals, small discontinuities can be observed. Calculating the temporal derivative of the velocity time-trace by using a central-differencing scheme (green), the noise from the velocity time-trace is amplified. To improve the quality of the acceleration signal, the velocity field is smoothed by performing a piece-wise second-order polynomial regression, using a Savitzky-Golay filter (Savitzky and Golay (1964)). The red line shows the result of the application of the filter, which is close to the original velocity time-trace. However, by looking at its temporal derivative (orange), an improvement of the acceleration signal has been obtained due to the filter.

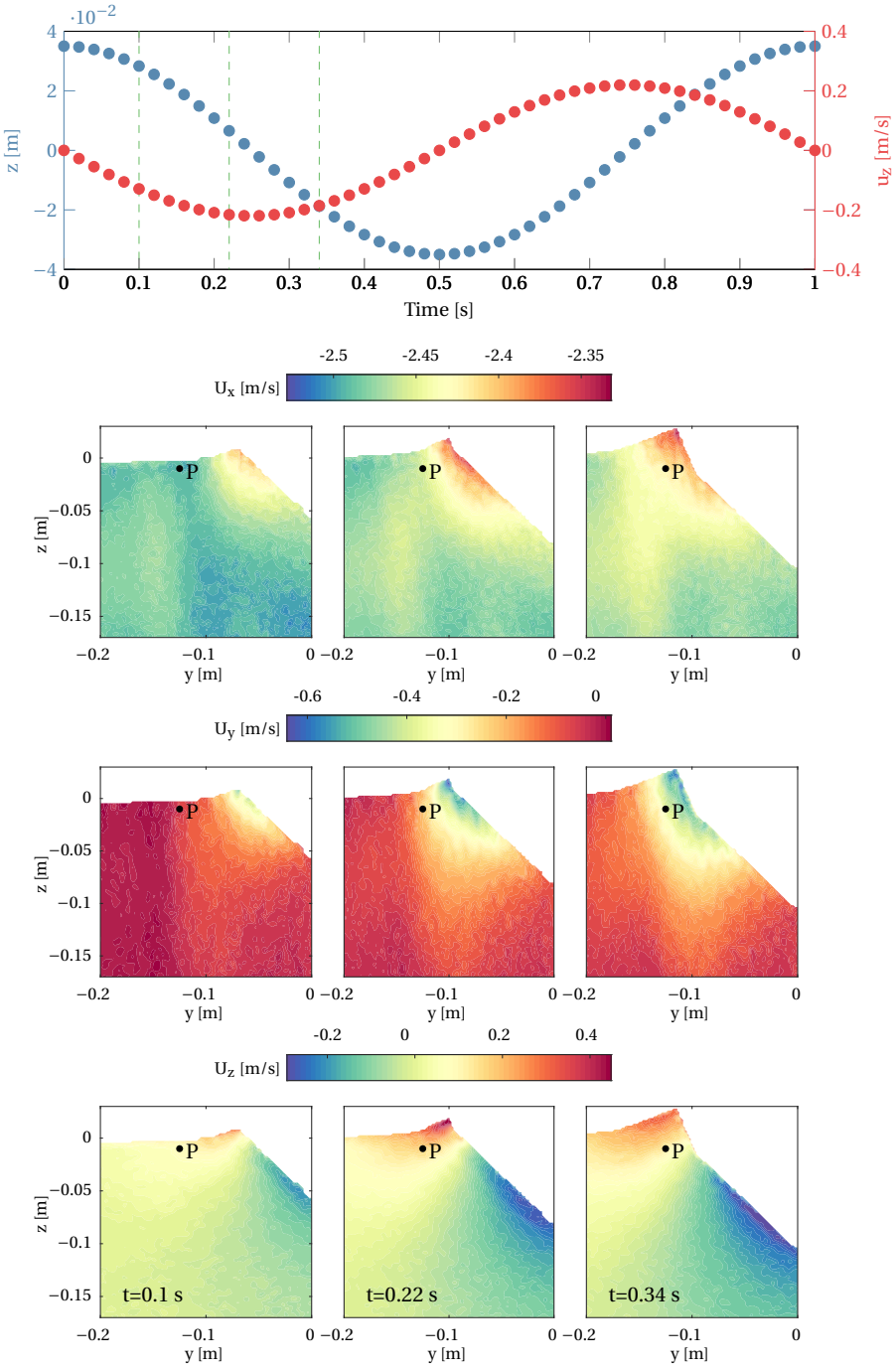

Figure 5.23: Phase-averaged velocity components at three selected time instants during the downward motion of the ship

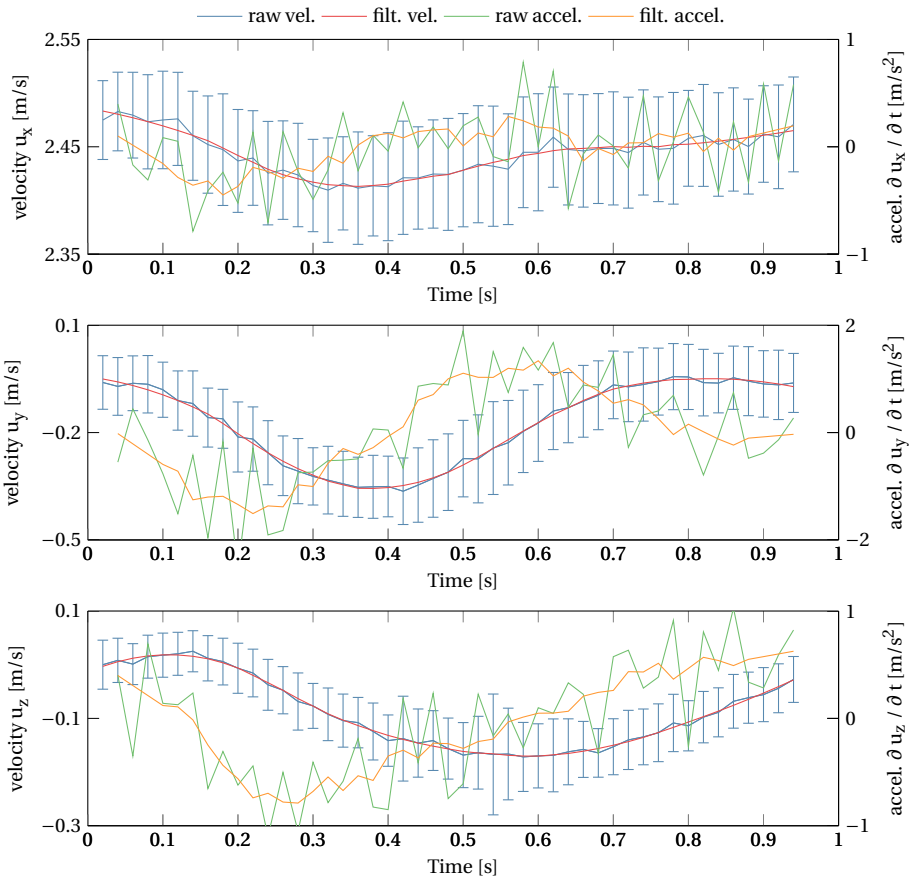

Figure 5.24: Time traces of the raw velocity components and accelerations and results after application of a Savitzky Golay Filter at a single point P within the measurement plane.

5.6. PRESSURE RECONSTRUCTION

After the determination of the phase-averaged velocity fields and appropriate spatial and temporal filtering, the hydrodynamic pressure distribution in the flow field can be obtained from the solution of the pressure Poisson equation, which is derived from the Reynolds-averaged momentum equation. Already introduced in Chapter 3 and 4, the equation is reproduced here for further clarity.

$$\frac{\partial^2 \overline{p}}{\partial x_i^2} = -\rho \frac{\partial}{\partial x_i} \left(\overline{u}_j \frac{\partial \overline{u}_i}{\partial x_j} + \frac{\partial \overline{u_i' u_j'}}{\partial x_j} \right) \tag{5.9}$$

As already described in Chapter 3, under consideration of the divergence-free condition $\nabla \cdot u = 0$, the local acceleration and the viscous term disappear. The spatial derivatives are obtained with central differences from the spatially smoothed velocity field. The Reynolds stresses are found from variances and covariances of the velocities. Figure 5.25 shows a cross-section of the numerical domain with the different patches, which are obtained from the feature identification procedure. This allows for the application of different boundary conditions on the ship and the free-surface. While the pressure on the water surface is equal to the atmospheric pressure $p = p_a$, a Dirichlet boundary condition is imposed on the 'free-surface' patch, for both, the scanning tests as well as the oscillation tests. Due to the symmetry of the ship model and the flow field with respect to the center-plane of the ship model, a symmetry boundary condition is imposed here which sets the patch normal components to zero. For the remaining patches, a Neumann boundary condition has been obtained from the momentum equation, which specifies

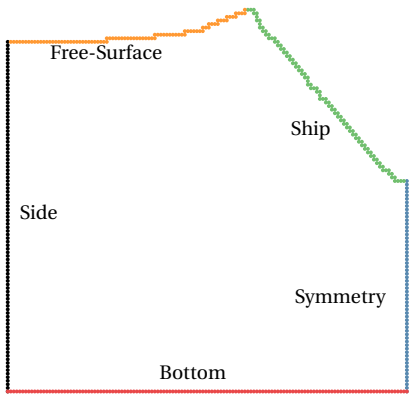

Figure 5.25: Cross section of numerical domain boundary split into different patches for the application of suitable boundary conditions

the pressure gradient in normal direction:

$$n_i \cdot \frac{\partial \overline{p}}{\partial x_i} = -\rho n_i \cdot \left(\frac{\partial \overline{u_i}}{\partial t} + \overline{u}_j \frac{\partial \overline{u}_i}{\partial x_j} - \nu \frac{\partial^2 \overline{u}_i}{\partial x_j \partial x_j} + \frac{\partial \overline{u_i' u_j'}}{\partial x_j} \right) \tag{5.10}$$

The temporal derivative of the velocity field is only included for the oscillation tests. The velocity and acceleration values of the moving ship hull, are obtained from the hexapod signal.

Figure 5.26 gives a first impression of the reconstructed pressure field in the vicinity of the ship model. The pressure field is reconstructed from the volumetric description of the velocity field, which is obtained from multi-plane PIV measurements. Results are presented at three selected slices perpendicular to the moving direction of the ship model. At all displayed positions, a clear high pressure region is found in the spray root. The size of this high pressure region and the peak pressure are increasing by shifting the measurement plane towards the aft of the ship. In measurement plane x_1, the chine of the ship is within the spray root of the bow wave, leading to the highest pressure increase in this region. The limited optical access prevents a full determination of the pressure field within the jet region, which is formed on the ship hull within the bow wave. However, the spray root, where the highest pressure is expected, is well captured in all measurement planes.

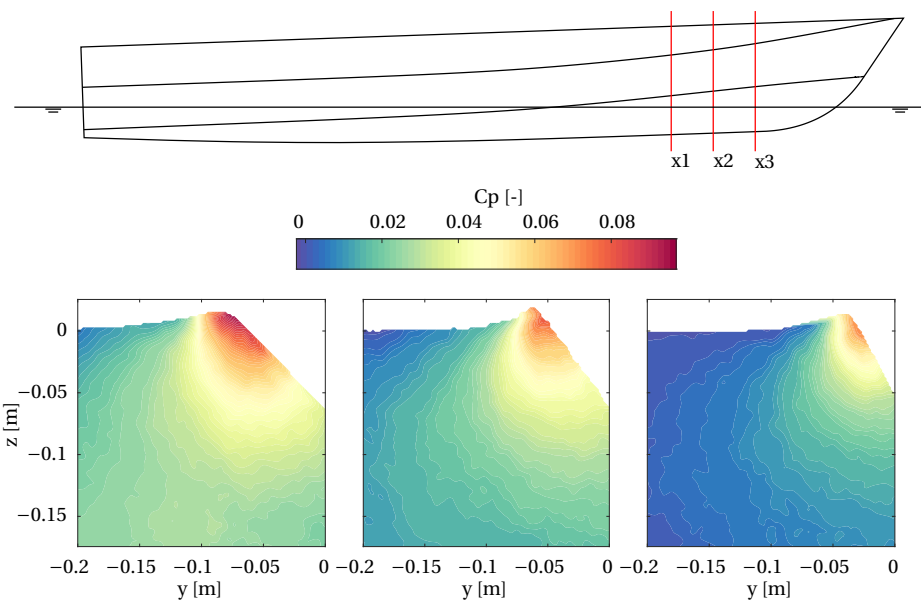

Figure 5.26: Time averaged pressure field at x=1.4 m 1.5 m and 1.6 m

A first impression of the pressure field in the vicinity of the oscillating ship model is shown in Figure 5.27. As indicated in Figure 5.27 (top), where the vertical position (blue) and velocity (red) of the ship during an oscillation cycle are given, the pressure field is presented at six selected time steps during the downward motion of the ship. While the ship is moving downwards, the magnitude of its vertical velocity increases initially. At the same time, also a high pressure region is formed at the intersection of the ship hull with

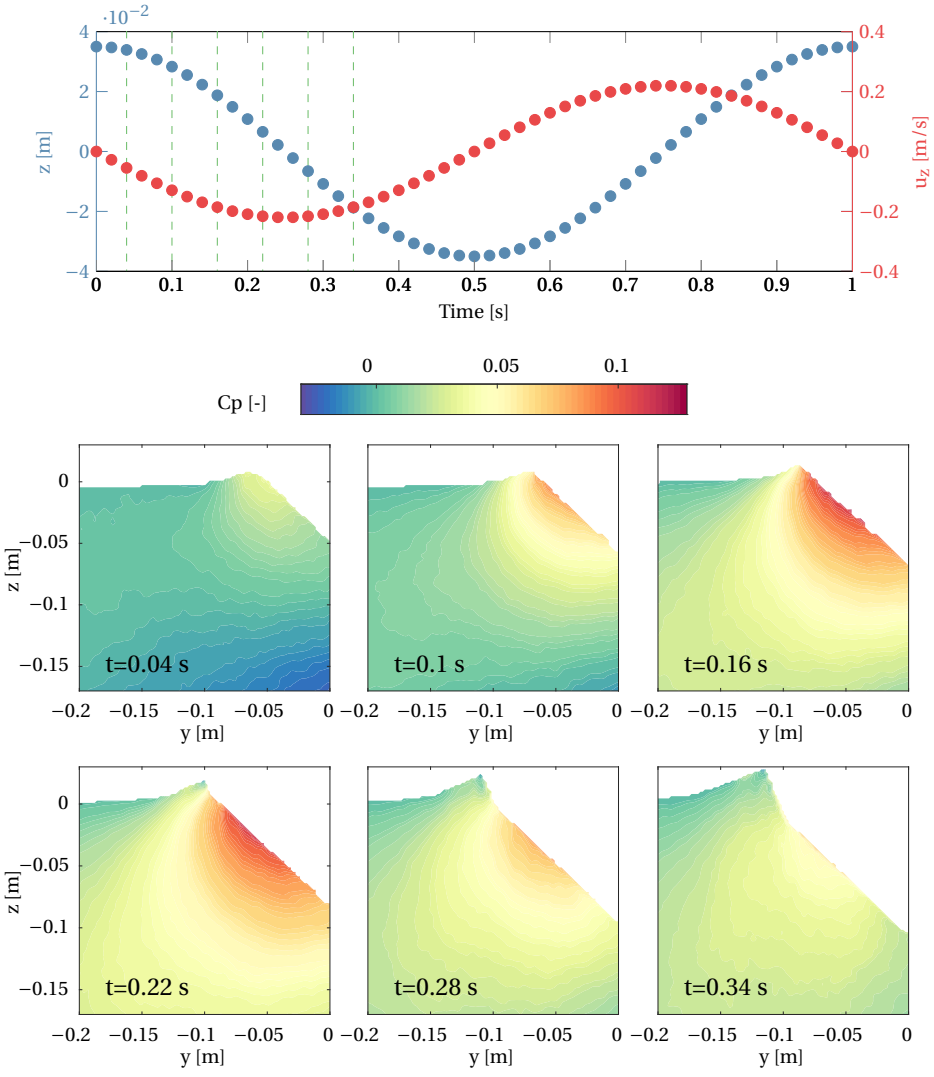

Figure 5.27: Phase averaged pressure field at selected time instants during the downward motion of the ship hull

the free-surface, which increases until the maximum vertical velocity is reached. Towards the end of the downward motion, the vertical velocity is decreasing and thus also the high pressure region. After the immersion of the chines at t=0.22 s, the pressure peak is moving away from the intersection of the ship with the free-surface. A more detailed discussion of the results from multi-plane measurements and oscillation tests and a comparison with numerical results is presented in Section 5.8.

5.7. MEASUREMENT UNCERTAINTY ASSESSMENT AND PROPAGATION

Before velocity fields from PIV measurements and the reconstructed pressure fields are compared to numerical results, a brief discussion of the uncertainty of the obtained velocity fields is given. Further, it is investigated how these influence the final pressure field. While ultimately being interested in the statistical quantities of the measured velocities, the following discussion mostly focusses on the random errors, which are typically dominant due to the finite sample size.

In accordance with the uncertainty assessment procedure performed in Chapter 4, uniform flow measurements are performed for an initial judgment of the random uncertainty components and the bias from any misalignment of the laser-sheet with the towing tank coordinate system. While in Chapter 4, the measurement plane is aligned with the main flow direction. In this case, the measurement plane is oriented normal to the main flow direction. In case of the uniform flow measurement in which the flow speed is equal to the carriage speed, and thus only an out-of-plane velocity component is expected with no in-plane velocities. Table 5.2 shows the main results from the uniform flow measurements at a towing tank carriage velocity of 3.32 m/s. Next to the statistical quantities, also the root mean square of the random uncertainties, assessed with the correlation statistics method of Wieneke (2015), which is introduced in Chapter 4, are shown for comparison with the standard deviation of the measured velocities. By looking at the out-of-plane velocity component and its equivalent pixel displacement, it has to be mentioned again, that the pulse separation Δt and thus the particle displacement was limited by the light-sheet thickness. To prevent any out-of-plane particle loss, particle displacement is one-quarter of the light-sheet thickness (Adrian and Westerweel (2011)). Especially in the case of high carriage velocities and measurements close to the ship hull, the large dynamic range thus results in a lower resolution. The bias of all three velocity components has a maximum value of 0.07 pixels, while the standard deviation varies between 0.15 and 0.16 pixels for the x and z-component and 0.23 pixels for the y-component. The same trend is also reproduced by the RMS values of the uncertainties obtained with the correlation statistics method. The larger standard deviation and RMS uncertainties in the y-direction indicate a slightly stretched correlation peak in this

Vel. [m/s]	Comp.	Mean [px]	Bias [px]	Error std. dev. [px]	Uncertainty RMS [px]
3.32	x	5.68	0.04	0.16	0.12
0	y	0.06	0.06	0.23	0.17
0	z	0.07	0.077	0.15	0.075

Table 5.2: Comparison of bias, errors and uncertainties from uniform flow tests for the different velocity components

direction. The reason for this can be found in the thickness of the light-sheet, which is increased to a maximum to increase the pulse separation Δt. As described in Chapter 2, the particle images of both cameras cannot match perfectly due to the finite thickness of the light-sheet. This results in a broader correlation peak, with its major axis, spanned by the viewing axes of both cameras. Under the assumption of perfectly still water during the uniform flow measurements, the standard deviation of the measured velocities should match the RMS of the estimated uncertainties. While the trend is well reproduced, with the highest uncertainty being in the y-direction, all uncertainties, determined with the correlation statistics method, are slightly lower. An explanation for this difference might be the fact that the assumption of perfectly still water does not completely hold true. As the measurement area is seeded with the help of a seeding rake prior to every run, small fluctuations might still be present, even after a waiting period of 25 minutes.

As shown in Chapter 4, the uncertainties obtained from uniform flow measurements, only give an initial indication of the bias and random errors. They do not take into account that due to local flow characteristics, the uncertainty during the real measurement can significantly differ from those obtained in uniform flow measurements. Furthermore, any influence of reflections from the model which influences the correlation quality is not taken into account. Figure 5.28 shows the RMS uncertainty obtained with the correlation statistics method from a total of 400 images. It is seen, that the uncertainty, obtained from the uniform flow measurements, can only be matched further away from the model. While the ship is painted mat black to minimize any reflections, these could not be completely removed. The laser-sheet is reflected from the model and influences the quality of the correlation peak within this region. While the model has a curved surface, it might be that the reflected light-sheet is not aligned with the incoming light-sheet and thus affects the quality of the correlation peak. The highest values of uncertainties can be found next to the ship hull and the free-surface, exceeding the initially determined uncertainties from the uniform flow measurements by a factor of three.

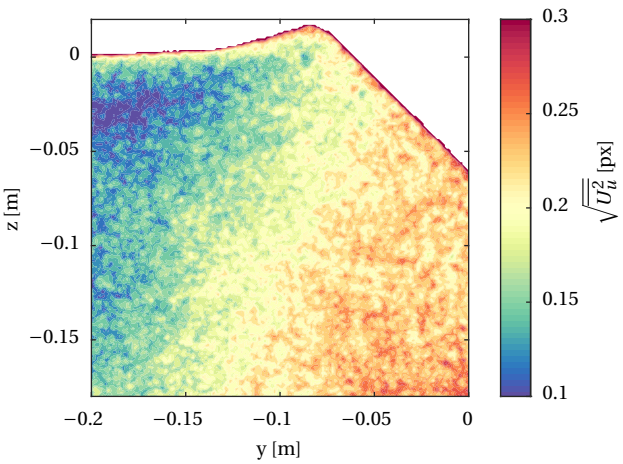

Figure 5.28: Spatial variation of the RMS of the velocity field uncertainty at x=1.4 m.

5.7.1. UNCERTAINTY PROPAGATION

As eventually being interested in the time- and phase-averaged properties of the flow quantities, the uncertainties of the instantaneous velocity fields need to be propagated to those quantities which are of interest. The uncertainties of the mean velocities and Reynolds stresses are determined according to Sciacchitano and Wieneke (2016), as described in Chapter 4. Having obtained the instantaneous uncertainties with the correlation statistics method, the Reynolds normal stresses are again corrected by subtracting the mean-square of these. The final propagation of the uncertainties of the mean velocities and the Reynolds stresses towards the uncertainty of the pressure field is done with Monte Carlo simulations (see Chapter 4). For a reliable determination of the pressure uncertainty, a total of 10.000 realizations is done. Figure 5.29 shows the uncertainties of the mean velocity field magnitude $U_{\overline{|u|}}$ (left) and the result of the uncertainty propagation towards the final pressure field U_{Cp} (right). Both uncertainty distributions are presented with a confidence interval of 95 %. The highest uncertainties can be found close to the ship hull, with maximum values within the spray root of the bow wave. In the far-field, the expanded uncertainty of the time-averaged velocity is approximately $5 \cdot 10^{-3}$ m/s, which is equal to 0.15 % of the carriage velocity. The value increases to $3 \cdot 10^{-2}$ m/s in the spray root, which is equal to 1 % of the carriage velocity. A similar uncertainty distribution can be found for the expanded uncertainty of the pressure coefficient, which is approximately $6 \cdot 10^{-4}$ in the far-field and $6 \cdot 10^{-3}$ close to the ship hull. The reported values are equal to 0.5 % and 5.5 % of the peak pressure, detected in the spray root.

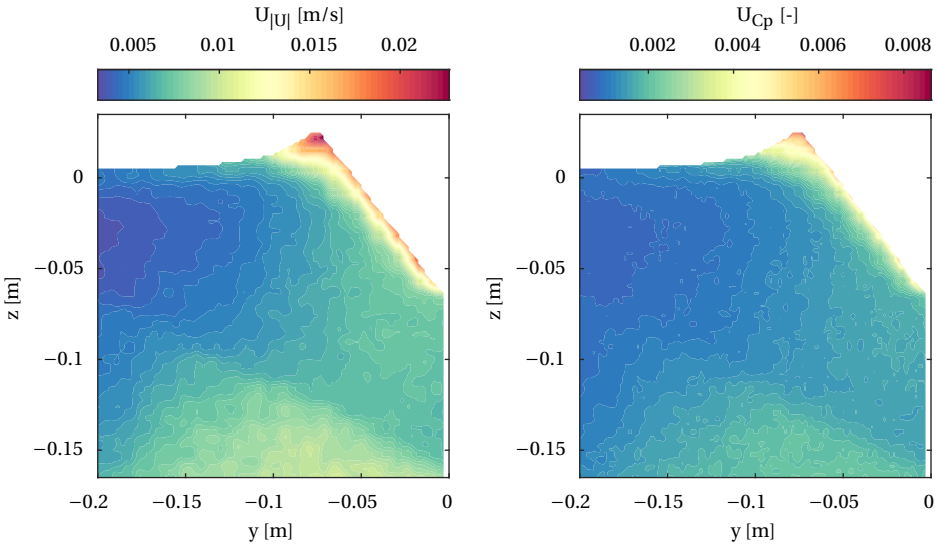

Figure 5.29: Spatial variation of the uncertainty of the mean velocity magnitude (left) and the uncertainty of the pressure coefficient (right) at x=1.4 m.

5.8. DISCUSSION AND COMPARISON OF EXPERIMENTAL AND NUMERICAL RESULTS

For the final evaluation of the quality of the measured pressure fields, results from the PIV measurements are compared to the previously obtained numerical results. While the pressure field is reconstructed from the measured velocities with the help of the Poisson equation, these have to be compared first, to make sure that the experimental conditions match with those from numerical simulations. The reconstructed pressure fields and force distributions on the ship hull are compared.

5.8.1. MULTI-PLANE PIV MEASUREMENTS

VELOCITY FIELDS

As described in Section 5.3, multi-plane PIV measurements were performed in the bow region of the ship model to obtain a volumetric description of the flow field. For these measurements, the ship is towed at 3.32 m/s, and the velocity field obtained in a total of 60 measurement planes starting at x=1.2 m, which were perpendicular to the main flow direction. After a first impression of the measurement results has been given in Section 5.5, Figure 5.30 shows a comparison of the measured velocity field (right) with numerical results (left) at two selected planes located at x=1.4 m and x=1.5 m. Their position along ship is indicated in Figure 5.30 (top). While the overall velocity distribution matches well

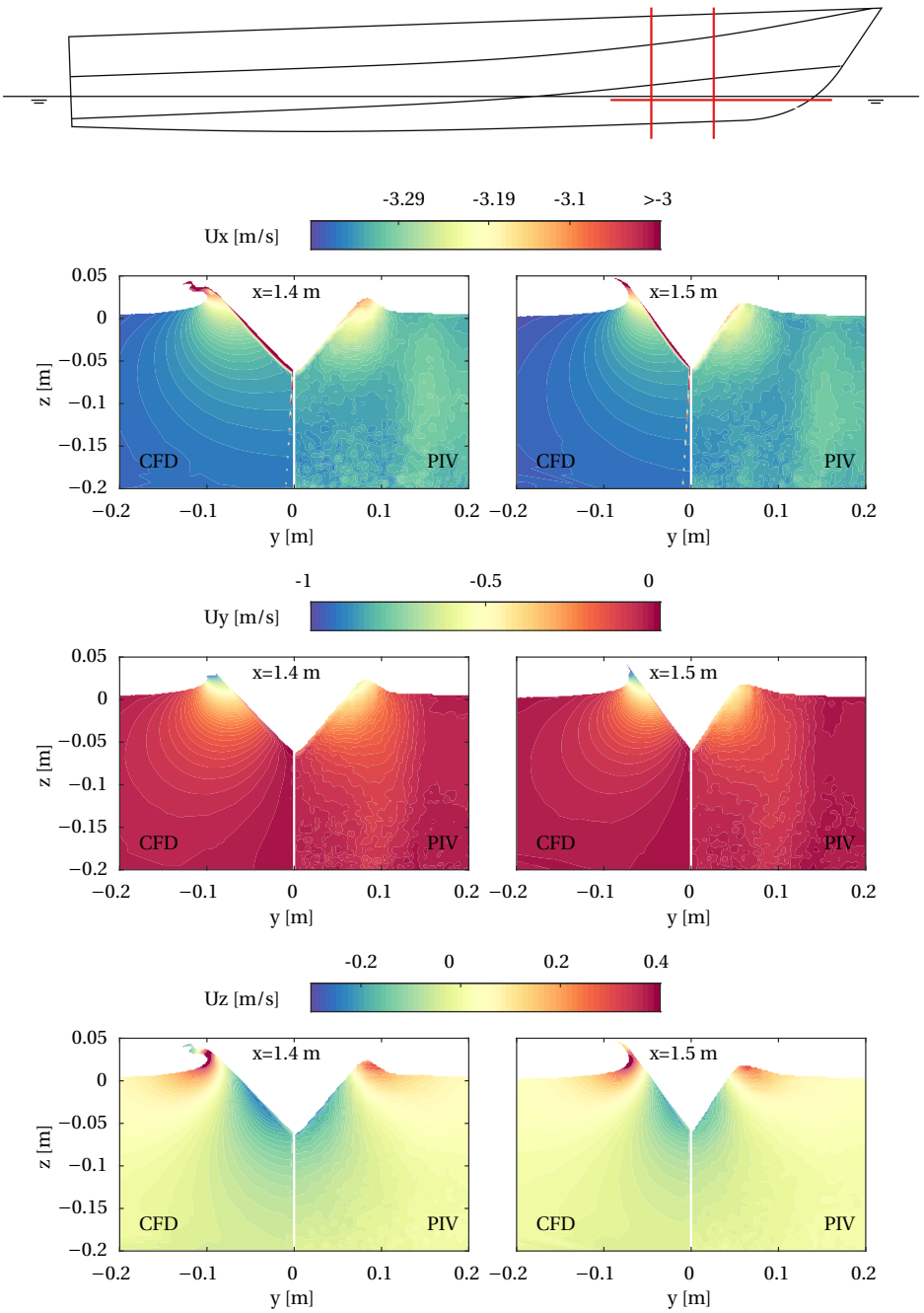

Figure 5.30: Velocity field components at x=1.4 m and x=1.5 m. Comparison of PIV measurements with numerical results

for all three velocity components, significant local differences can be found. One of the most significant differences can be found by looking at the out-of-plane velocity field. While the numerical solution resolves the flow within the boundary layer, it is not resolved in the PIV measurement. The reason for this is twofold. As for a successful pressure reconstruction, the domain needs to be sufficiently large, the field of view is increased to approximately 0.25 by 0.25 meters. With a sensor size of 2048 by 2048 pixels and an interrogation window size of 24 pixels with an overlap of 75 %, the spatial resolution is approximately 1 mm. This is about the same order of magnitude as the boundary layer within this region. Furthermore, reflections on the model surface did not allow measurements in the direct vicinity of the surface. Further discrepancies can be found within the spray root region and the jet, which is formed on the ship hull. With the current setup, it is not possible to obtain optical access to this region. Due to the limited spatial resolution, also the high velocity gradient within this region is slightly under resolved.

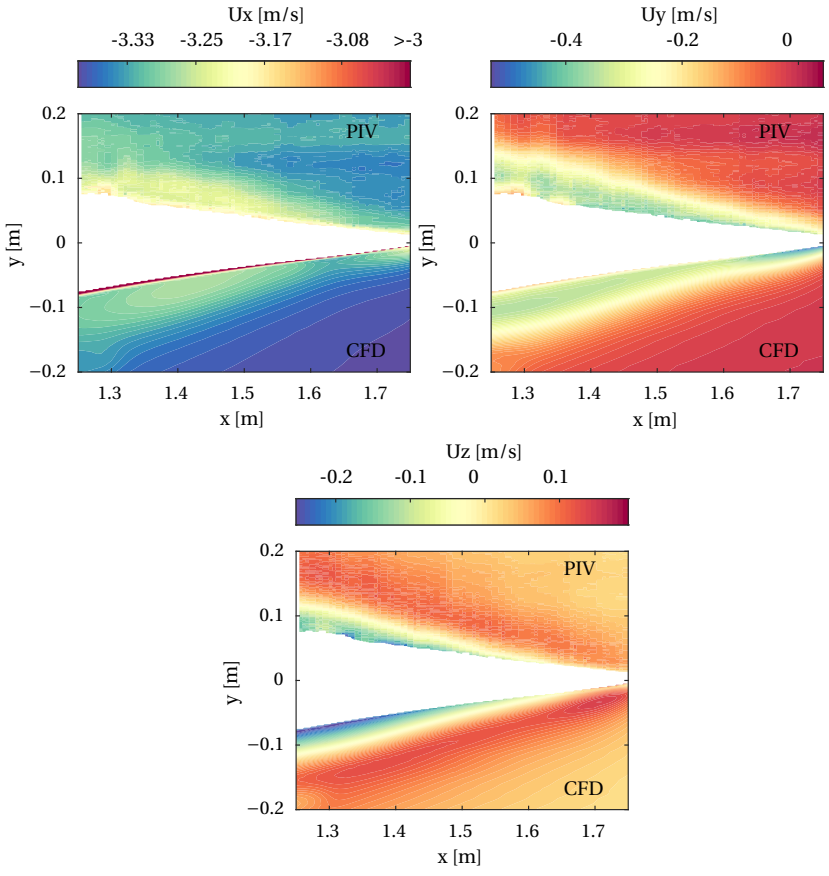

Figure 5.31: Velocity field components at z=-0.01 m. Comparison of PIV measurements with numerical results

While the volumetric representation of the velocity field is generated only from vertical measurement planes which are perpendicular to the main flow direction, a horizontal slice of the domain is used to examine the continuity of the velocity field across the measurement planes. The position of the slice is at z=-0.01 m and indicated in Figure 5.30 (top). Figure 5.31 shows a comparison between measurements (top) and numerical results (bottom) for all three velocity components. For all three velocity components, a smooth velocity field can be observed along the x-direction. The overall comparison between both techniques again shows good agreement, with the PIV technique capturing the main features of the flow. However, as already noticed in Figure 5.30, the near-wall flow cannot be captured with the PIV technique as a result of a compromise between spatial resolution and field of view.

PRESSURE FIELDS

With the volumetric description of the velocity field, the dynamic pressure field is reconstructed in the bow region of the ship model by solving the Poisson equation. The quality of the reconstructed pressure field is observed in Figure 5.32 by comparison with the numerical results. The pressure field is analyzed in two horizontal planes at z=-0.01 m and z=-0.03 m and 4 vertical slices with equal distance between x=1.4 m and 1.6 m. The position of these planes is indicated in Figure 5.32 (top). Comparing the pressure field within the two horizontal slices with numerical results shows that the main characteristics of the hydrodynamic pressure field are well reproduced with the pressure PIV technique. The high pressure area within the bow wave, as well as the stagnation region in the bow, can be found in the measurement results. Despite the absence of the boundary layer in the PIV measurements, good agreement between numerical and experimental results is also found close to the wall within the bow wave. However, close to the bow, the experimentally obtained pressure is lower than the numerically obtained pressure. Here, the high velocity gradient cannot be fully resolved by the PIV measurements, which have a limited spatial resolution. The pressure field in the vertical slices also shows a good overall agreement between both methods. The limited optical access to the region of the jet, which is formed on the ship hull and the limited spatial resolution result in an under prediction of the pressure peak within the spray root of the bow wave. To obtain the distribution of the hydrodynamic lift forces on the bow, the hydrodynamic pressures are interpolated to the ship hull. In Figure 5.33 (top), the bow segment is highlighted over which the force distribution is eventually calculated. For the force integration, the region is split into sections of 0.01 m, which is equal to the spacing of the PIV measurement plane. The resulting sectional forces are presented in both intermediate plots of Figure 5.33. The first plot shows the numerically obtained distribution of sectional lift forces over the whole length together with the sectional lift forces from the PIV measurements. It becomes visible, that despite the effort of obtaining the velocity fields in a total of 60

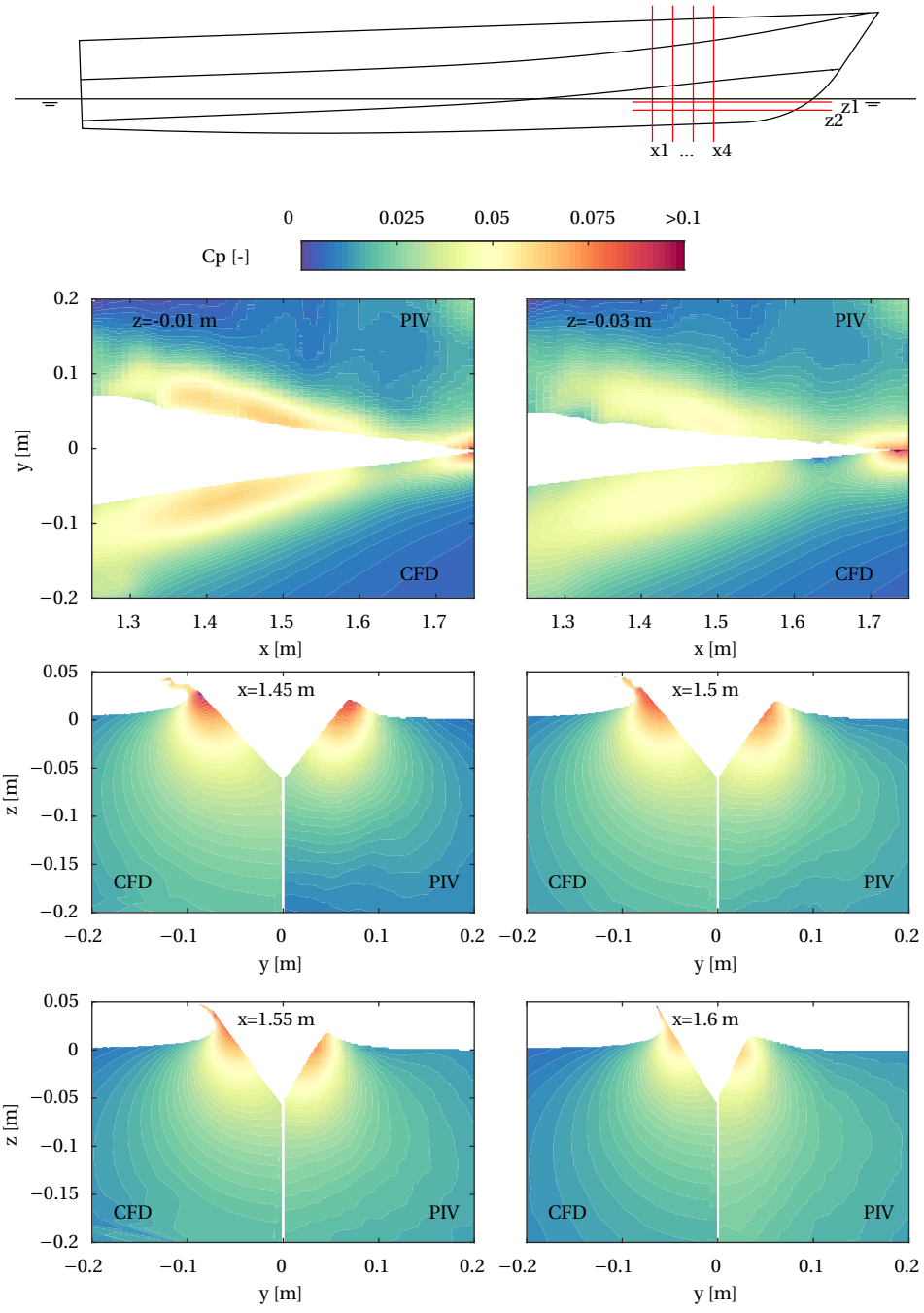

Figure 5.32: Comparison of the reconstructed pressures with numerical results at selected slices of the measurement domain

measurement planes the force distribution of only a relatively small part of the ship model has been obtained. In this region, however, the hydrodynamic lift distribution matches well with the numerical simulations. A more detailed picture of the sectional lift force distribution is given in the second plot. The integration of the sectional forces leads to the total hydrodynamic lift force in the bow region. Here, the experimentally obtained force is approximately 4 % smaller compared to the CFD results. By looking at the distribution of the sectional forces, largest differences are found between x= 1.35 m and x = 1.5 m. As already seen in Figure 5.32 in this region, the flow field within the bow wave is not fully captured but cut off above the spray root. Furthermore, the pressure peak in this region was slightly under predicted. Within the bow wave, the maximum local deviation of the sectional lift force is 11%.

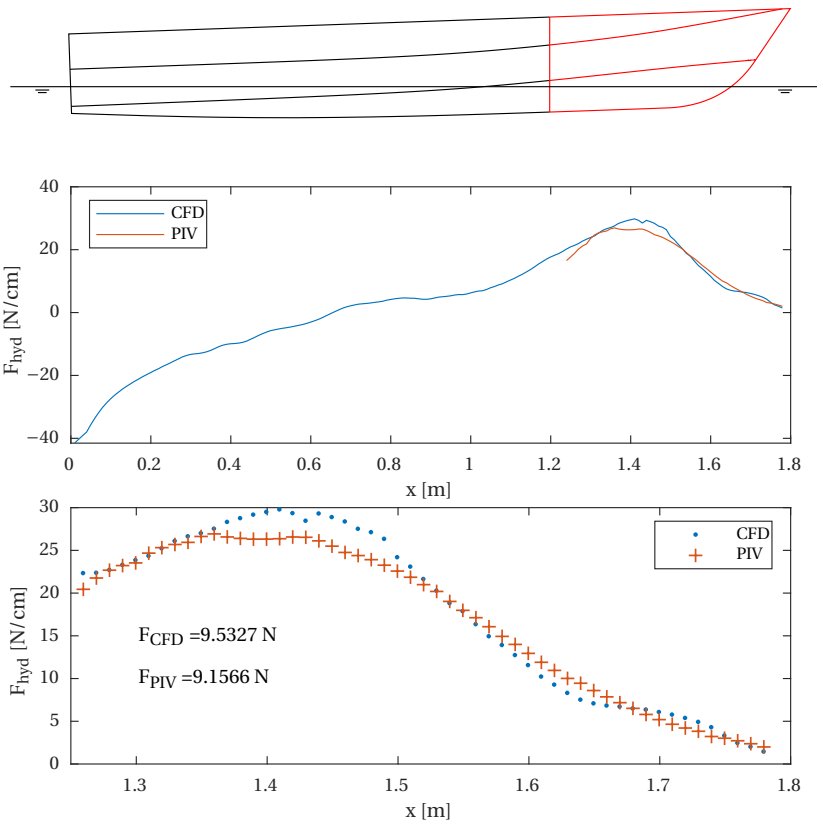

Figure 5.33: Comparison of the force distribution on the ship hull obtained by pressure PIV experiments with numerical results

5.8.2. OSCILLATION TESTS

VELOCITY FIELDS

Oscillation tests are performed at a lower carriage speed of 2.54 m/s, which is equal to Fr_L 0.6, and PIV recordings are obtained in three successive planes perpendicular to the main flow direction at x=1.35 m. A first impression of the velocity field and the corresponding pressure field during the downward motion of the ship is given in Section 5.5, where the pressure increase is found to be proportional to the horizontal velocity amplitude. Figure 5.34 and 5.35 compare the velocity fields obtained for two different test cases. While the oscillation frequency is kept constant at 1 Hz for a temporal resolution of 50 vector fields per oscillation cycle, the oscillation amplitude is varied between 0.017 m and 0.035 m. Time traces of the ship's vertical position and the corresponding vertical velocity are shown at the top of Figure 5.34 and 5.35. The doubling of the oscillation amplitude also doubles the maximum vertical oscillation velocity. Both figures compare the experimentally obtained velocity fields with numerical results for two selected time instants during the downward moving phase. The two time instances are at 0.1 s within the downward acceleration phase and at 0.26 s where the model has reached its maximum downward velocity with the chine being immersed in both cases. The comparison with numerical results shows good overall agreement at both time instances. However, as noticed during the multi-plane PIV measurements, the flow close to the ship hull cannot be resolved because of reflections, which did not allow measurements right at the wall and the low spatial resolution. The latter and the limited optical access to the jet region, which forms on the ship hull, also result in larger differences in this region. The largest differences for both cases can be found at 0.26 s close to the immersed chines. As the forward speed of the model is reduced for the oscillation tests from 3.32 m/s to 2.54 m/s, by using the same maximum pixel displacement, the lower dynamic range of the velocities results in a higher resolution of this. However, while the numerical simulations capture the local acceleration of the flow around the sharp edge of the chine, this is not sufficiently captured by the PIV measurements.

PRESSURE FIELDS

The reconstructed pressure fields for both cases are presented in Figure 5.36 and 5.37 where they are compared to the numerical results for six selected time-steps during the downward motion of the ship hull. Having seen a good agreement of both methods for velocity fields, differences become more pronounced in the pressure fields. In both, the numerical simulations, as well as the experiments, the high pressure area increases during the downward motion. As far as it can be observed from the six selected time steps, the pressure peak in the numerical results coincides with the immersion of the chine, whereas it is slightly shifted to a later time instance in the PIV measurements. Further is the pressure peak in the experimental results not at the hull-water intersection,

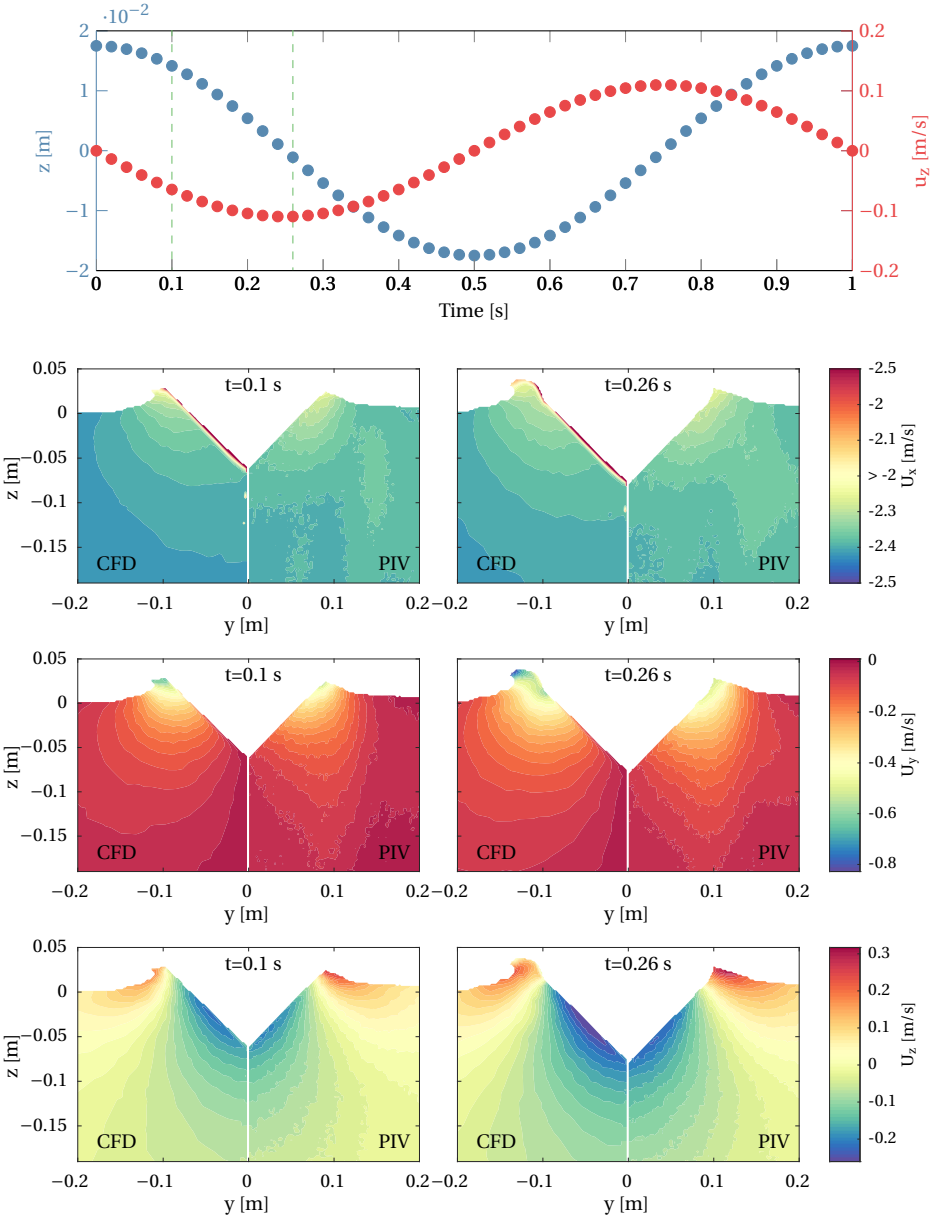

Figure 5.34: Distribution of phase-averaged velocity components at two selected time instants during the downward motion of the ship model, performing oscillatory motions at f=1Hz with an amplitude of a=0.0175m. Comparison of experimental with numerical results.

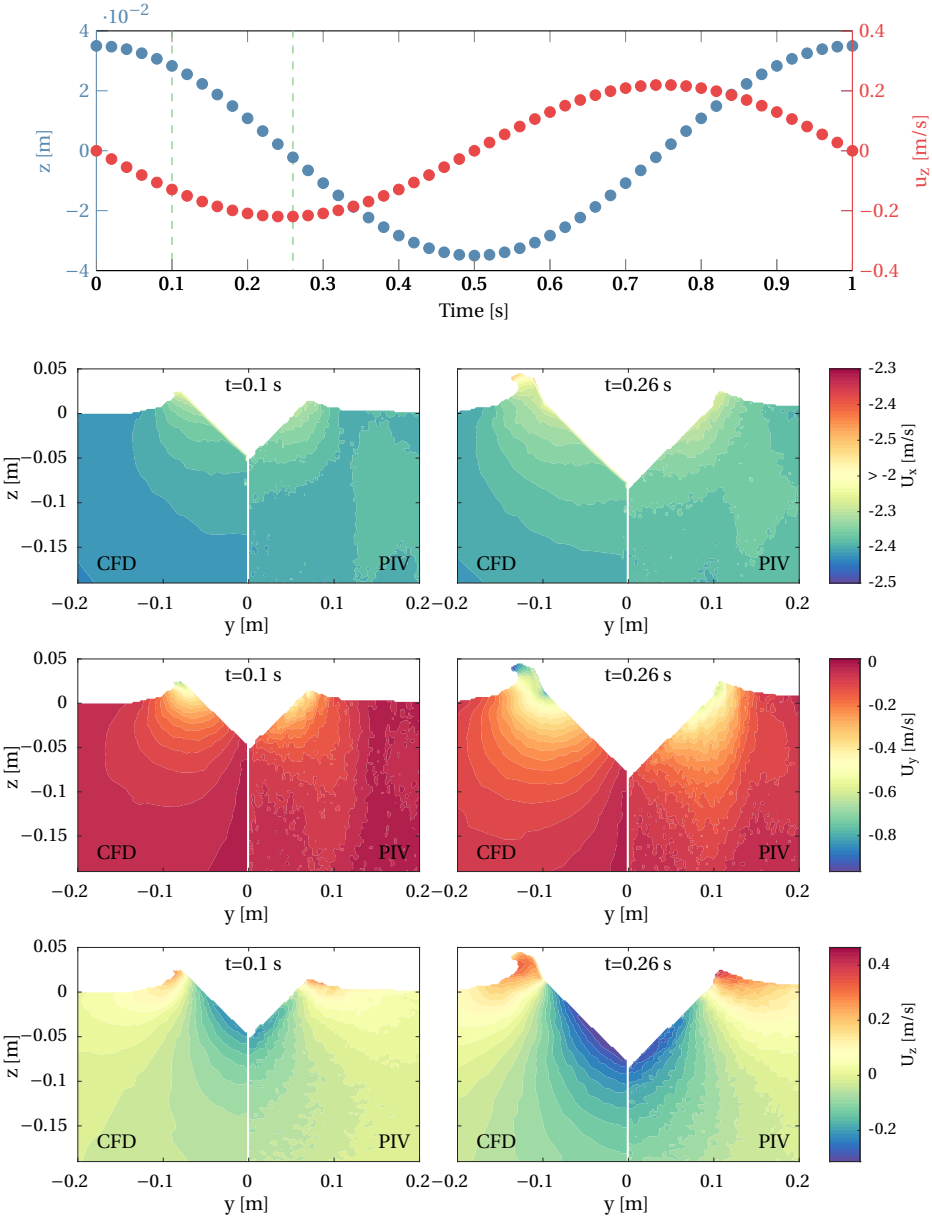

Figure 5.35: Distribution of phase-averaged velocity components at two selected time instants during the downward motion of the ship model, performing oscillatory motions at f=1Hz with an amplitude of a=0.035m. Comparison of experimental with numerical results.

as expected from the numerical simulation, but further shifted downwards. As already seen in the velocity field comparison, the numerical simulations are able to resolve the small local acceleration region above the edge of the chine. The effect of this can also be observed in the numerically observed pressure fields, starting from 0.16 s for the small amplitude and 0.22 s for the larger amplitude. However, as already noticed in the velocity fields, this effect is not captured with the experimental method.

SURFACE PRESSURE AND INTEGRATED FORCES

A better picture of the temporal evolution of the pressure is given in Figures 5.38 and 5.39, which show the temporal evolution of the pressure distribution on the hull for one oscillation cycle at the measurement section at x=1.35 m. While the bottom line indicates the position of the keel, the upper line shows the position of the chine. In both cases, the general behavior of the pressure field is well reproduced with the PIV measurements, showing a pressure increase during the downward motion and a low-pressure area during the upward motion. However, what has already been noticed in the sectional pressure field plots becomes more clear within the temporal evolution of the surface pressure distribution. The CFD results show a well defined pressure peak when the chine becomes immersed, which is at 0.1 s in Figure 5.38 and at 0.15 s in Figure 5.39. Once immersed, the peak pressure at the chine is reduced. The pressure peak, reconstructed from PIV experiments, is slightly shifted within time and space. Instead of capturing the high impact pressure on the chine, the high-pressure region is stretched over multiple time steps. Also captured in the CFD result, but not visible within the measured pressure field, is the pressure drop above the chine due to the acceleration of the flow in this region. The position of the low-pressure area during the upward motion is well predicted at approximately 0.6 s. However, both PIV measurements indicate lower dynamic pressures compared to the numerical results.

Figure 5.38 and 5.39 (bottom), both show the time traces of the sectional forces obtained from the integration of the hydrodynamic pressure. While for the multi-plane PIV measurements with a captive model in calm water, good agreement was found between CFD and experimental results, significant differences are found for the oscillation tests. In the numerical simulation, the hydrodynamic force rapidly increases until the immersion of the chines. The experimental results, however, show a slow increase of forces, which is in phase with the velocity field. While the amplitude of the maximum force matches well with the numerical results for the higher oscillation amplitude, it is over predicted for the low amplitude test case.

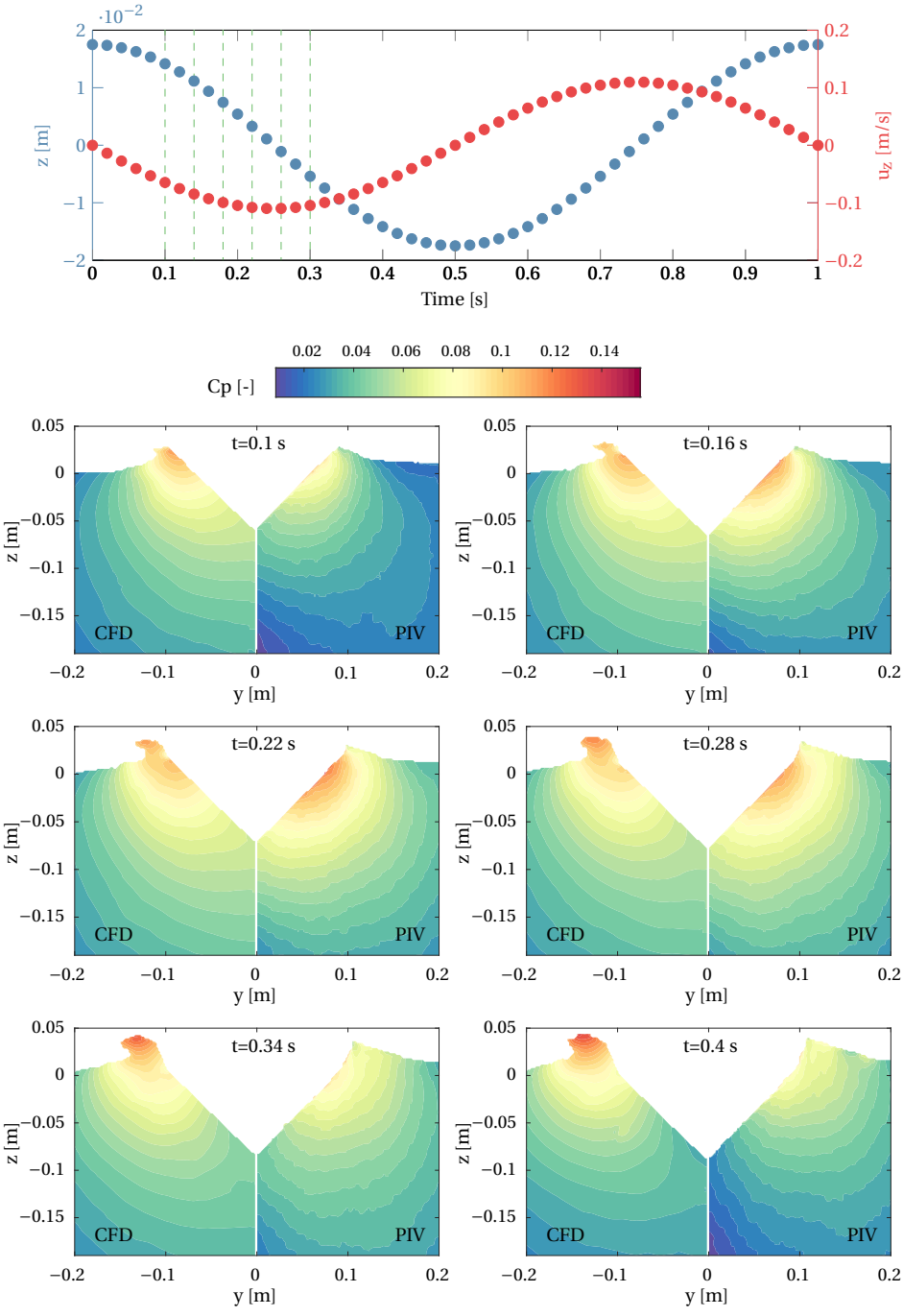

Figure 5.36: Distribution of phase-averaged pressure fields at six selected time instants during the downward motion of the ship model, performing oscillatory motions at f=1Hz with an amplitude of a=0.0175m. Comparison of experimental with numerical results.

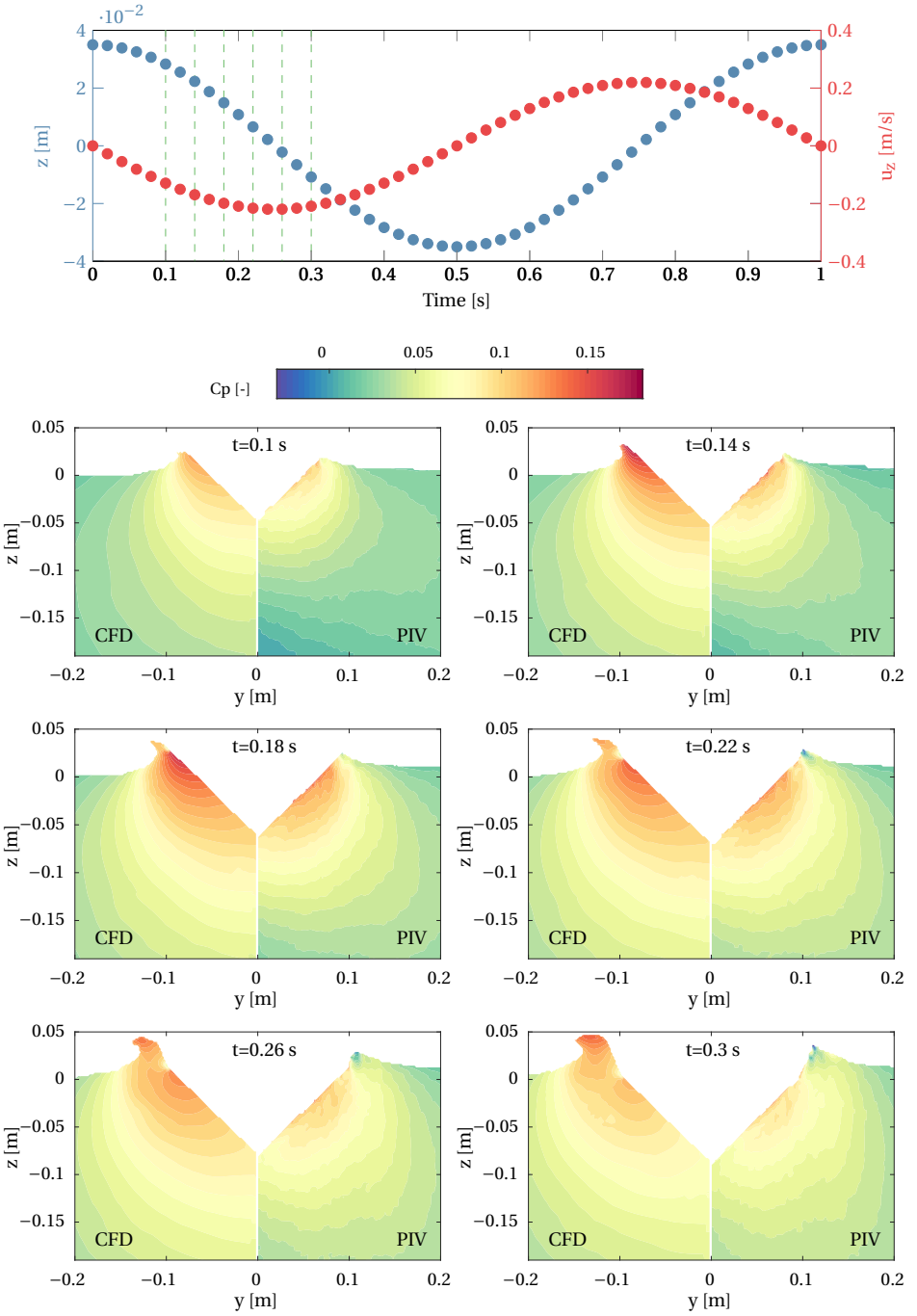

Figure 5.37: Distribution of phase-averaged pressure fields at six selected time instants during the downward motion of the ship model, performing oscillatory motions at f=1Hz with an amplitude of a=0.035m. Comparison of experimental with numerical results.

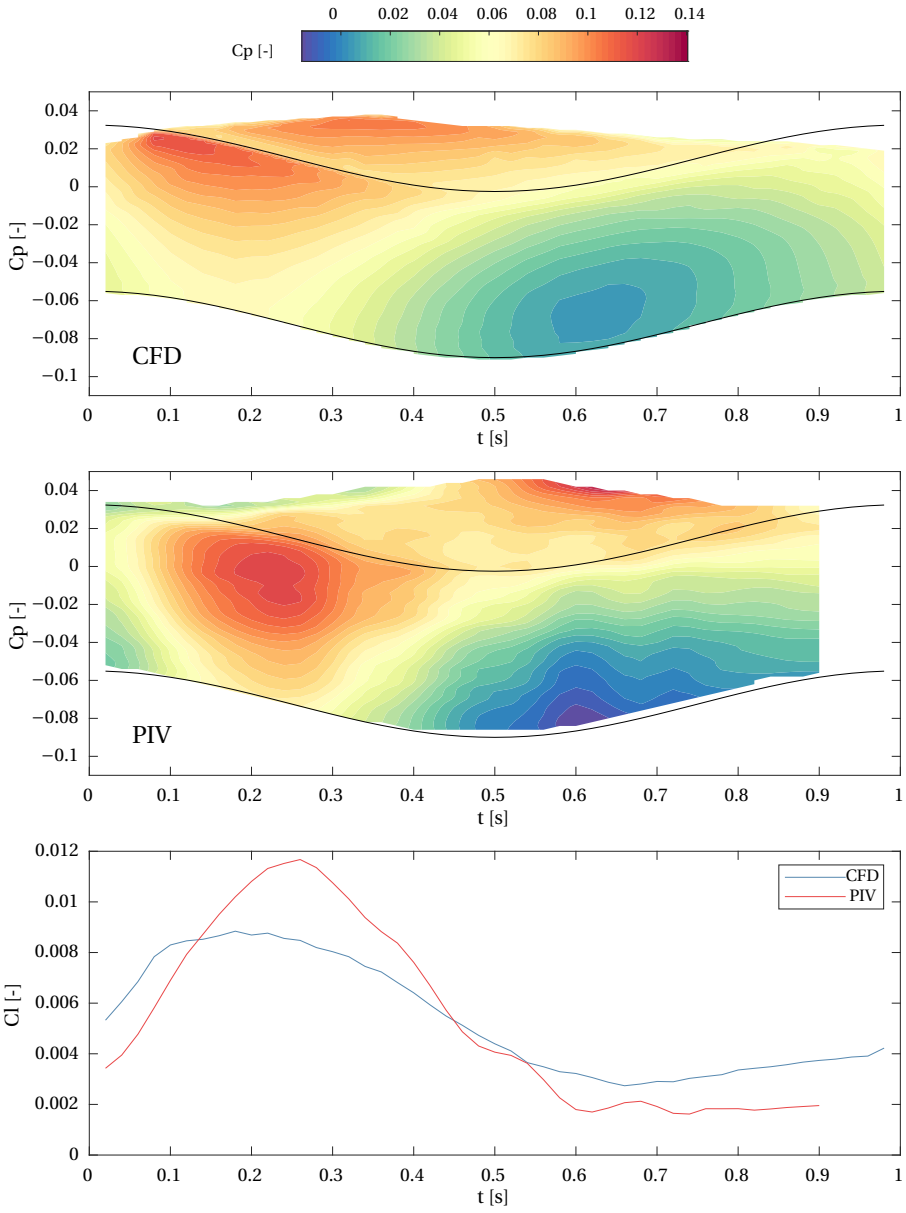

Figure 5.38: Temporal evolution of the pressure distribution and lift coefficient on the ship hull at x=1.35 m for f=1Hz and a=0.0175 m. Comparison of experimental with numerical results.

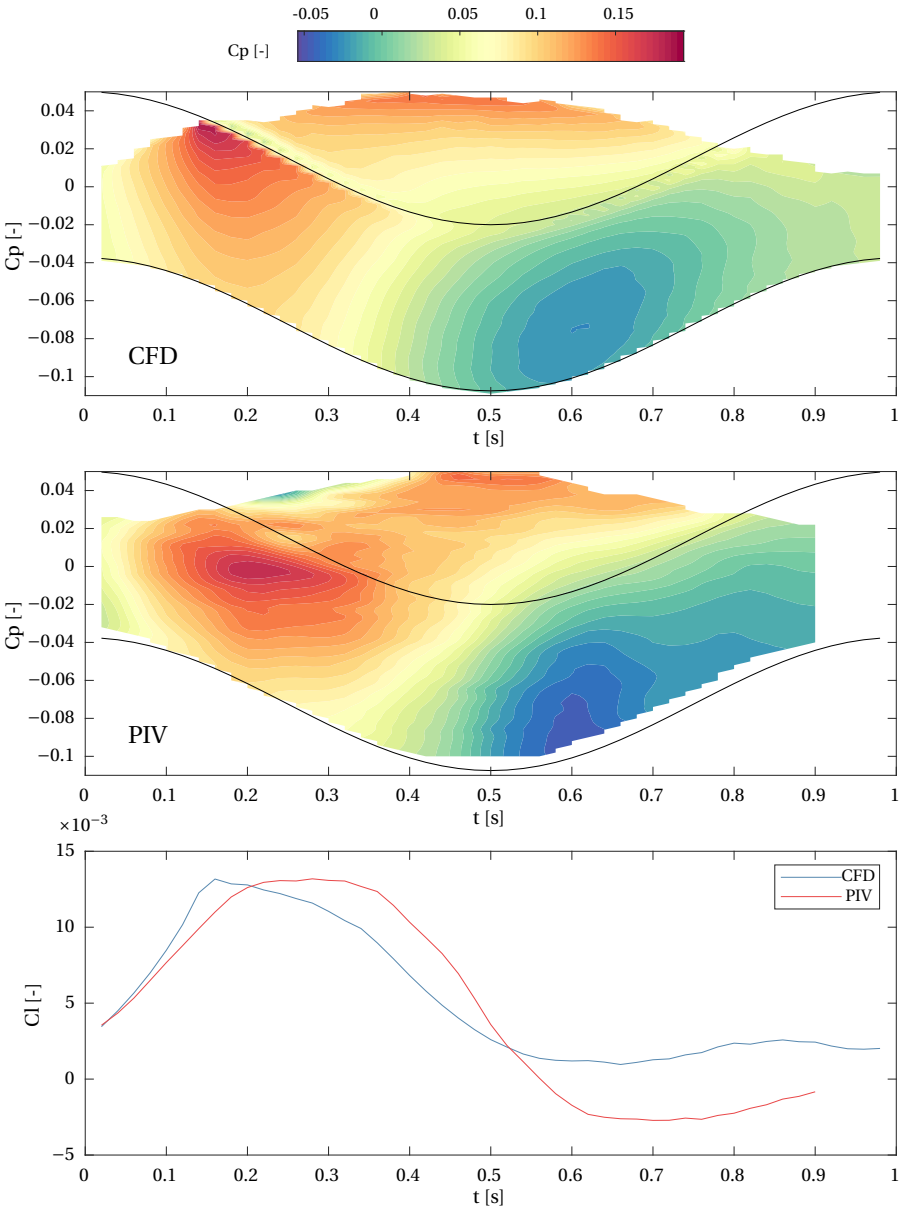

Figure 5.39: Temporal evolution of the pressure distribution and lift coefficient on the ship hull at x=1.35 m for f=1Hz and a=0.035 m. Comparison of experimental with numerical results.

5.9. DISCUSSION

For further understanding of the hydrodynamics of fast ships and the validation of numerical codes, De Jong (2011) expressed the need for an experimental technique that accurately captures the pressure distribution in the flow field around these types of ships. After a first successful application of the pressure PIV technique, presented in Chapter 4, the technique is used to reconstruct the hydrodynamic pressure distribution in the bow region of a fast ship. The ship model, used for the investigation in Chapter 4, has a simple box-shaped aft-section which is made from perspex. This enabled measurements close to the wall, and masking out the ship bottom was a straight forward procedure. Furthermore, the main flow direction is aligned with the laser-sheet, which resulted in a high resolution of the dynamic range. However, during the measurements presented in this chapter, the measurement plane is oriented perpendicular to the main flow direction. The measurements are aimed at capturing the flow field close to the ship hull as well as in the flow field, to create the domain for the pressure reconstruction. This significantly reduces the dynamic range, due to the high carriage velocities and the finite laser-sheet thickness, which limited the out-of-plane particle displacement. Despite the large stereo-angle, only a particle displacement of seven pixels could be obtained for the out-of-plane component. While the in-plane velocities were significantly smaller, the uncertainty of the instantaneous velocities significantly increased for these components.

During the test-case presented in Chapter 4, the measurement area is illuminated through the perspex bottom of the ship. This results in only little reflections influencing the measurement region, and the flow field can also be obtained close to the ship hull. However, in the present case, the model is illuminated from under-water through a submerged laser-sheet optic. Despite painting the model black, reflections occur on the ship hull. This makes a measurement in the direct vicinity of the model difficult. The high-intensity region is enlarged due to the thick light-sheet, which is meant to increase the dynamic range of the out-of-plane component.

The pressure reconstruction asks for an accurate definition of the domain boundaries. To correctly apply the boundary conditions, the ship hull and the water surface have to be identified and masked out from the images. Reflections of the ship hull make the identification of this a straight forward procedure. However, the identification of the free-surface proved to be a non-trivial task. While the identification of the instantaneous free-surface position was not possible, the time- and phase-averaged free-surface is reconstructed with adequate time-filtering of the images. The large amount of measurement planes for the volumetric velocity field reconstruction makes automation of the procedure necessary.

The velocity fields and the reconstructed pressure fields are finally compared to numerical results from RANS simulations. For the velocity fields outside of the boundary

layer, good agreement is found. However, more substantial differences are found close to the ship hull. Due to the reflections and the limited resolution of the dynamic range, the outer boundary layer cannot be resolved. Additionally, the limited optical access to the spray region of the bow wave made velocity measurements in this region impossible. Despite the missing boundary layer in the measured velocity fields, the pressure fields of the calm-water tests show a good agreement with the numerical results. An interpolation of the obtained pressure field onto the ship hull shows that the method is also able to reconstruct the load distribution on the ship hull. The velocity fields obtained during forced oscillation tests, also match well with numerical simulations. However, the reconstructed pressures from these tests show a less good agreement with numerical results. While the general behavior of the pressure field is still captured, the location of the pressure peak and its amplitude are predicted inaccurately with this method. One reason for this might be the under-resolved flow close to the ship hull and the pressure boundary condition, where the acceleration is obtained from the motion of the ship.

6

CONCLUSION

To improve the understanding of the hydrodynamics of fast ships, the performance of a towed underwater PIV system is evaluated for measuring the flow field around these types of ships. At high velocities, the hydrodynamic pressure distribution plays an important role and influences the performance of the ship. While traditional pressure measurement techniques often suffer from limited spatial resolution, the obtained velocity field is used for a reconstruction of the pressure field. The potential of the technique is evaluated by means of two practical applications, for a reconstruction of the pressure in the flow field, as well as on the ship hull.

6.1. PIV AT HIGH CARRIAGE SPEEDS

With the PIV technique, being an optical measurement technique, the quality of the obtained velocity fields is highly dependent on an initial calibration, that defines the mapping function between the observed flow region and the image plane. Furthermore, it has to be assured that the observed particles are visible in both image frames, which are used for correlation. Following this, structural vibrations of the carriage at high speeds and particle-loss, due to high out-of-plane velocity components, are identified to be the most critical aspects in stereo-PIV applications for the study of high-speed craft hydrodynamics.

6.1.1. STRUCTURAL VIBRATIONS

By means of PIV measurements in the transom region of a planing hull, it is shown that depending on the towing carriage speed, structural vibrations occur, that increase with

carriage speed. While the setup did not allow for a rigid connection of all PIV system components, i.e., laser and camera sections, the structural vibrations are found to result in a time-dependent displacement of the optical components. This results in a mismatch of the images from both cameras, known as disparity. Performing measurements in the range between 1-5 m/s this disparity is found to significantly increase with towing carriage speeds. Resulting from this, the 3d velocity vectors, which are calculated from 2d vectors of both cameras in a stereo-PIV system, are not correctly calculated, as velocity information from different positions of the flow field is used for the 3d vector reconstruction. The distance between these positions is called the registration error, and it is only visible in flows with gradients. While the registration error cannot be determined, as the gradient in the flow is usually not known, the disparity can be assessed and used for a correction of the initial calibration. While the disparity correction only corrects for the motion of the cameras with respect to each other, it has to be used in combination with a feature-based image correction to correct for any motion with respect to the investigated object. The inter-camera correction increases the measurement accuracy, and the motion correction with respect to the object reduces the uncertainty of the spatial location of the measured property. This is especially important when considering a statistical description of the flow in a vibrating environment. Vibrations of the setup should be suppressed already with the design of the setup. Especially the inter-camera motion is suppressed by placing both cameras in one rigid torpedo.

6.1.2. OUT-OF-PLANE FLOW

In towing tank experiments, with stereo-PIV systems, the light-sheet plane is often chosen to be perpendicular to the main flow direction, often for the reason of capturing local flow structures, such as vortices. Especially when the flow close to the hull is observed, the dynamic range automatically increases with the carriage speed, to capture as well the flow close to the hull, that approaches zero and the free-stream flow. The finite thickness of the light-sheet limits the out-of-plane particle displacement in between two recorded images and thus significantly reduces the resolution of the given dynamic range. Given a constant thickness of the light-sheet, the resolution linearly reduces with increasing carriage speed and dynamic range. Often seen in towing tank applications is an asymmetric setup, with the laser-sheet in front and the cameras observing the flow from one side of the light-sheet. While in flows with small out-of-plane velocities accurate stereo PIV measurements can be already obtained at smaller stereo-angles, at high-speed, large stereo angles are favored, to increase the resolution of the out-of-plane motion. Whenever the setup allows an orientation of the light-sheet that is aligned with the main flow direction, the largest possible resolution of the dynamic range can be established.

6.2. PRESSURE MEASUREMENT WITH PIV IN TOWING TANKS

In combination with the solution of the pressure Poisson equation, the PIV technique is tested as an alternative to existing pressure measurement techniques, which often suffer from low spatial resolution and intrusiveness. The reconstruction of the velocity field and its corresponding pressure field in front of an interceptor shows, that pressure measurements can be obtained in regions where high spatial resolution is necessary but cannot be provided by traditional techniques. Being interested in time- or phase-averaged pressure fields multi-plane PIV measurements can extend the observed region, to a volume. This extends the capability of the method to capture the pressure field in three-dimensional flows, where the out-of-plane velocity gradient has to be considered when solving the Poisson equation. Limitations of the method become clearer during pressure PIV measurements in the bow region of a fast ship. The method requires optical access to the measurement region and good image quality of the particles. Limited optical access makes a measurement in the spray region of the bow wave impossible. Furthermore, reflections from the laser-sheet prevent a measurement close to the hull surface. While the solution of the Poisson equation is dependent on adequate boundary conditions, a clear identification of boundaries is important. These can be the ship-hull, but also the free-surface. The identification of these is shown to be a non-trivial task. Especially the free-surface cannot always be identified, which asks for intensive post-processing. However, for the observed test-cases, the time-averaged flow in front of an interceptor and the time-averaged flow in the bow region good results are obtained, and the reconstructed volumetric pressure fields are in good agreement with numerical simulations. Next to the volumetric pressure fields, also the planar, phase-averaged pressure field is reconstructed from PIV measurements in three successive planes, next to an oscillating ship model. While the general flow behavior is well captured, larger deviations are found in the pressure fields when being compared to results from numerical simulations. With the studied flow being relatively complex, for a further investigation, a simpler test case is needed for a detailed evaluation of the pressure reconstruction with an oscillating ship.

6.2.1. PRESSURE PIV FOR HIGH-SPEED CRAFT HYDRODYNAMICS

The studies, conducted in this thesis can be seen as a proof of concept for the application of the pressure PIV technique in towing tank environments. It is shown, that the technique can give valuable insights into the hydrodynamics of fast ships, where hydrodynamic pressures play an important role for the understanding and prediction of the ship's performance. While further evaluation and testing is necessary to make it an established technique, the conducted studies show, that in terms of spatial resolution and non-intrusiveness, the PIV technique poses an interesting alternative to traditional meth-

ods, such as Pitot-tubes and pressure sensors. Especially where traditional techniques cannot be applied, either due to the limited possibilities for fitting sensors or where their intrusiveness distorts the measurement result, the pressure PIV technique can be used, given that optical access to the observed region is provided. Under these conditions, the technique also enables the reconstruction of sectional pressure- and force-distributions on the ship hull.

6.3. OUTLOOK AND FUTURE RECOMMENDATIONS

Limitations of the planar stereo-PIV system for the usage of three-dimensional time- and phase-averaged flows are overcome by using multi-plane measurements for the reconstruction of the volumetric velocity and pressure fields. However, the multi-plane technique limits the application to ensemble-averaged consideration of the observed problem. Especially, the reconstruction of the out-of-plane velocity gradients from different measurement planes can lead to additional uncertainties. Furthermore, it is shown that in flows with high out-of-plane velocities, the planar character of the technique results in a limitation concerning the resolution of the dynamic range. For further improvement and an extension of the technique for the observation of unsteady phenomena in three-dimensional flows, the usage of a tomographic PIV system or tomographic particle tracking velocimetry (PTV) system may be considered. With a volumetric illumination and usually four cameras, the instantaneous flow field in a volume can be obtained. However, next to a more complex test setup, these systems ask for higher laser powers, to achieve an exposure level which is comparable to planar recordings (Adrian and Westerweel (2011)). While the energy density of the light-sheet reduces with increased thickness, at the same time, a smaller aperture is needed to achieve a larger depth of field. The tomographic PIV technique has been first applied in a towing tank environment by Egeberg et al. (2014) for the investigation of shedding vortices from a ship hull. Recently, a compact tomographic underwater probe has been released by LaVision (2019), which is optimized for time-resolved tomographic PTV in towing tank environments. The pre-calibrated probe can observe the flow field in a volumetric region of approximately 300 x 200 x 150 mm^3. Figure 6.1 shows the mini-shaker underwater probe and an example of the recorded flow field.

While the small footprint of the probe asks for small stand-off distances, a larger, modular torpedo-based tomographic system would allow more flexibility. As seen for planar PIV measurements, the application of the technique close to the ship-hull and the free-surface presumes accurate masking and identification of these surfaces, especially, when a reconstruction of the pressure on one of these is of interest. For the application in a tomographic setup, thus, accurate identification of the three-dimensional ship hull and the water-surface would be necessary.

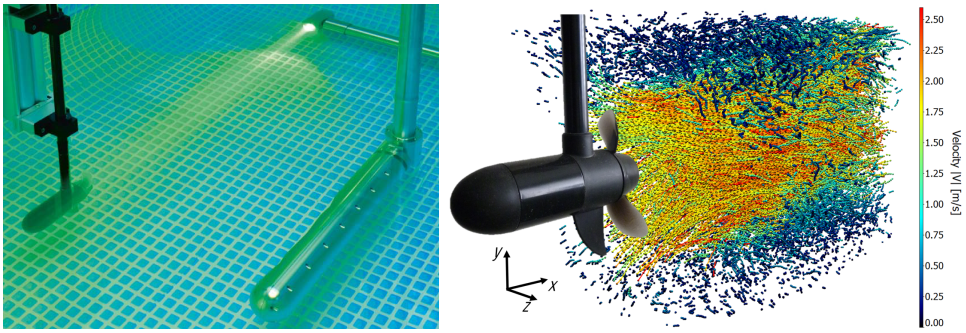

Figure 6.1: Experimental setup for the measurement of the volumetric velocity field in the wake of a propeller with the mini-shaker probe (left) and an example of the obtained instantaneous velocity field (right)(LaVision (2019))

REFERENCES

R. J. Adrian and J. Westerweel. *Particle image velocimetry*. Cambridge University Press, 2011.

T. Albrecht, V. del Campo, T. Weier, and G. Gerbeth. Comparison of PIV-Based Methods for Airfoil Loads Evaluation. *Symposium on Applications of Laser Techniques to Fluid Mechanics*, (July 2015):9–12, 2012.

P. Anschau and K. Mach. Application of a Stereo PIV System for Investigations of Flow Fields in Towing Tank and Cavitation Tunnel. *Archives of Civil and Mechanical Engineering*, 7(3):5–17, 2012. ISSN 16449665. doi: 10.1016/s1644-9665(12)60009-0.

A. Ashworth Briggs, A. Fleming, J. Duffy, and J. R. Binns. Tracking the vortex core from a surface-piercing flat plate by particle image velocimetry and numerical simulation. *Proceedings of the Institution of Mechanical Engineers Part M: Journal of Engineering for the Maritime Environment*, 2018. ISSN 20413084. doi: 10.1177/1475090218776202.

I. Azijli and R. P. Dwight. Solenoidal filtering of volumetric velocity measurements using Gaussian process regression. *Experiments in Fluids*, 56(11):1–18, 2015. ISSN 07234864. doi: 10.1007/s00348-015-2067-7.

I. Azijli, A. Sciacchitano, D. Ragni, A. Palha, and R. P. Dwight. A posteriori uncertainty quantification of PIV-based pressure data. *Experiments in Fluids*, 57(5):1–15, 2016. ISSN 07234864. doi: 10.1007/s00348-016-2159-z.

J. J. Blok and W. Beukelman. The high speed displacement hull forms - seakeeping characteristics. *Transactions Society of Naval Architects and Marine Engineers*, 92: 125–150, 1984.

A. Boomsma, S. Bhattacharya, D. Troolin, S. Pothos, and P. Vlachos. A comparative experimental evaluation of uncertainty estimation methods for two-component PIV. *Measurement Science and Technology*, 27(9), 2016. ISSN 13616501. doi: 10.1088/0957-0233/27/9/094006.

J. van den Bosch. Tests with two planing boats in waves. Technical report, Ship Hydromechanics Laboratory Delft University of Technology, 1970.

S. Brizzolara. Hydrodynamic Analysis of Interceptors With Cfd Methods. *The 7th International Conference on Fast Sea Transportation*, (October 2003):49–56, 2003.

B. Choi. *Influence of Bow-Wave Breaking on the Added Resistance of Fast Ships*. PhD thesis, Delft University of Technology, 2018.

E. Clement and D. Blount. Resistance tests of a systematic series of planing hull forms. *SNAME Transactions*, 71:491–579, 1963. doi: 10.1109/ICWL.2008.12.

J. Dautel, D. Martigny, P. Corrignan, and J. Tukker. Development and application of a new three components PIV system (3C-PIV) designed for towing tank applications. In *10th days of hydrodynamics*, 2005.

R. R. Dong, J. Katz, and T. T. Huang. On the structure of bow waves on a ship model. *Journal of Fluid Mechanics*, 1997.

C. W. H. van Doorne, J. Westerweel, and F. T. M. Nieuwstadt. Measurement Uncertainty of Stereoscopic-PIV for Flow with Large Out-of-plane Motion. *Particle Image Velocimetry: Recent Improvements*, (1999):213–227, 2004. doi: 10.1007/978-3-642-18795-7_15.

R. O. Duda and P. E. Hart. Use of the Hough transformation to detect lines and curves in pictures. Technical report, Sri International Menlo Park Ca Artificial Intelligence Center, 1971.

D. Dussol, P. Druault, B. Mallat, S. Delacroix, and G. Germain. Automatic dynamic mask extraction for PIV images containing an unsteady interface, bubbles, and a moving structure. *Comptes Rendus - Mecanique*, 344(7):464–478, 2016. ISSN 16310721. doi: 10.1016/j.crme.2016.03.005.

T. F. Egeberg, H. Yoon, F. Stern, and B. Pettersen. Vortex shedding from a ship hull by means of tomographic PIV. In *ASME 2014 33rd International Conference on Ocean, Offshore and Arctic Engineering*. American Society of Mechanical Engineers, 2014.

G. E. Elsinga, F. Scarano, B. Wieneke, and B. W. van Oudheusden. Tomographic particle image velocimetry. *Experiments in Fluids*, 41(6):933–947, 2006. ISSN 07234864. doi: 10.1007/s00348-006-0212-z.

M. Falchi, M. Felli, S. Grizzi, G. Aloisio, R. Broglia, and F. Stern. SPIV measurements around the DELFT 372 catamaran in steady drift. *Experiments in Fluids*, 55(11):1844, nov 2014. ISSN 0723-4864. doi: 10.1007/s00348-014-1844-z.

O. M. Faltinsen. *Hydrodynamics of high-speed marine vehicles*. Cambridge University Press, 2005.

G. Fridsma. A systematic study of the rough water performance of planing boats. Technical report, Stevens Institute of Technology, 1969.

G. Fridsma. A systematic study of the rough water performance of planing boats - Part 2 irregular waves. Technical report, Stevens Institute of Technology, 1971.

S. Grizzi, F. Pereira, and F. Di Felice. A simplified, flow-based calibration method for stereoscopic PIV. *Experiments in Fluids*, 48(3):473–486, 2010. ISSN 07234864. doi: 10.1007/s00348-009-0750-2.

L. Gui, J. Longo, and F. Stern. Towing tank PIV measurement system, data and uncertainty assessment for DTMB Model 5512. *Experiments in Fluids*, 31(3):336–346, sep 2001. ISSN 0723-4864. doi: 10.1007/s003480100293.

M. Haase, F. Iliopulos, G. Davidson, S. Friezer, G. Thomas, J. Binns, N. Bose, J. Lavroff, and M. Davis. Application of RANSE-based Simulations for Resistance Prediction of Medium-Speed Catamarans at Different Scales. *18th Australasian Fluid Mechanics Conference*, (December), 2012.

R. Hallmann, J. Tukker, and M. Verhulst. Challenges for Piv in Towing Facilities. In *International Conference on Advanced Model Measurement Technology for The Maritime Industry*, number September, pages 10–22, Nantes, 2009.

R. Huijsmans, M. Graham, and T. Kendon. The Flow Around FPSO's in Steep Regular Beam Waves: Results of PIV Experiments and RANS Computations. In *24th International Conference on Offshore Mechanics and Arctic Engineering*, pages 965–972. American Society of Mechanical Engineers, 2005.

ISO. ISO/IEC Guide 98-3: 2008 (E) Uncertainty of measurement-Part 3: Guide to the expression of uncertainty in measurement (GUM: 1995). Technical report, 2008.

ISO. ISO/IEC Guide 98-3/SI/AC1:2009(E) Uncertainty of Measurement - Part 3: Guide to the Expression of Uncertainty in Measurement (GUM:1995), Supplement 1: Propagation of Distributions Using a Monte Carlo Method, Technical Corrigendum 1. Technical report, 2009.

ITTC. Practical Guidelines for Ship CFD Applications. 2011.

G. Jacobi, C. Thill, and R. Huismans. The Application of Particle Image Velocimetry for the Analysis of High-Speed Craft Hydrodynamics. In *International Conference on Hydrodynamics*, number September, 2016.

G. Jacobi, C. Thill, and R. Huismans. Pressure reconstruction from velocity field measurements, obtained with particle image velocimetry, in the bow region of a fast ship. In *Int. Conference on Advanced Measurement Technology for the Maritime Industry*, 2019a.

G. Jacobi, C. H. Thill, R. van't Veer, and R. H. Huijsmans. Analysis of the influence of an interceptor on the transom flow of a fast ship by pressure reconstruction from stereoscopic scanning PIV. *Ocean Engineering*, 181(February):281–292, 2019b. ISSN 00298018. doi: 10.1016/j.oceaneng.2019.02.062.

M. L. Jakobsen, T. P. Dewhirst, and C. A. Greated. Particle image velocimetry for predictions of acceleration fields and force within fluid flows. *Measurement Science and Technology*, 8(12):1502–1516, 1997. ISSN 09570233. doi: 10.1088/0957-0233/8/12/013.

P. de Jong. *Seakeeping Behaviour of High Speed Ships: An Experimental and Numerical Study*. PhD thesis, Delft University of Technology, 2011.

P. de Jong and J. A. Keuning. 6-DOF forced oscillation tests for the evaluation of nonlinearities in the superposition of ship motions. *International Shipbuilding Progress*, 53: 123–143, 2006. ISSN 0020868X.

P. de Jong, F. van Walree, J. Keuning, and R. Huijsmans. Evaluation of the free surface elevation in a timedomain panel method for the seakeeping of high speed ships. In *Proceedings of the 17th International Offshore and Polar Engineering Conference*, pages 2134–2141, Lisboa, 2007.

A. Jurgens, R. Hallmann, and J. Tukker. Experimental investigation into the flow around a manoeuvring LNG carrier on shallow water. In *International Conference on Ship and Shipping Research*, 2006.

J. Keuning and J. Pinkster. Optimisation of the seakeeping behaviour of a fast monohull. In *Proceeding of the 3th International Conference on Fast Sea Transportation*, 1995.

J. Keuning and F. van Walree. The comparison of the hydrodynamic behaviour of three fast patrol boats with special hull geometries. In *Proceedings of the 5th International Conference on High-Performance Marine Vehicles*, 2006.

J. Keuning, S. Toxopeus, and J. Pinkster. The effect of bow shape on the seakeeping performance of a fast monohull. *FAST Conference Proceedings ...*, 2001.

J. A. Keuning. *Nonlinear Behaviour of Fast Monohulls in Head Waves*. PhD thesis, Delft University of Technology, 1994.

J. A. Keuning. Grinding the bow. *International Shipbuilding Progress*, 53:281–310, 2006.

J. A. Keuning and J. Gerritsma. Resistance tests of a series of planing hull forms with 25 degrees deadrise angle. *International Shipbuilding Progress*, 29:222–249, 1982.

J. A. Keuning and J. Pinkster. The Axebow, a futher improvement on the seakeeping performance of a fast monohull. *Schip en Werf en de Zee*, 12(1):31–36, 2002.

L. Larsson, F. Stern, and M. Visonneau. *Numerical ship hydrodynamics: an assessment of the Gothenburg 2010 workshop*. Springer Science & Business Media, 2013.

LaVision. Underwater 3D Flow Field Measurement - Lagrangian Particle Tracking with MiniShaker Underwater. Technical report, 2019.

N. J. Lawson and J. Wu. Three-dimensional particle image velocimetry: Experimental error analysis of a digital angular stereoscopic system. *Measurement Science and Technology*, 8(12):1455–1464, 1997. ISSN 09570233. doi: 10.1088/0957-0233/8/12/009.

J. Longo, J. Shao, M. Irvine, L. Gui, and F. Stern. Unsteady PIV for regular head waves. *lcgui.net*, 5512, 2001.

J. Longo, J. Shao, M. Irvine, and F. Stern. Phase-Averaged PIV for the Nominal Wake of a Surface Ship in Regular Head Waves. *Journal of Fluids Engineering*, 129(5):524, 2007. ISSN 00982202. doi: 10.1115/1.2717618.

M. Mansoori and A. C. Fernandes. Hydrodynamics of the interceptor on a 2-D flat plate by CFD and experiments. *Journal of Hydrodynamics*, 27(6):919–933, 2015. ISSN 10016058. doi: 10.1016/S1001-6058(15)60555-8.

M. Mansoori and A. C. Fernandes. Hydrodynamics of the Interceptor Analysis Via Both Ultrareduced Model Test and Dynamic Computational Fluid Dynamics Simulation. *Journal of Offshore Mechanics and Arctic Engineering*, 139(2):021101, 2016. ISSN 0892-7219. doi: 10.1115/1.4034615.

B. G. McLachlan and J. H. Bell. Pressure-sensitive paint in aerodynamic testing. *Experimental Thermal and Fluid Science*, 10(4):470–485, 1995. ISSN 08941777. doi: 10.1016/0894-1777(94)00123-P.

A. Molini and S. Brizzolara. Hydrodynamics of interceptors: A fundamental study. In *International Conference on Marine Research and Transportation*, Naples, 2005.

A. Nila, S. Vanlanduit, S. Vepa, and W. van Paepegem. A PIV-based method for estimating slamming loads during water entry of rigid bodies. *Measurement Science and Technology*, 24(4), 2013. ISSN 13616501. doi: 10.1088/0957-0233/24/4/045303.

M. Novara, R. Geisler, and A. Schroeder. Multi-stereo PIV measurement of propeller wake flow in industrial facility. Number June, pages 1–13, 2015. doi: 10.2514/6.2015-2867.

N. Otsu. A threshold selection method from gray-level histograms. *IEEE transactions on systems, man, and cybernetics*, 1:62–66, 1979.

B. W. van Oudheusden. PIV-based pressure measurement. *Measurement Science and Technology*, 24(3), 2013. ISSN 13616501. doi: 10.1088/0957-0233/24/3/032001.

B. Pearce and P. Brandner. Inviscid cavity flow over a wall-mounted fence. *Ocean Engineering*, 80:13–24, 2014. ISSN 00298018. doi: 10.1016/j.oceaneng.2014.02.003.

F. Pereira, T. Costa, M. Felli, G. Calcagno, and F. Di Felice. "A Versatile Fully Submersible Stereo-PIV Probe for Tow Tank Applications. In *Proceedings of the ASME/JSME 2003 4th Joint Fluids Summer Engineering Conference*, 2003.

A. K. Prasad. Particle image velocimetry. *Current Science*, 79(1):51–60, 2000. ISSN 00113891.

M. Raffel, C. E. Willert, F. Scarano, C. J. Kähler, and J. Wereley, S. T. Kompenhans. *Particle image velocimetry: a practical guide*. Springer, 2018.

D. Ragni. *PIV-based load determination in aircraft propellers Daniele Ragni*. PhD thesis, Delft University of Technology, 2012.

D. Ragni, B. W. van Oudheusden, and F. Scarano. 3D pressure imaging of an aircraft propeller blade-tip flow by phase-locked stereoscopic PIV. *Experiments in Fluids*, 52 (2):463–477, 2012. ISSN 07234864. doi: 10.1007/s00348-011-1236-6.

A. A. K. Rijkens, H. M. A. Cleijsen, and J. A. Keuning. On the hydrodynamic performance of an improved motion control device for fast ships. In *The 12th International Conference on Fast Sea Transportation*, 2013.

P. J. Roache. Verification of codes and calculations. *AIAA Journal*, 36(5):696–702, 1998. ISSN 00011452. doi: 10.2514/2.457.

H. Sakaue, T. Ozaki, and H. Ishikawa. Global oxygen detection in water using luminescent probe on anodized aluminum. *Sensors*, 9(6):4151–4163, 2009. ISSN 14248220. doi: 10.3390/s90604151.

D. Savitsky. On the seakeeping of planing hulls. *Marine Technology*, 5(2):164–174, 1968.

A. Savitzky and M. J. Golay. Smoothing and differentiation of data by simplified least squares procedures. *Analytical chemistry*, 36(8):1627–1639, 1964.

S. Scharnowski, K. Grayson, C. M. de Silva, N. Hutchins, I. Marusic, and C. J. Kähler. Generalization of the PIV loss-of-correlation formula introduced by Keane and Adrian. *Experiments in Fluids*, 58(10):1–12, 2017. ISSN 07234864. doi: 10.1007/s00348-017-2431-x.

A. Sciacchitano and B. Wieneke. PIV uncertainty propagation. *Measurement Science and Technology*, 27(8), 2016. ISSN 13616501. doi: 10.1088/0957-0233/27/8/084006.

A. Sciacchitano, D. R. Neal, B. L. Smith, S. O. Warner, P. P. Vlachos, B. Wieneke, and F. Scarano. Collaborative framework for PIV uncertainty quantification: Comparative assessment of methods. *Measurement Science and Technology*, 26(7), 2015. ISSN 13616501. doi: 10.1088/0957-0233/26/7/074004.

C. M. de Silva, J. Philip, and I. Marusic. Minimization of divergence error in volumetric velocity measurements and implications for turbulence statistics. *Experiments in Fluids*, 54(7), 2013. ISSN 07234864. doi: 10.1007/s00348-013-1557-8.

J. Tukker, J. J. Blok, G. Kuiper, and R. H. M. Huijsmans. Wake Flow Measurements in Towing Tanks with PIV. *Proceedings of 9th International Symposium on Flow Visualization*, (373):1–12, 2000.

D. Villa and S. Brizzolara. A Systematic CFD Analysis of Flaps/Interceptors Hydrodynamic Performance. *The 10th International Conference on Fast Sea Transportation*, (2):1023–1038, 2009.

F. van Walree. *Computational methods for hydrofoil craft in steady and unsteady flow*. PhD thesis, Delft University of Technology, 1999.

F. van Walree, D. Sgarioto, and T. Turner. Validation of a time domain panel code for prediction of impulsive loads on high speed ships. In *Symposium on Naval Hydrodynamics*, 2016.

J. Westerweel, D. Dabiri, and M. Gharib. The effect of a discrete window offset on the accuracy of cross-correlation analysis of digital PIV recordings. *Experiments in Fluids*, 23(1):20–28, 1997. ISSN 07234864. doi: 10.1007/s003480050082.

B. Wieneke. Stereo-PIV using self-calibration on particle images. *Experiments in Fluids*, 39(2):267–280, 2005. ISSN 07234864. doi: 10.1007/s00348-005-0962-z.

B. Wieneke. PIV uncertainty quantification from correlation statistics. *Measurement Science and Technology*, 26(7), 2015. ISSN 13616501. doi: 10.1088/0957-0233/26/7/074002.

B. Wieneke. *PIV Unvertainty Quantification and Beyond.* PhD thesis, Delft University of Technology, 2017.

J. J. D. Wilde, R. H. M. Huijsmans, and J. Tukker. Experimental Investigation into the Vortex Formation in the Wake of an Oscillating Cylinder Using Particle Image Velocimetry. In *Proceedings of the Sixteenth (2006) International Offshore and Polar Engineering Conference*, volume 4, pages 798–805, San Francisco, 2006. ISBN 1880653664.

C. Willert. Stereoscopic digital particle image velocimetry for application in wind tunnel flows. *Measurement Science and Technology*, 8(12):1465–1479, 1997. ISSN 09570233. doi: 10.1088/0957-0233/8/12/010.

H. Yoon, J. Longo, Y. Toda, and F. Stern. Benchmark CFD validation data for surface combatant 5415 in PMM maneuvers - Part II: Phase-averaged stereoscopic PIV flow field measurements. *Ocean Engineering*, 109:735–750, 2015. ISSN 00298018. doi: 10.1016/j.oceaneng.2015.09.046.

E. Zarnick. A nonlinear mathematical model of motions of planing boats in regular head waves. Technical report, DTNSRDC, 1978.

ACKNOWLEDGEMENTS

The presented research has been conducted within the Fast FEM project under the guidance of the Dutch organization for scientific research NWO. The project has been made possible with contributions from DAMEN Shipyards, Maritime Research Institute Netherlands, the Royal Netherlands Navy, Bureau Veritas, Lloyds Register, the Royal Netherlands Rescue Organization KNRM and the University of Twente.

The successful completion of this work has, by far, not been the achievement of an individual person. It is the result of collaboration and exchange of knowledge with other people and especially emotional support and motivation.

I first want to express my gratitude to my promotor Prof. Rene Huijsmans for giving me the opportunity to conduct research on the herein presented subject and the support throughout the last years. Furthermore, I want to thank my current co-promotor, Dr. Ido Akkerman, for his thorough review and critical comments and discussions concerning the mathematical and numerical parts of the conducted research. In the same way, I want to thank Dr. Conel Thill for his supervision within the first years and the fruitful discussions during the planning of the experimental campaigns. I am also grateful to the independent committee members for their time and effort to read the dissertation and for providing me with further valuable feedback.

The PIV measurements conducted within this work would have been less successful without the extensive support of Radomir Beslac and Alex Nila from LaVision. The continuous exchange of knowledge resulted in a fruitful collaboration and further improvement of the underwater PIV system. In this context, I also want to thank Rink Hallman and Jan Tukker from MARIN for their advice on performing PIV measurements in towing tanks and the discussions about measurement uncertainty.

During my experimental campaigns, I experienced lots of help from the personnel of the Delft Ship Hydromechanics Laboratory: Peter Poot, Jasper den Ouden, Frits Sterk, Hans van der Hek, Wick Hillege, Jennifer Rodriquez Monteiro and Pascal Chabot. Thank you for realizing my sometimes inconvenient ideas and supporting me on the towing tank carriage with setting up and running my experiments.

Not only for their expert advice and fruitful discussions but also for their distraction, I want to thank my other colleagues and fellow Ph.D. students: Sebastian, Peter, Nico, Giovanni, Swaraj, BongJun. Especially, I want to thank my former office mates: Albert, who supported me during the initial phase of my Ph.D. and Matteo, with whom I shared all the ups and downs of being a Ph.D. student in the last years.

Probably more important than any expert advice was the emotional support and motivation I experienced from my friends and family within the last years. Therefore, I would particularly like to thank my parents and my sister, who also helped me to design the cover of this book.

The two persons who are probably more happy over the end of this work than I am, are my partner Skadi and my son Jona. Finishing this work has asked lots of dedication and extra working hours, at the cost of many other activities, potentially much more pleasant. Skadi, thank you for taking the decision to move with me to the Netherlands and for your love and support during the last years, which substantially contributed to the successful completion of this work.

CURRICULUM VITÆ

Gunnar JACOBI

Gunnar Jacobi was born on 18 Mai 1987 in Göttingen, Germany. In 2006, he commenced his studies in mechanical engineering at Clausthal University of Technology. After finishing his undergraduate studies in 2008, he continued his studies at the University of Rostock, specializing in naval architecture and maritime engineering. During his graduate studies, he worked amongst others as an intern at Voith Turbo Advanced Propeller Technologies and BaltiCo, supporting the design of composite propellers with numerical methods. In 2010 he was granted a scholarship from the Veith-Berghoff Foundation for an academic visit at the Australian Maritime College to investigate the motion response and slamming behavior of high-speed catamarans. He completed his graduate studies in 2012 with honors. Within his thesis, he worked on the development of a hybrid CFD method for concentrated vortex structures and its numerical implementation. In 2013 he continued his work on the coupling of finite-volume and vortex methods for increased accuracy in propeller wake modeling as a research assistant for numerical methods and ship hydrodynamics at the Chair of Modelling and Simulation at the Faculty of Mechanical Engineering and Marine Technology of the University of Rostock.

In 2014 he commenced his Ph.D. research on the application of particle image velocimetry for the analysis of high-speed craft hydrodynamics at the Ship Hydromechanics and Structures Section of the Delft University of Technology. The results of this work are presented in this dissertation. Parts of the research will be continued during a subsequent Post-Doc employment at the same institution.

LIST OF PUBLICATIONS

Publications, related to this thesis:

3. G. Jacobi, C. H. Thill, and R.H.M. Huijsmans. Pressure reconstruction from velocity field measurements, obtained with particle image velocimetry, in the bow region of a fast ship. *Int. Conference on Advanced Model Measurement Technology for The Maritime Industry*, 2019

2. G. Jacobi, C. H. Thill, R. van't Veer and R.H.M. Huijsmans. Analysis of the influence of an interceptor on the transom flow of a fast ship by pressure reconstruction from stereoscopic scanning PIV. *Ocean Engineering*, (181):281-292, 2019.

1. G. Jacobi, C. H. Thill, and R.H.M. Huijsmans. The application of particle image velocimetry for the analysis of high-speed craft hydrodynamics. *Int. Conference on Hydrodynamics*, 2016.

Further publications:

4. G.Jacobi, G. Thomas, M.R. Davis, G. Davidson. An insight into the slamming behaviour of large high-speed catamarans through full-scale measurements *Journal of Marine Science and Technology*, 19(1),15-32, 2014

3. N. Kornev, G. Jacobi. Development of a hybrid approach using coupled grid-based and grid-free methods. *Computational Methods in Marine Engineering V - Proceedings of the 5th International Conference on Computational Methods in Marine Engineering*, 2013

2. N. Kornev, V. Zhdanov, G. Jacobi, I. Cherunova. Development of a hybrid grid-and particle-based numerical method for resolution of fine vortex structures in fluid mechanics. *International Conference on Particle-based Methods, Fundamentals and Applications*, 2013

1. G. Jacobi, G. Thomas, M.R. Davis, D.S. Holloway, G. Davidson, T. Roberts. Full-scale motions of a large high-speed catamaran: The influence of wave environment, speed and ride control system. *Transactions of the Royal Institution of Naval Architects Part A: International Journal of Maritime Engineering*, 154(A3),143-155, 2012